



Analysis of the process $e^+e^- \rightarrow \mu^+\mu^-(n\gamma)$
at centre-of-mass energies from 60 to 140 GeV
with the ALEPH detector at LEP. ¹

Frederic Teubert
Universitat Autònoma de Barcelona
Institut de Física d'Altes Energies
Edifici Cn
08193 Bellaterra (Barcelona)

December 1996

¹Ph. D. Dissertation

Contents

1	Introduction	1
2	Theoretical framework	4
2.1	The Standard Model of EW interactions	4
2.1.1	Lowest order SM predictions for the process $e^+e^- \rightarrow \mu^+\mu^-$	6
2.1.2	Higher order corrections	11
2.1.3	Higher order SM predictions for the process $e^+e^- \rightarrow \mu^+\mu^-(\gamma)$	14
2.2	Model independent approaches to the process $e^+e^- \rightarrow \mu^+\mu^-$	22
2.2.1	The effective coupling language	23
2.2.2	The S-matrix language	25
2.3	Beyond the Standard Model. Z' physics	28
3	The ALEPH detector	34
3.1	The LEP collider	34
3.1.1	Determination of the beam energy	36
3.2	The ALEPH apparatus	39
3.2.1	General description	39
3.2.2	Subdetectors relevant to the analysis	46
3.3	Event reconstruction and simulation	55
3.3.1	Tracking in ALEPH	55
3.3.2	Particle identification: μ and γ	57
3.3.3	Monte Carlo simulation	59

4	Data analysis	61
4.1	Determination of the effective centre-of-mass energy	61
4.2	Event selection	66
4.3	Correction functions ($\epsilon_{F(B)}(s, x)$)	72
4.4	The loglikelihood function	75
5	Results and systematic studies	82
5.1	Extraction of the S-matrix parameters	82
5.2	Systematic studies	89
5.3	Analysis of the helicity cross sections and new scalar interactions . .	95
5.4	Limits on extra Z bosons	99
6	Summary and conclusions	102
A	Writing the helicity cross sections in the S-matrix language.	104
B	Relativistic kinematics.	107
B.1	Effective centre-of-mass energy.	107
B.2	Final State Radiation in the CM system.	108
C	Efficiencies computed from Monte Carlo simulation.	110

List of Figures

2.1	Feynman diagrams contributing at tree level to the process $e^+e^- \rightarrow \mu^+\mu^-$	7
2.2	Schematic representation of the process $e^+e^- \rightarrow \mu^+\mu^-$	8
2.3	Contributions of the individual channels	10
2.4	Weak box corrections	14
2.5	Vertex corrections	15
2.6	Vacuum polarization corrections	15
2.7	QED Initial State corrections	18
2.8	QED Initial-Final state interference corrections	19
2.9	Contribution of the I-F QED interference as a function of the cut on x_{max}	20
2.10	QED Final State corrections	22
2.11	Schematic representation of the S-matrix ansatz	25
2.12	Comparison of the S-matrix ansatz with the SM predictions	29
2.13	Deviation of $\hat{\sigma}$ and $\hat{\sigma}_{fb}$ with respect the SM predictions, for several Z' models	33
3.1	Schematic representation of the LEP ring	36
3.2	Schematic representation of the LEP injectors and accelerators	37
3.3	Change of LEP energy as a result of the tide	38
3.4	Schematic view of the ALEPH detector	40
3.5	Cut-away view of the VDET	47
3.6	The ITC drift cells	48
3.7	View of the TPC	49
3.8	View of a TPC end-plate	50
3.9	View of a TPC wire chamber	50

3.10	View of an ECAL stack layer	53
3.11	Overall view of the ECAL and HCAL calorimeters	54
3.12	Momentum resolution in the tracking system for dimuon events	56
4.1	$ \beta $ as a function of the acollinearity and $\cos \theta_1$	63
4.2	Definition of the angles used to compute β	64
4.3	MonteCarlo study of the performance of the s' reconstruction	65
4.4	Momentum of the most energetic track normalized	69
4.5	Comparison of the Photon reconstruction performance between data and MC	70
4.6	$\epsilon_{F,B}(x)$ at different nominal centre-of-mass energies	74
5.1	Measured cross sections as a function of the effective centre-of-mass	87
5.2	Measured forward-backward asymmetries as a function of the effective centre-of-mass	88
5.3	Relative change in the asymmetry as a function of x_{max}	90
5.4	Comparison of efficiencies when FSR is exponentiated or not	92
5.5	Angular distribution of the detected photon from Data and MC	93
5.6	Energy deposited in ECAL by the two muon candidates.	94
5.7	Helicity cross sections as a function of the effective centre-of-mass energy	97
5.8	Contours of equal probability in the plane R_{SCAL} vs M_{SCAL}	98
5.9	Curves corresponding to 95% confidence level exclusion limits on new gauge bosons	101

List of Tables

2.1	SM predictions for the S-matrix parameters	28
3.1	Momentum resolution of the tracking system	56
4.1	MonteCarlo statistics used	67
4.2	Breakdown of the effect of the selection cuts	71
4.3	Computed efficiency at the different LEP nominal energies.	72
4.4	I-F QED interference corrections	78
4.5	Luminosity correlation matrix	79
4.6	Inclusive cross-section and luminosities	81
5.1	Results obtained for the electroweak parameters	83
5.2	Results obtained for the electroweak parameters as a function of the running period	84
5.3	Number of observed events in the different intervals of energy	84
5.4	Measured cross sections and asymmetries	86
5.5	Breakdown of systematic errors	94
5.6	95% confidence level limits on the mass and mixing angle of a new gauge boson	100
C.1	Computed $\epsilon_{F(B)}(s, x)$ at the different LEP nominal energies	111

Chapter 1

Introduction

Since its formulation in the 60s, the Standard Model [1] (SM) of electroweak interactions has been extensively tested with great success. In particular, the high statistics accumulated by the LEP experiments from 1989 to 1995 (when the first phase of LEP at centre-of-mass energies close to 91 GeV ended) and the small experimental systematic uncertainties, have allowed to test the SM predictions at the quantum level.

In fact, the cross section of the process $e^+e^- \rightarrow \mu^+\mu^-$ and its angular distribution have been accurately measured at different energy points around the Z mass [2]. These measurements have allowed a precise determination of the effective couplings of the Z to the muons. Within the effective coupling language, the “on peak” measurements σ^0 and A_{FB}^0 determine completely the vector and axial coupling of the Z to the muons and hence, together with the known photon couplings, they determine the complete behaviour of the cross section and forward-backward asymmetry at any energy, in the absence of new physics beyond the Standard Model.

In a more general framework, the actual description of the energy dependence of these quantities requires the introduction of additional parameters which can be determined at LEP with just limited accuracy given the present measurements. The main reason is the limited excursion in energy during the LEP energy scans, which gives a rather small lever arm to measure the energy dependence.

In practice, by using a structure function picture of the beams, we know that the actual direct measurements are a centre-of-mass average of the “hard scattering” cross section: the “inclusive” cross sections that we have measured come from

averaging the “hard scattering” cross sections in a wide range of energies with a weight given by the initial state radiation (ISR) probability function. Conceptually, the ISR energy losses are effectively “scanning” (although in a very non-uniform way) the “hard scattering” process in a range of energy which is much broader than the nominal one of LEP.

If we consider that QED is a well established theory which, in fact, allows very accurate calculations of the ISR radiation probability, then we do know how this “ISR scan” is performed, that is, which is the actual probability of the “naked beams” colliding at a certain energy. The idea, then, is to try to be more “exclusive” in the measurements, by extracting from the event characteristics the centre-of-mass energy of the “hard scattering” process. Although this is not a rigorous procedure in quantum mechanics, we shall see that theoretically one can justify and show its validity in a very good approximation.

The reconstruction of the effective centre-of-mass energy is possible in the case of muon pair production process, because of the absence of neutrinos (in contrast to the case of tau production), and because they are produced via s-channel annihilation.

So far, the analysis of radiative muon events carried out by other LEP experiments [3] was based on the specific selection of events with strong initial state radiation. This requirement results in a very small sample of events, and only the global agreement with the SM expectations could be checked.

In this thesis we introduce a new method to determine, on an event-by-event basis, the actual centre-of-mass energy of the “hard scattering” process. This will allow us to use all the muon events and hence, all the statistical power of the data, giving us maximal sensitivity to the electroweak parameters. We will show that, by setting up a suitable fitting procedure allowing us to use that information, we can obtain precise determinations of the cross section and the forward-backward asymmetry in a wide range of energies, spanning without gaps from 60 to 140 GeV (the region not covered by past accelerators). These measurements enable us to make accurate determinations of the energy dependence of the cross section and the forward-backward asymmetry as well as to place constraints on the existence of new Z bosons that could change this dependence. Moreover, we can explore for the first time the centre-of-mass energy region around 80 GeV and 113 GeV, where the violation of parity symmetry is maximal, and therefore the sensitivity to the

presence of new scalar interactions that could couple to the initial electrons or final muons is maximized.

In addition, by deconvolving the measurements taken at the Z resonance from the ones taken at different effective energies, we optimize the extraction of the electroweak parameters, giving the correct statistical weight to each event.

The outline of this thesis is as follows: in chapter two we analyze the theoretical framework of our approach. We start with a description of the SM predictions for the process of interest here, and then we develop the “model independent” formalism and we study the precision achieved in the relevant interval of energies. A brief description of possible extensions of the SM that would introduce new gauge bosons is introduced at the end of chapter two.

Chapter three is devoted to the description of the experimental apparatus, the LEP collider and the ALEPH detector, together with a description of the algorithms used in the analysis to identify muon candidates and photons in ALEPH, and to reconstruct the particle direction.

Chapter four is devoted to explain the specific selection procedure, and to build the likelihood function to be maximized. In chapter five we show the results obtained for the electroweak parameters, and their systematic uncertainties. From these results, we study possible extensions of the SM, (new scalar interactions and new gauge bosons). The final summary and conclusions are given in chapter six.

Chapter 2

Theoretical framework

This chapter describes the theoretical framework necessary to interpret the results of this analysis. In section 2.1 the Standard Model predictions for the process $e^+e^- \rightarrow \mu^+\mu^-$ are given and it is shown how the inclusion of higher order corrections are absolutely necessary to cope with the experimental accuracy. In section 2.2 we present the necessary language to describe this process in an almost model independent way, and it is compared with the actual Standard Model predictions. The last section 2.3 is devoted to possible extensions of the Standard Model that include new gauge bosons, because these are the most obvious candidates to modify the predicted energy dependence of the observables in the energy range from 60 GeV to 140 GeV.

2.1 The Standard Model of EW interactions

The Standard Model [1] (SM) is a gauge theory, based on the group $SU(3)_C \otimes SU(2)_L \otimes U(1)_Y$, which describes strong, weak and electromagnetic interactions, via the exchange of the corresponding spin-1 gauge fields: 8 massless gluons and 1 massless photon for the strong and electromagnetic interactions respectively, and 3 massive bosons, W^\pm and Z^0 , for the weak interaction. The fermionic-matter content is given by the known leptons and quarks, which are organized in a 3-fold family structure:

leptons

$$\begin{pmatrix} \nu_e \\ e_L^- \end{pmatrix}_{Y=\frac{-1}{2}} \quad \begin{pmatrix} \nu_\mu \\ \mu_L^- \end{pmatrix}_{Y=\frac{-1}{2}} \quad \begin{pmatrix} \nu_\tau \\ \tau_L^- \end{pmatrix}_{Y=\frac{-1}{2}}$$

$$(e_R^-)_{Y=-1} \quad (\mu_R^-)_{Y=-1} \quad (\tau_R^-)_{Y=-1}$$

quarks

$$\begin{pmatrix} u_L \\ d_L' \end{pmatrix}_{Y=\frac{1}{6}} \quad \begin{pmatrix} c_L \\ s_L' \end{pmatrix}_{Y=\frac{1}{6}} \quad \begin{pmatrix} t_L \\ b_L' \end{pmatrix}_{Y=\frac{1}{6}}$$

$$(u_R)_{Y=\frac{2}{3}} \quad (c_R)_{Y=\frac{2}{3}} \quad (t_R)_{Y=\frac{2}{3}}$$

$$(d_R')_{Y=\frac{-1}{3}} \quad (s_R')_{Y=\frac{-1}{3}} \quad (b_R')_{Y=\frac{-1}{3}}$$

where each quark appears in 3 different “colours”, and to each particle corresponds an antiparticle with the same mass but with opposite quantum numbers. Thus, the left-handed fields are $SU(2)_L$ doublets, while their right-handed partners transform as $SU(2)_L$ singlets. The $\{d', s', b'\}$ states are three lineal combinations of the $\{d, s, b\}$ mass eigenstates. The unitarity matrix which relates both is the Cabibbo-Kobayashi-Maskawa matrix which depends on three angles and a phase which have to be determined experimentally. This phase is the responsible of the **CP** symmetry breaking in the SM and it is widely believed that **CP** nonconservation in the early universe is the source of the apparent imbalance between matter and antimatter. There's no equivalent mixing matrix in the leptonic sector, although recent experimental results [4] seem to indicate the existence of $\nu_e - \nu_\mu$ mixing, and therefore to invalidate the hypothesis of massless neutrinos.

The gauge symmetry is broken by the vacuum, which triggers the Spontaneous Symmetry Breaking (SSB) of the electroweak group to the electromagnetic subgroup:

$$SU(3)_C \otimes SU(2)_L \otimes U(1)_Y \xrightarrow{SSB} SU(3)_C \otimes U(1)_{\text{QED}}$$

The SSB is an “intriguing” way of generating the weak gauge bosons and fermion masses while is preserving the gauge symmetry of the Lagrangian. This symmetry is essential in order to make the theory renormalizable, in other words to keep the number of “infinities” that appear in the theory finite, and therefore be absorbed in

the redefinition of a finite number of “bare” parameters. In fact, ’t Hooft demonstrated in 1971 [5] that for a theory to be renormalizable, it must be a Yang-Mills theory, that is, a theory with a local gauge invariance. Only if we have such a high degree of symmetry can we obtain the systematic cancellations of divergences order by order.

This mechanism has as a consequence the appearance of a physical scalar particle in the model, the so-called “Higgs” boson, that has not been observed experimentally. Its mass range is constrained to be $M_H > 66$ GeV [6] at 95% confidence level. The precise electroweak measurements at LEP have some sensitivity to the $\log(M_H)$ through loop corrections, and allow to constraint M_H to be below 550 GeV at 95% confidence level [7]. The next generation of machines (LEP II, LHC) should be able to decide whether the simplest Higgs model is correct.

2.1.1 Lowest order SM predictions for the process $e^+e^- \rightarrow \mu^+\mu^-$

The Feynman diagrams contributing at tree level to the process $e^+e^- \rightarrow \mu^+\mu^-$ are those shown in figure 2.1 in the massless limit where the Higgs exchange diagram is neglected. The neutral current coupling constants between the Z^0 boson and the fermions are given by,

$$v_f = \frac{I_3^f - 2Q_f \sin^2 \theta_W}{2 \sin \theta_W \cos \theta_W}, \quad a_f = \frac{I_3^f}{2 \sin \theta_W \cos \theta_W} \quad (2.1)$$

where I_3^f and Q_f denote the third isospin component and the electric charge of a given fermion specie f . θ_W is known as the weak mixing angle defined as the ratio of the weak coupling constants, (g and g'), to the gauge groups SU(2) and U(1), or equivalently,

$$\cos \theta_W = \frac{M_W}{M_Z} \quad (2.2)$$

where M_W and M_Z are the masses of the gauge fields W^\pm and Z^0 respectively.

The electromagnetic current coupling constant between the γ boson and the fermions has only a vectorial component given by the electric charge Q_f . Note that the simultaneous presence of vector and axial couplings breaks the Parity symmetry (\mathbf{P}) of the process, and as a consequence the angular distribution of the produced muon pair is not symmetric.

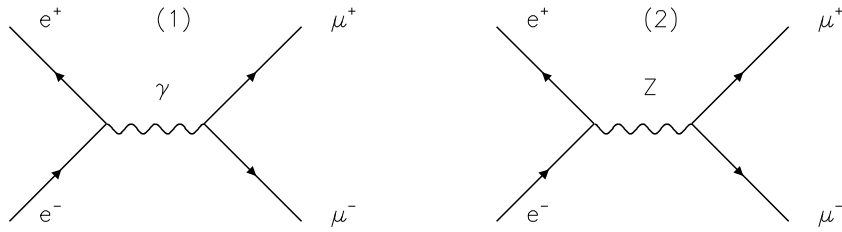


Figure 2.1: Feynman diagrams contributing at tree level to the process $e^+e^- \rightarrow \mu^+\mu^-$. The Higgs exchange diagram is neglected.

Using the Feynman rules and neglecting the fermion masses (thus neglecting the Higgs exchange diagram), the Born differential cross section for this process is obtained:

$$\begin{aligned}
 \frac{d\sigma^0(s)}{d\cos\theta} &= \frac{\pi\alpha^2}{2s} \frac{s^2}{|Z(s)|^2} \left[(1 + \cos^2\theta)(v_e^2 + a_e^2)(v_\mu^2 + a_\mu^2) + 8\cos\theta v_e v_\mu a_e a_\mu \right] \\
 &+ \frac{\pi\alpha^2}{2s} \frac{s(s - M_Z^2)}{|Z(s)|^2} \left[(1 + \cos^2\theta)2v_e v_\mu + 4\cos\theta a_e a_\mu \right] \\
 &+ \frac{\pi\alpha^2}{2s} (1 + \cos^2\theta)
 \end{aligned} \tag{2.3}$$

where the Z propagator is written in the lowest order Breit-Wigner approximation,

$$|Z(s)|^2 = (s - M_Z^2)^2 + (M_Z\Gamma_Z)^2$$

θ is the polar angle in the centre-of-mass frame between the incoming electron (e^-) and the outgoing muon (μ^-) as shown in figure 2.2, s is the centre-of-mass energy squared, M_Z is the Z^0 mass, Γ_Z is the Z^0 width and $\alpha = e^2/4\pi$ is the electromagnetic coupling constant at the Thompson limit ($\alpha(0)$).

As we have already mentioned, the SM prediction for this process is not symmetric in the space, (\mathbf{P} symmetry is not conserved), and we can define a forward-backward asymmetry as:

$$A_{fb}^0 = \frac{\sigma_f^0 - \sigma_b^0}{\sigma_f^0 + \sigma_b^0} \equiv \frac{\sigma_{fb}^0}{\sigma^0}$$

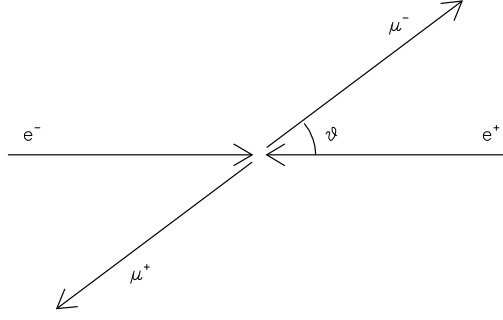


Figure 2.2: Schematic representation of the process $e^+e^- \rightarrow \mu^+\mu^-$

and

$$\begin{aligned}\sigma_f^0 &= \int_0^1 d \cos \theta \frac{d\sigma^0(s)}{d \cos \theta} \\ \sigma_b^0 &= \int_{-1}^0 d \cos \theta \frac{d\sigma^0(s)}{d \cos \theta}\end{aligned}$$

so that,

$$\sigma^0(s) = \frac{4\pi\alpha^2}{3s} \left[\frac{s^2}{|Z(s)|^2} (v_e^2 + a_e^2)(v_\mu^2 + a_\mu^2) + \frac{s(s - M_Z^2)}{|Z(s)|^2} 2v_e v_\mu + 1 \right] \quad (2.4)$$

$$\sigma_{fb}^0(s) = \frac{\pi\alpha^2}{2s} \left[\frac{s^2}{|Z(s)|^2} 8v_e v_\mu a_e a_\mu + \frac{s(s - M_Z^2)}{|Z(s)|^2} 4a_e a_\mu \right] \quad (2.5)$$

and with this definition the angular distribution at tree level can be written as:

$$\frac{d\sigma^0(s)}{d \cos \theta} = \frac{3}{8} \sigma^0(s) (1 + \cos^2 \theta) + \frac{8}{3} A_{fb}^0(s) \cos \theta \quad (2.6)$$

Note that this angular distribution is independent of the specific SM prediction and is a general consequence of the helicity conservation between the initial and the final state in the massless limit, when the interaction is mediated by a spin-1 boson. This is so, because the scattering proceeds from an initial state with $J_z = \pm 1$ to a final state with $J_{z'} = \pm 1$, where the z, z' axes are along the ongoing e^- and outgoing μ^- directions, respectively. Thus, there are four helicity amplitudes proportional to the rotation matrices,

$$d_{\lambda'\lambda}^j(\theta) = \langle j\lambda' | e^{-i\theta J_y} | j\lambda \rangle$$

where y is perpendicular to the reaction plane and λ, λ' are the net helicities along the z, z' axes. The four helicity amplitudes have the same vertex factors and are thus proportional to:

$$\begin{aligned} d_{11}^1(\theta) = d_{-1-1}^1(\theta) &= \frac{1}{2}(1 + \cos \theta) \\ d_{1-1}^1(\theta) = d_{-11}^1(\theta) &= \frac{1}{2}(1 - \cos \theta) \end{aligned}$$

If we take now the spin average of these four squared amplitudes we get an angular distribution as in equation 2.6.

Now, from the measured values of M_W and M_Z we have $\sin^2 \theta_W \sim 0.22$, and therefore using equation 2.1 $\frac{v_\mu}{a_\mu} \sim 0.1$. This implies that the Z^0 boson coupling to muons is essentially axial, and as the γ boson coupling is vectorial, the interference between both contributions will generate a forward-backward asymmetry, while the individual contributions of the diagrams appearing in figure 2.1 will be essentially symmetric. This can be seen in figure 2.3, where the contribution of the Z^0 -exchange channel, γ -exchange channel and their interference is explicitly shown. In particular, one can see how the energy dependence of the forward backward asymmetry is completely generated by the interference between both channels.

In fact, it turns out that due to the interference between the Z contribution (dominated by the axial coupling), and the γ contribution (that is only vector coupling), there is a region of energies ($\sqrt{s} \sim 80$ GeV) in which parity violation is maximal and $\sigma_{LL} \sim \sigma_{RR} \sim 0$, where $i(j)$ in σ_{ij} stands for the polarization of the incoming e^- (outgoing μ^-) [8]. Similarly, there is a region around $\sqrt{s} \sim 113$ GeV where $\sigma_{LR} \sim \sigma_{RL} \sim 0$ and parity violation is maximal too. In terms of helicity cross sections, the total and antisymmetric cross sections can be written as

$$\begin{aligned} \sigma^0 &= \frac{1}{2}(\sigma_{LL} + \sigma_{RR} + \sigma_{LR} + \sigma_{RL}) \\ \sigma_{fb}^0 &= \frac{3}{8}(\sigma_{LL} + \sigma_{RR} - \sigma_{LR} - \sigma_{RL}) \end{aligned}$$

so that, at these interesting energies $\sigma_{fb}^0 = \pm \frac{3}{4}\sigma$, and corresponds to the maximum value for $|\sigma_{fb}^0|$ that the probability density of eq. 2.6 allows (for values of $|A_{fb}^0|$ larger than $3/4$ the differential cross section is not positive defined because it will imply a negative helicity cross section).

A study of the muon pair production at these energies allows to search for new physics in an environment of minimal background [8]. More specifically, a scalar

interaction that will not interfere with the Z^0 or the photon contribution, will naturally show up at these energies.

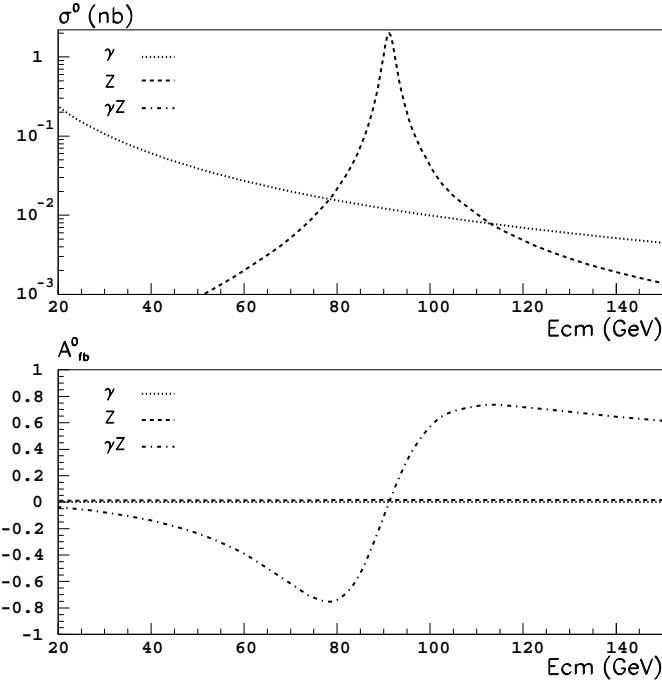


Figure 2.3: Contributions of the individual channels to the muon pair production process. The size of the interference contribution for σ^0 is below 10^{-3} nb and is not shown in the upper figure.

In principle, the SM has some free parameters that need to be fixed experimentally in order to be able to use equation 2.3. The most natural option is to take the best measured parameters as input parameters of the theory:

$$\begin{aligned}
 \alpha &= \frac{1}{137.0359895(61)} \\
 G_F &= 1.166389(22) \times 10^{-5} \text{GeV}^{-2} \\
 M_Z &= 91.18(63) \text{GeV}
 \end{aligned}
 \tag{2.7}$$

being the first one the electromagnetic coupling constant measured at very low q^2 (Thompson limit), and the second one is the Fermi coupling constant, obtained from the analysis of the muon decay using the Fermi interaction language. If instead of the Fermi language, one uses the SM language at Born level to predict the

muon lifetime measurement, then G_F is equivalent to the product of the W boson couplings times the W boson propagator at $q^2 \rightarrow 0$, namely:

$$G_F = \frac{\pi\alpha}{\sqrt{2}} \frac{1}{M_W^2 \sin^2 \theta_W} \quad (2.8)$$

so that, in practice, we can substitute M_W in equation 2.2 by G_F that is much better known. Defining

$$A_0 \equiv \frac{\pi\alpha}{\sqrt{2}G_F} = (37.2802(3)\text{GeV})^2$$

one can compute M_W , and therefore $\sin^2 \theta_W$ as

$$\begin{aligned} M_W &= \frac{M_Z}{\sqrt{2}} \left[1 + \left(1 - \frac{4A_0}{M_Z^2} \right)^{1/2} \right]^{1/2} \rightarrow 80.937\text{GeV} \\ \sin^2 \theta_W &= \frac{1}{2} \left[1 - \left(1 - \frac{4A_0}{M_Z^2} \right)^{1/2} \right] \rightarrow 0.2122 \end{aligned}$$

Nevertheless, the direct data on M_W gives $M_W = 80.356 \pm 0.125$ GeV [9], that is, about 4.6 sigma off from the above prediction. If the neutrino-nucleon data is used in addition [10], then the best experimental determination of $\sin^2 \theta_W$ is $\sin^2 \theta_W = 0.2237 \pm 0.0021$ at about 5.5 sigma from the above prediction. So, already at this stage, one can see that the Born SM language is not accurate enough to describe the data and therefore, since the SM is a renormalizable theory, we must include higher order contributions to correct the above expressions.

2.1.2 Higher order corrections

In order to take into account higher order corrections, the first step is to define the renormalization scheme, that is, to define the “bare” input parameters of the theory that need to be renormalized and the corresponding renormalization equations. The discussion that follows is based on the on-shell-mass renormalization scheme where the “bare” parameters to be renormalized are the electromagnetic coupling constant, the masses of all the particles in the theory and the Cabibbo-Kobayashi-Maskawa fermionic mixing angles.

At one loop, equation 2.8 becomes,

$$G_F = \frac{\pi\alpha}{\sqrt{2}} \frac{1}{M_W^2 \sin^2 \theta_W} (1 + \Delta r) \quad (2.9)$$

Since in the self energy corrections all kind of heavy particles may show up virtually, in practice the size of Δr depends on all the constants of the SM Lagrangian and, in particular, on the still unknown (or badly known) top mass and Higgs mass.

Δr is customarily splitted into pieces which have different conceptual origin:

$$\Delta r = \Delta\alpha - \frac{\cos^2 \theta_W}{\sin^2 \theta_W} \Delta\rho + \Delta r_{rem} \quad (2.10)$$

Let's discuss a little bit the different contributions to Δr that constitute the basic building blocks of radiative corrections.

Photon vacuum polarization: $\Delta\alpha$

$\Delta\alpha$ describes the change in the electric charge coupling from $q^2 = 0$ to the real q^2 of the interaction. Therefore at energies around the Z^0 mass,

$$\alpha(M_Z^2) = \frac{\alpha}{1 - \Delta\alpha} \quad (2.11)$$

which within the SM is

$$\Delta\alpha = \frac{\alpha}{3\pi} \sum_l Q_l^2 \left(\log \frac{M_Z^2}{m_l^2} - \frac{5}{3} \right) + \Delta\alpha_{had} + \dots$$

where the first term is the contribution for charged leptons, $\Delta\alpha_{had}$ the contribution for quarks and the dots indicate remaining (small) bosonic contributions. One can see from the above expression that $\Delta\alpha$ is dominated by the contribution of light particles and *it remains unchanged by new physics*. In the case of quarks, since the actual masses to be used in this expression are not well determined, $\Delta\alpha_{had}$ is in practice computed via dispersion relations using the experimental data on hadronic e^+e^- cross sections. Recently there has been some updates on the number obtained with this procedure [11], and we will take the standard value taken by the LEP community $\Delta\alpha_{had} = 0.0280 \pm 0.0007$ at $q^2 = M_Z^2$ corresponding to $\alpha^{-1}(M_Z^2) = 128.896 \pm 0.090$.

Quantum corrections to the ρ parameter: $\Delta\rho$

The ρ parameter is defined as the relation between the neutral and charged current strength at $q^2 = 0$. In the SM at tree level,

$$\rho_0 = \frac{M_W^2}{\cos^2 \theta_W M_Z^2} = 1$$

but after computing one loop corrections $\rho = \rho_0 + \Delta\rho$ being

$$\Delta\rho = \frac{\sqrt{2}G_F}{16\pi^2} \sum_f N_{c,f} \Delta m_f^2 + \dots$$

being f all fermion doublets, $N_{c,f}$ their possible number of colours and $\Delta m_f^2 = |m_{f1}^2 - m_{f2}^2|$ the doublet mass splitting. $\Delta\rho$ is negligible for light fermions but large for heavy fermions with a light iso-doublet partner. Therefore, the largest contribution is, by far:

$$\Delta\rho \sim \Delta\rho_{tb} = \frac{\sqrt{2}G_F}{16\pi^2} 3m_t^2 \quad (2.12)$$

which amounts to about 1% for $m_t = 175$ GeV. $\Delta\rho$ is sensitive to all kind of SU(2) multiplets which couple to gauge bosons and exhibit large mass splitting and hence, *it is very sensitive to new physics*,

Remainder corrections: Δr_{rem}

In addition to the terms included in the two previous corrections, there are other non-leading (but non negligible) contributions, that have a logarithmic dependence with the mass of the top quark. In Δr at one loop the leading Higgs contribution is logarithmic due to the accidental SU(2)_R symmetry of the Higgs sector (the so-called custodial symmetry).

Now, from the measured M_{top} by CDF and D0 collaborations [12] ($M_{top} = 175 \pm 6$ GeV), one can compute Δr at one loop to be $\Delta r = 0.040 \pm 0.002$ neglecting the Higgs contribution, and see how the measured M_W and $\sin^2 \theta_W$ compare with the SM predictions at one loop. Introducing this result in equation 2.9 we have $M_W = 80.30 \pm 0.03$ GeV and $\sin^2 \theta_W = 0.2245 \pm 0.0007$, that compares very nicely with the experimental measurements mentioned in the previous section, ($M_W = 80.356 \pm 0.125$ GeV, $\sin^2 \theta_W = 0.2237 \pm 0.0021$).

So, the message is clear... at the present level of experimental accuracy, one needs to compute the SM predictions at least to one loop. We will see in the next section, that even this is not enough for some specific kind of radiative corrections, but let's focus now on the higher order SM predictions for the relevant process in this work.

2.1.3 Higher order SM predictions for the process $e^+e^- \rightarrow \mu^+\mu^-(\gamma)$

The goal is to be able to predict the total cross-section and forward-backward asymmetry for the muon pair production process with a precision better than the permille level at the Z resonance. To do this, one needs to take into account higher order corrections not only in the definition of the input parameters (α, G_F) determined at $q^2 \rightarrow 0$, but also include the specific higher order corrections for this process.

At one loop, the radiative corrections to the process $e^+e^- \rightarrow \mu^+\mu^-$ can be classified into two groups: photonic and non-photonic corrections. The first one includes all contributions in which a photon line is added to the born diagram and the second group includes the rest. This separation is specially important for neutral current processes in which the non-photonic corrections at one-loop level separate naturally from the photonic ones forming a gauge-invariant subset.

Non-photonic corrections

These corrections do not depend on experimental cuts, (with the exception of box diagrams) and contain relevant information on the non-energetically available elements of the theory. So, they are the ones that allow the detailed test of the quantum structure of the SM and the search for new physics. At one loop, these contributions can be classified into three types, namely: box corrections (figure 2.4), vertex corrections (figure 2.5) and vacuum polarization corrections (figure 2.6), in such a way that one can just modify equation 2.6 with

$$\frac{d\hat{\sigma}(s)}{d\cos\theta} = \frac{d\sigma^0(s)}{d\cos\theta} (1 + \Delta_{box}(s, \cos\theta) + \Delta_{vertex}(s) + \Delta_{vacuum}(s)) \quad (2.13)$$

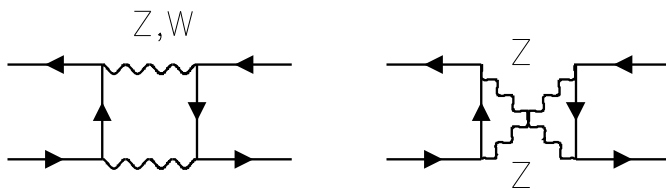


Figure 2.4: Weak box corrections.

The box corrections are very small near the Z peak due to their non-resonant structure. Their size depends on $\cos\theta$ and therefore they depend on the actual

observable studied but their typical order of magnitude is $\Delta_{box} \leq 0.02\%$. Their influence is slightly bigger at energies which are several GeV below or above M_Z , but still negligible. This allows to use the angular distribution of equation 2.6 safely (taking into account that the most precise measurements are at the Z peak).

The vertex corrections are small too, but non negligible. For all leptons their typical size is of $\Delta_{vertex} \leq 1\%$ and don't modify the $\cos \theta$ dependence. Finally, the

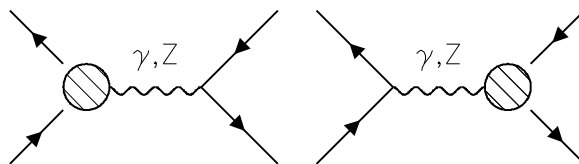


Figure 2.5: Vertex corrections.

vacuum polarization corrections (also called oblique corrections, propagator corrections and self-energies) are the largest non-photonic corrections and typically $\Delta_{vacuum} \leq 10\%$. These corrections are universal, that is independent of initial and final fermion flavour. It has been shown by several groups that in four fermion processes, the matrix element squared including non-photonic corrections can be rewritten keeping a Born-like structure by defining running effective complex parameters [13]. As we shall see in the next section, initial-final factorizable corrections such as self-energies and vertex corrections can be easily absorbed by redefining the Born couplings (Effective coupling language).

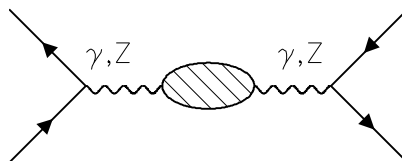


Figure 2.6: Vacuum polarization corrections.

Moreover, the effect of missing higher order corrections has been extensively studied in reference [14]. The conclusions there are that $\hat{\sigma}$ is known with a precision of about 0.05% and the forward backward asymmetry is known with a precision of about 0.04% due to the uncertainty on the hadronic contribution to $\Delta\alpha$. So that, the

precision achieved with the SM predictions at one loop copes with the experimental accuracy (say 0.2%).

Photonic corrections

The photonic corrections near the Z pole are very large for many observables. They distort noticeably the shape of their energy dependence and hence their size depends strongly on the actual energy. In addition, given the possibility to radiate real photons, they depend also strongly on the experimental cuts applied to analyze the data.

Nevertheless, the inclusion of photon lines does not add more physics than just QED and therefore, the physics interest of photonic corrections is rather limited. In general, the strategy applied to deal with these corrections consist in unfolding them as accurately as possible from the observed measurements to recover the non-photonic measurements. In this work, we will go a little bit further, and we will measure directly the non-photonic cross-section and forward backward asymmetry reconstructing the effective centre-of-mass energy of the collision.

For s-channel lineshapes, at one loop, photonic corrections can be classified into three infrared-finite gauge-invariant sets of diagrams:

- **Initial State Radiation (ISR)**. Contribution from diagrams in which a photonic line is attached to the initial state fermion (see figure 2.7). These corrections near the Z^0 pole are very large and of paramount importance. To understand why ISR corrections are so important, the physical picture of structure functions results very useful. In that picture, the colliding electrons are though as composite objects inside which, parton electrons are dressed by photons with which they share the beam's momentum. These partons collide in a "hard scattering" which is described by the amplitudes without photonic corrections. The Z^0 resonance width acts as a natural photon energy cut-off which decreases drastically the cross section. Out of all the beam's collisions, only those in which the actual parton energies is close enough to the Z^0 mass will produce a "hard scattering" event. Therefore, the Z^0 resonance acts as a monochromator of the parton energy since only those with the right energy annihilate into a Z^0 boson. Therefore, the existence of ISR decreases drastically the actual probability of Z^0 production (inclusive cross-section).

In fact, at $\mathcal{O}(\alpha)$

$$\sigma(s) = \hat{\sigma}(s)(1 + \delta_1 + \beta \ln x_0) + \int_{x_0}^1 dx \beta \left(\frac{1}{x} - 1 + \frac{x}{2} \right) \hat{\sigma}(s') \quad (2.14)$$

where the first part is the soft photon cross-section and the rest the hard one; x is the photon energy in units of the beam energy and $s' = s(1-x)$; x_0 is the soft-hard separation cut that is completely irrelevant because the final result is independent of it; δ_1 is the part of the soft radiative corrections which is independent of x_0 , its value being

$$\delta_1 = \frac{3}{4}\beta + \frac{\alpha}{\pi} \left(\frac{\pi^2}{3} - \frac{1}{2} \right) \quad (2.15)$$

β defined as

$$\beta = \frac{2\alpha}{\pi} \left(\ln \frac{s}{m_e^2} - 1 \right) \quad (2.16)$$

and it can be regarded as an effective coupling constant for bremsstrahlung. It is a factor associated to every electron bremsstrahlung vertex. At LEP energies it is large: $\beta \sim 0.11$. Now, if there's an effective energy cut-off given by the Z^0 width $x_M \sim \frac{\Gamma_Z}{M_Z}$, equation 2.14 becomes

$$\sigma(M_Z^2) \sim \hat{\sigma}(M_Z^2)(1 + \delta_1 + \beta \ln x_M)$$

and $\delta_1 \sim 0.09$ while $\beta \ln \frac{\Gamma_Z}{M_Z} \sim -0.40$, so that the infrared term dominates by far and the final total correction is of about -30% . Note that in absence of any resonance, the effective cut-off x_M disappears and we do not have any large log like the one in the previous equation in the final result. Hence the dominant correction will be then δ_1 . Given their large size, the pure one loop calculation of ISR corrections is clearly insufficient to match the experimental precision ($\sim 0.1\%$). Therefore, the calculation of the two loop terms as well as the study of the procedure to resum to all orders the infrared contributions (exponentiation) were attacked before LEP started operation. The outcome of this work was that the photonic corrections to the e^+e^- annihilation near the Z^0 pole are very accurately known [15]. Several approaches to handle higher orders, based on different physical pictures and different technical implementations (inductive exponentiation, structure functions, YFS...) have been developed and their results compare well.

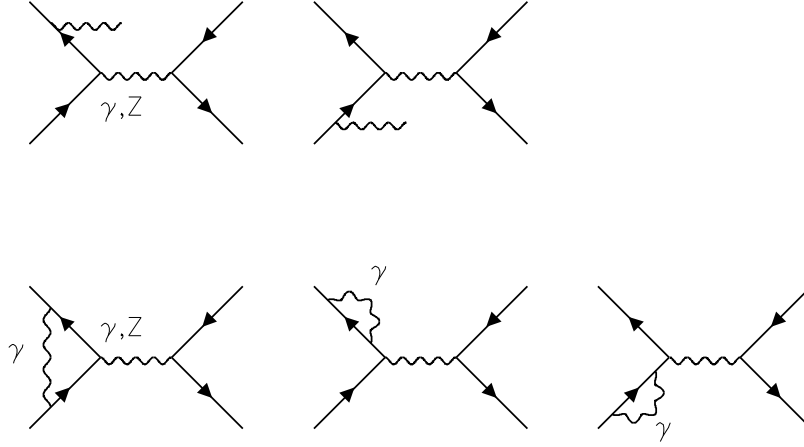


Figure 2.7: QED Initial State corrections

In practice, the probability to emit a photon that decreases the “nominal” centre-of-mass energy (\sqrt{s}) to the “effective” one ($\sqrt{s'}$) can be parameterized in a radiator function computed up to $\mathcal{O}(\alpha^2)$ and including soft photon exponentiation as:

$$H(s, x) = \beta x^{\beta-1} (1 + \delta_1 + \delta_2) - \frac{\beta}{2} (2 - x) (1 + \delta_1 + \beta \ln(x)) + \delta_2^H(x)$$

where δ_1 and δ_2 are just numerical functions independent of x , and $\delta_2^H(x)$ describes the probability of emission of hard photons up to $\mathcal{O}(\alpha^2)$. Explicit expressions for these functions can be found in [15]. One can see that when $x \rightarrow 0$, the radiator function behaves as $\beta x^{\beta-1}$, so that it is divergent in that limit, while the integrated expression goes as x^β and is finite. In this way, the differential cross section in equation 2.6 depends now on two variables ($\cos \theta$ and x) and can be written as:

$$\frac{d^2\sigma}{dx d\cos\theta}(s) = H(s, x) \left[\frac{3}{8} (1 + \cos^2\theta) \hat{\sigma}(s') + \cos\theta \hat{\sigma}_{fb}(s') \right] \quad (2.17)$$

where $\cos \theta$ is referring to the centre-of-mass reference system, and is related to the measured angles of the muon pair through:

$$\cos \theta = \frac{\sin \frac{1}{2}(\theta_{\mu^+} - \theta_{\mu^-})}{\sin \frac{1}{2}(\theta_{\mu^+} + \theta_{\mu^-})} \quad (2.18)$$

To write equation 2.17, we have made the approximation that the radiator function $H(s, x)$ is the same for the symmetric and antisymmetric cross

section. This is valid for soft photons in the collinear leading logarithmic approximation provided the scattering angle is used in the rest frame of the outgoing fermion pair.

It is not surprising that the convolution kernel for the antisymmetric part of the cross section is different from the symmetric one, since $\hat{\sigma}_{fb}$ is a less inclusive quantity than $\hat{\sigma}$ and the kinematical situation is more complicated. The radiator function $\tilde{H}(s, x)$ for the antisymmetric cross section can be related with $H(s, x)$ through [15]:

$$\tilde{H}(s, x) = H(s, x) - \theta(1 - x_0 - x) \frac{\alpha}{\pi} \frac{4x}{1-x} \log \frac{4x}{(1+x)^2} \quad (2.19)$$

where $\theta(z)$ denotes the Heaviside function.

- Initial-Final State Interference (I-F interference).** Contribution from the interference between the diagrams in which a real photonic line is attached either to the initial or the final fermionic lines (see figure 2.8). In this set of contributions, as before, the infrared divergence which shows up in the real photon emission when the photon energy vanishes, cancels the infrared divergence present in the interference between the Born amplitude and the one in which a virtual photon links the initial and the final state fermion lines (box correction). This contribution, unlike the previous one, depends on $\cos \theta$ and its analytic form is rather involved.

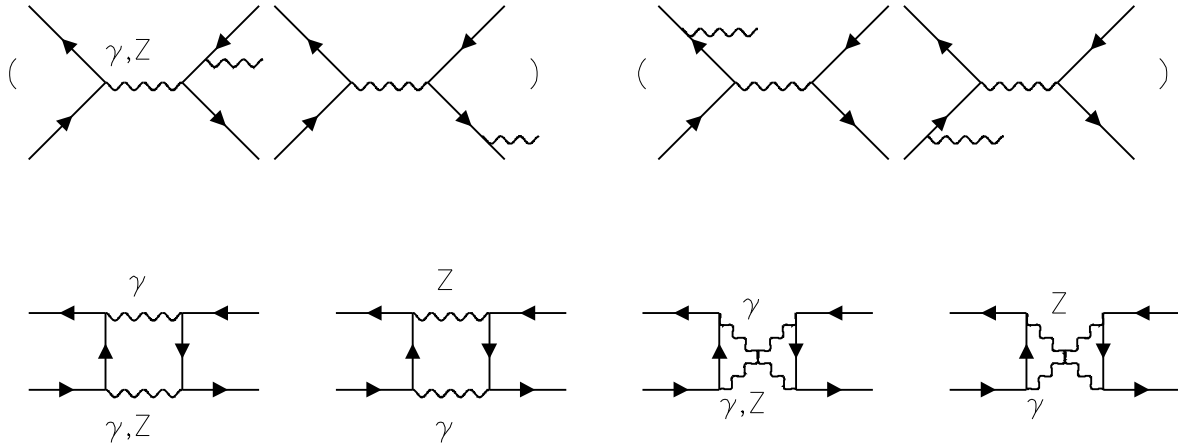


Figure 2.8: QED Initial-Final state interference corrections.

In fact, for inclusive observables, that is when there's no cut on the phase space of the Initial State photon, the contribution is very small, at the level of $\mathcal{O}(0.02\%)$ for $\hat{\sigma}$, and can be safely neglected. This is the case usually at LEP, but in our case we are interested in the differential cross-section ($\frac{d^2\sigma}{d\cos\theta dx}$) where $s' = s(1-x)$ is the square of the “effective” centre-of-mass energy that we have introduced in the discussion of the ISR corrections. In figure 2.9 one can see the contribution of the I-F QED interference for the total cross section and the forward-backward asymmetry as a function of the cut on $s'_{min} \equiv s(1-x_{max})$.

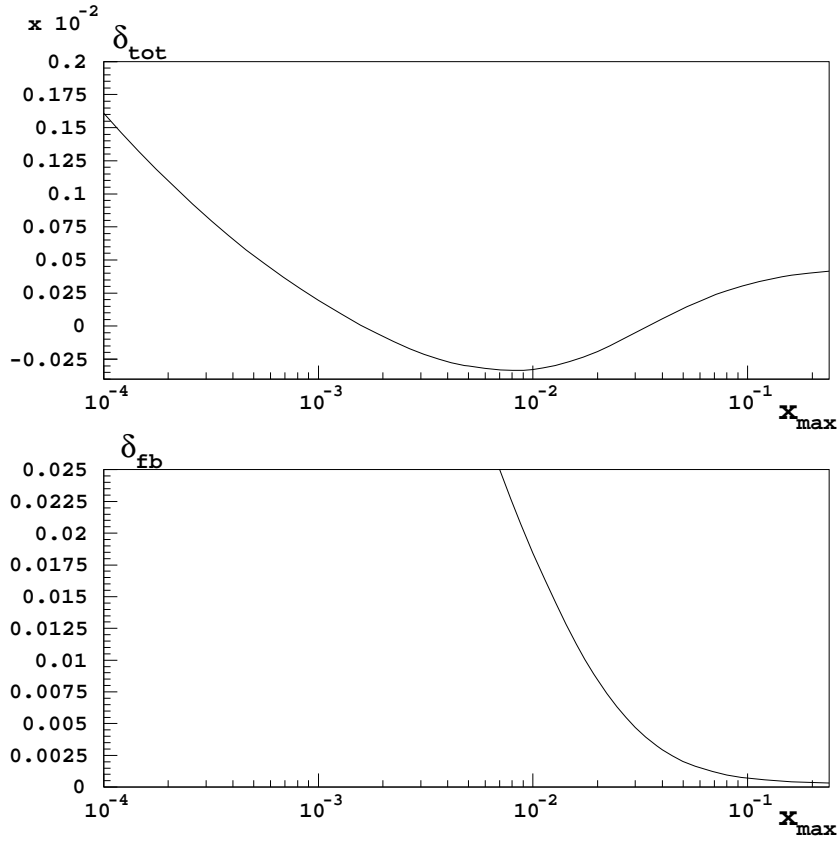


Figure 2.9: Contribution of the I-F QED interference for the total cross section and the forward-backward asymmetry at $\sqrt{s} = M_Z$ as a function of the cut on $s'_{min} \equiv s(1-x_{max})$, in the angular acceptance $|\cos\theta| < 0.9$.

These contributions are parameterized in δ_{tot} and δ_{fb} defined as:

$$\begin{aligned}\frac{\sigma^{if}}{\sigma^{nif}} &= 1 + \delta_{tot} \\ A_{fb}^{if} &= A_{fb}^{nif} + \delta_{fb}\end{aligned}$$

where σ^{if} and A_{fb}^{if} include the interference, whereas σ^{nif} and A_{fb}^{nif} don't include it. δ_{tot} and δ_{fb} have been computed using an analytic expression that describes the effect to $\mathcal{O}(\alpha)$, at a centre-of-mass energy $\sqrt{s} = 91.2$ GeV, and in the angular acceptance $|\cos\theta| < 0.9$.

What one can learn from fig. 2.9 is that as we try to become less inclusive ($x_{max} \rightarrow 0$), the effect of the interference is becoming less and less negligible. This is specially true for the forward-backward asymmetry, if we take into account that the experimental precision in the determination of A_{fb}^μ is around 0.01 [7].

The actual reason why the I-F QED interference is so small near the Z^0 peak is the finite lifetime of the Z^0 which, somehow, “separates physically” the initial and final state wavefunctions. Nevertheless, as we cut in radiated energy, the photon wavelength increases and then, radiation starts overlapping the initial and final state wavefunctions leading to a gradual restoration of the I-F QED interference with increasing strength of the cuts.

Indeed, this phenomenon was proposed some time ago by S. Jadach and Z. Was in ref. [16] as an alternative method to “determine” the Z^0 width. Very recently, the DELPHI collaboration has published a study on this topic [17].

In our case, we pretend to be as insensitive as possible to such kind of effects, in order not to spoil the interpretation of $\sqrt{s'}$ as the “effective” centre-of-mass energy left after ISR. So that, instead of dealing with the probability density of equation 2.17, we have to bin the distribution in intervals of x with a minimum bin size of the order of $\Delta x \sim \frac{\Gamma_Z}{M_Z} \sim 0.03$. In any case, one needs to bin the probability density in the limit $x \rightarrow 0$ in order to have a finite answer.

- **Final State Radiation (FSR).** Contribution from diagrams in which a photonic line is attached to the final state fermion line (see figure 2.10). In this set of contributions, the infrared divergence which shows up in the real photon

emission when the photon energy vanishes, cancels the infrared divergence present in the interference between the Born amplitude and the one in which a virtual photon is attached to the final state vertex (vertex correction). If we don't cut on the phase space of the final state photon, the correction for the total cross-section ($\hat{\sigma}$) is $(1 + \frac{3\alpha(s)}{4\pi})$ and negligible for the antisymmetric cross-section ($\hat{\sigma}_{fb}$). This amounts to a correction at the level of 0.17% at energies around the Z^0 mass.

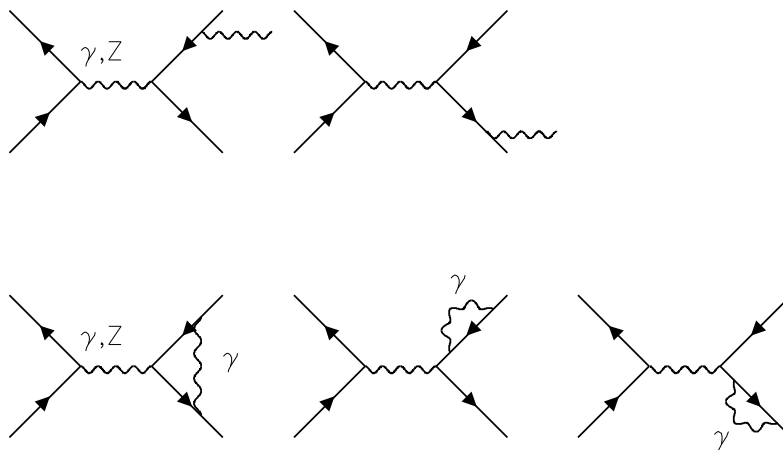


Figure 2.10: QED Final State corrections

2.2 Model independent approaches to the process $e^+e^- \rightarrow \mu^+\mu^-$

In the previous section, we have seen how the process $e^+e^- \rightarrow \mu^+\mu^-$ can be described at lowest order by two quantities: $\sigma^0(s)$ and $A_{fb}^0(s)$ that are “in principle” measurable. The explicit dependence of these quantities with the centre-of-mass energy is predicted by the SM (see equations 2.4, 2.5). The inclusion of higher order non photonic corrections does not change this picture and we can just absorb them in a redefinition of the cross section ($\hat{\sigma}(s)$ and $\hat{A}_{fb}(s)$).

To interpret $\hat{\sigma}(s)$ and $\hat{A}_{fb}(s)$ in a “model independent” way, we need to parameterize the energy dependence of these observables in such a way that it copes with

the experimental accuracy, and has the minimum input from the theory. Since almost the beginning of LEP, the “effective coupling” language has been established by the LEP community as a suitable way to compile the precision electroweak measurements. In fact, this language is adequate when we are describing a restricted energy region around the Z^0 resonance, but as we will see, we need a more general approach to describe an energy region spanning from 60 GeV up to 140 GeV. This is the motivation to introduce the so-called S-matrix language.

2.2.1 The effective coupling language

As we have seen in section 2.1, the inclusion of the leading non-photonic corrections does not change at all the Born structure of the SM predictions. The “effective coupling” language takes profit of this, and parameterizes $\hat{\sigma}(s)$ and $\hat{A}_{fb}(s)$ as a function of two real constant parameters per flavour: an effective vector coupling ($\Re(g_V)$) and an effective axial coupling ($\Re(g_A)$).

In fact, one can absorb higher order non-photonic corrections in formulae 2.4 and 2.5 with just some simple replacements, namely:

$$\begin{aligned}
 \alpha &\rightarrow \alpha(s) \text{ Real part of } \gamma \text{ self-energy} \\
 s(s - M_Z^2) &\rightarrow s(s - M_Z^2) + s^2 \frac{\Gamma_Z}{M_Z} \Im(\Delta\alpha) \text{ Imaginary parts of } \gamma \text{ self-energy and } g_{A(V)} \\
 |Z(s)|^2 &\rightarrow (s - M_Z^2)^2 + \left(s \frac{\Gamma_Z}{M_Z}\right)^2 \text{ Imaginary part of } Z \text{ self energy} \\
 v, a &\rightarrow \sqrt{F_G(s)} \Re(g_V), \\
 &\quad \sqrt{F_G(s)} \Re(g_A) \text{ Real part of } Z \text{ self-energy, } \gamma - Z \text{ mixing, weak vertices}
 \end{aligned}$$

where

$$F_G(s) = \frac{G_F M_Z^2}{2\sqrt{2}\pi\alpha(s)} \quad (2.20)$$

$\Im(\Delta\alpha)$ can be neglected in the total cross section, but it turns out to be relevant in the antisymmetric cross section [15],[18]. The explicit expression is

$$\Im(\Delta\alpha) = \frac{\Im(\Pi^\gamma(s))}{1 + \Re(\Pi^\gamma(s))} + 2 \frac{\Im(g_A)}{\Re(g_A)} + 2\Im(F_{V\gamma}) \quad (2.21)$$

where $\Pi^\gamma(s)$ is the γ self-energy and $F_{V\gamma}$ is the vertex corrections to the electromagnetic coupling.

In this way, we can replace $\sigma^0(s)$ ($A_{fb}^0(s)$) by $\hat{\sigma}(s)$ ($\hat{A}_{fb}(s)$), in equation 2.4 (equation 2.5).

By construction this language is an almost-model-independent language in which the only underlying assumptions are (a part from the description of photonic radiation by QED) just basic concepts of quantum field theory and the hypothesis that the interaction is mediated by the exchange of two bosons, a massless photon with vector coupling to the electric charge, and a massive Z boson with both vector and axial couplings to fermions. In addition, from the theoretical point of view, the accuracy of this language has been studied in great detail and its validity beyond the experimental precision has been established [14], [19].

On the other hand, if we want to describe a wide region of energies, and not only a limited energy region around the Z^0 pole, we find that this language is not adequate. The problem arises from the $\gamma - Z$ interference terms in equation 2.4 and equation 2.5, that becomes more and more important as we are moving away from the Z^0 resonance. These terms are not independent parameters in this language, because they are just function of the effective couplings mainly determined at the Z^0 peak.

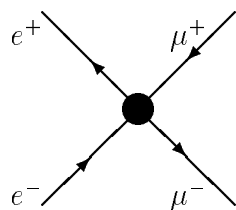
This problem is specially relevant in the case of the energy dependence of the forward-backward asymmetry. As we have already mentioned, the non-zero asymmetry that we observe when moving away from the Z^0 pole is a consequence of the $\gamma - Z$ interference term, that on the other hand is just a function of the weak axial coupling, as can be seen in equation 2.5. The axial coupling is determined with high precision from the measured total cross section at the Z^0 peak, because $\hat{\sigma}(M_Z^2) \propto ((\Re(g_{V_e}))^2 + (\Re(g_{A_e}))^2)((\Re(g_{V_\mu}))^2 + (\Re(g_{A_\mu}))^2)$ and for $(\Re(g_{V_l}))^2 \ll (\Re(g_{A_l}))^2$, the lepton lineshape measures basically $(\Re(g_{A_e}))^2(\Re(g_{A_\mu}))^2$. So that, even if there was some new physics beyond the SM that could modify such energy dependence, this will not be visible in this language !

So, if we are going to describe a wide range of energies, we need to treat the energy dependence of $\hat{\sigma}(s)$ and $\hat{A}_{fb}(s)$ in a model independent way. This is what the S-matrix approach basically does.

2.2.2 The S-matrix language

The S-Matrix ansatz allows a consistent parameterization of the energy dependence of the LEP cross sections and asymmetries because its underlying basic concept is an expansion around the Z^0 pole on the energy dependence. It is a rigorous, well defined and well documented [20] approach that allows to fit the data in a more general way than the one using the “effective coupling” language since it does not assume any a priori relation between on-resonance measurements and energy dependences, which is something unavoidable in the “effective coupling” language.

Assuming that the S-matrix element that describes the process $e^+e^- \rightarrow \mu^+\mu^-$ is analytic (so it can be expanded in a Laurent serie), and that there are only two poles in the complex plane (corresponding to the Z-boson and γ -boson in the SM), one can write in a completely general way the S-matrix amplitude for this process as is shown in figure 2.11.



$$\begin{aligned} \mathcal{M} &\equiv \frac{R_\gamma}{s} + \frac{R_Z}{s-s_Z} + F(s) \\ s_Z &\equiv \overline{M}_Z^2 - i\overline{\Gamma}_Z\overline{M}_Z \end{aligned}$$

Figure 2.11: Schematic representation of the S-matrix ansatz

The poles of \mathcal{M} have complex residua R_Z and R_γ , the latter corresponding to the photon, and $F(s)$ is an analytic function without poles.

Note that now \overline{M}_Z corresponds to the real part of the complex pole s_Z . In fact, the relation between \overline{M}_Z and the usual definition of M_Z in terms of the Breit-Wigner propagator can be found very easily to be:

$$\overline{M}_Z \equiv \frac{M_Z}{\sqrt{1 + \left(\frac{\Gamma_Z}{M_Z}\right)^2}} \quad (2.22)$$

$$\overline{\Gamma}_Z \equiv \frac{\Gamma_Z}{\sqrt{1 + \left(\frac{\Gamma_Z}{M_Z}\right)^2}} \quad (2.23)$$

after a redefinition of the real Fermi coupling constant that appears in the normalization of the weak amplitude, being now a complex number with $\overline{G}_F = G_F/(1 + i\frac{\Gamma_Z}{M_Z})$.

This is so, because

$$\begin{aligned}
\frac{G_F}{(s - M_Z^2 + is\frac{\Gamma_Z}{M_Z})} &= \frac{\overline{G}_F(1 + i\frac{\Gamma_Z}{M_Z})}{(s - M_Z^2 + is\frac{\Gamma_Z}{M_Z})} \\
&= \frac{\overline{G}_F}{s - \frac{M_Z^2 - iM_Z\Gamma_Z}{1 + (\frac{\Gamma_Z}{M_Z})^2}} \\
&= \frac{\overline{G}_F}{s - \overline{M}_Z^2 + i\overline{M}_Z\overline{\Gamma}_Z}
\end{aligned}$$

and this demonstrates equations 2.22 and 2.23. Note that the ratio between Γ_Z and M_Z is exactly the same in both definitions.

If one compares the amplitude \mathcal{M} in figure 2.11 with the SM predictions after including one loop non-photonic corrections, one can see that the structure of both amplitudes is exactly the same with $F(s) = 0$, (neglecting the energy dependence of the “effective couplings” and the contribution of the weak boxes). In other words, the only contributions to $F(s)$ in the SM, are those that cannot be absorbed in the definition of the “effective couplings”, that at one loop correspond to the inclusion of the weak boxes diagrams, (see figure 2.4). As we have already seen, they can be neglected safely at the present level of experimental accuracy.

Now, if the four helicity amplitudes that describe the process $e^+e^- \rightarrow \mu^+\mu^-$ are written in this approximation,

$$\mathcal{M}^{ij} \equiv \frac{R_\gamma}{s} + \frac{R_Z^{ij}}{s - s_Z} \quad (2.24)$$

where i (j) stands for the polarization of the incoming e^- (outgoing μ^-), it is straightforward to show (see appendix A),

$$\hat{\sigma}_{ij}(s) \equiv \frac{s}{2} |\mathcal{M}^{ij}|^2 = \frac{2}{3}\pi\alpha^2 \left[\frac{r^\gamma}{s} + \frac{sr_{ij} + (s - \overline{M}_Z^2)J_{ij}}{(s - \overline{M}_Z^2)^2 + \overline{M}_Z^2\overline{\Gamma}_Z^2} \right] \quad (2.25)$$

and therefore the total cross section defined as $\hat{\sigma} = \frac{1}{2}(\hat{\sigma}_{LL} + \hat{\sigma}_{RR} + \hat{\sigma}_{LR} + \hat{\sigma}_{RL})$ will be

$$\hat{\sigma}(s) = \frac{4}{3}\pi\alpha^2 \left[\frac{r^\gamma}{s} + \frac{sr_{tot} + (s - \overline{M}_Z^2)J_{tot}}{(s - \overline{M}_Z^2)^2 + \overline{M}_Z^2\overline{\Gamma}_Z^2} \right] \quad (2.26)$$

while the antisymmetric cross section defined as $\hat{\sigma}_{fb} = \frac{3}{8}(\hat{\sigma}_{LL} + \hat{\sigma}_{RR} - \hat{\sigma}_{LR} - \hat{\sigma}_{RL})$ will be

$$\hat{\sigma}_{fb}(s) = \pi\alpha^2 \left[\frac{sr_{fb} + (s - \overline{M}_Z^2)J_{fb}}{(s - \overline{M}_Z^2)^2 + \overline{M}_Z^2\overline{\Gamma}_Z^2} \right] \quad (2.27)$$

So that, these equations parameterize $\hat{\sigma}$ and $\hat{\sigma}_{fb}$ in an almost model independent way as a function of 6 real parameters: M_Z , Γ_Z , r_{tot} , J_{tot} , r_{fb} and J_{fb} , (the pure QED contribution r^γ is fixed to the SM predictions). Equations 2.22 and 2.23 are used in order to recover the usual definition of the Z^0 mass and width.

The expressions that relate the coefficients r and J in these equations to the helicity amplitudes are given explicitly in appendix A. The total cross section $\hat{\sigma}(s)$ needs to be corrected with a factor $(1 + \frac{3}{4\pi}\alpha(M_Z^2))$ which takes into account the possibility to radiate a photon in the final state.

The SM predictions for the helicity amplitudes are given in appendix A, and in an approximate way can be related with the real part of the effective couplings through

$$\begin{aligned} r_{tot} &\propto ((\Re(g_{V_e}))^2 + (\Re(g_{A_e}))^2)((\Re(g_{V_\mu}))^2 + (\Re(g_{A_\mu}))^2) \\ J_{tot} &\propto \Re(g_{V_e})\Re(g_{V_\mu}) \\ r_{fb} &\propto \Re(g_{A_e})\Re(g_{V_e})\Re(g_{A_\mu})\Re(g_{V_\mu}) \\ J_{fb} &\propto \Re(g_{A_e})\Re(g_{A_\mu}) \end{aligned}$$

Introducing the measured M_{top} by CDF and D0 collaborations [12] ($M_{top} = 175 \pm 6$ GeV) and the most probable mass range determined for M_H [7] ($66 < M_H < 300$ GeV), and fixing the input values to be ($M_Z = 91.1863$ GeV, $\alpha^{-1}(M_Z^2) = 128.896 \pm 0.090$), the SM predictions for these parameters are shown in table 2.1, where the error corresponds to the variation induced by the error on $\alpha^{-1}(M_Z^2)$, on the top mass and the unknowledge of M_H .

The number of digits quoted in table 2.1 have been chosen to match with the experimental accuracy. From these numbers one can see that the parameters that describe the energy dependence of the total cross section (J_{tot}) and antisymmetric cross section (J_{fb}) have negligible sensitivity to the top and Higgs masses. They are determined in the SM by the interference between the photon and the Z-boson, so they can be used to test any new contribution beyond the SM that can interfere with the Z-boson.

In figure 2.12 there's a comparison between the predictions of the S-matrix ansatz with the actual SM predictions at one loop using the BHM EW libraries [21],

M_Z (GeV)	=	91.1863
Γ_Z (GeV)	=	$2.4974 \pm 0.0006 \pm 0.0014^{+0.0024}_{-0.0018}$
r_{tot}	=	$0.14298 \pm 0.00004 \pm 0.00019^{+0.00022}_{-0.00014}$
J_{tot}	=	$0.004 \pm 0.000 \pm 0.000 \pm 0.000$
r_{fb}	=	$0.00278 \pm 0.00008 \pm 0.00007^{+0.00013}_{-0.00015}$
J_{fb}	=	$0.800 \pm 0.001 \pm 0.000 \pm 0.000$

Table 2.1: SM predictions for the S-matrix parameters for $M_Z = 91.1863$ GeV, $\alpha^{-1}(M_Z^2) = 128.896 \pm 0.090$, $M_{top} = 175$ GeV and $M_H = 150$ GeV. The first error corresponds to the uncertainty in $\alpha^{-1}(M_Z^2)$. The second error corresponds to the variation of the top mass in the range $169 < M_{top} < 181$ GeV and the third of the Higgs mass in the range $66 < M_H < 300$ GeV.

in the energy range of interest in this work. One can see from this figure that at energies around the Z^0 pole, the precision is better than the permille level, and at energies below it is always much better than 0.5%. At energies above the Z^0 pole, the precision is a little bit worse but always better than the 1% level, while the only data available at those energies before LEP II started was 5 pb^{-1} taken in November of 1995 at energies around 130-136 GeV. The statistical precision at these energies is at the level of 10 – 20%, so the S-matrix ansatz copes perfectly with the experimental accuracy in all the energy range.

2.3 Beyond the Standard Model. Z' physics

Despite the excellent performance of the SM so far, there is a general consensus that it is not the “final” theory (if something like that exist). Most of the attempts to unify the strong and electroweak interactions predict additional neutral heavy gauge bosons Z' (see for instance [22]). New interference terms, as $\gamma - Z'$ and $Z - Z'$ will appear at the Born level and will modify the cross-section and angular distribution at energies far from $\sqrt{s} \sim M_Z$. In this sense, a new gauge boson is the most obvious candidate to modify the predicted energy dependence.

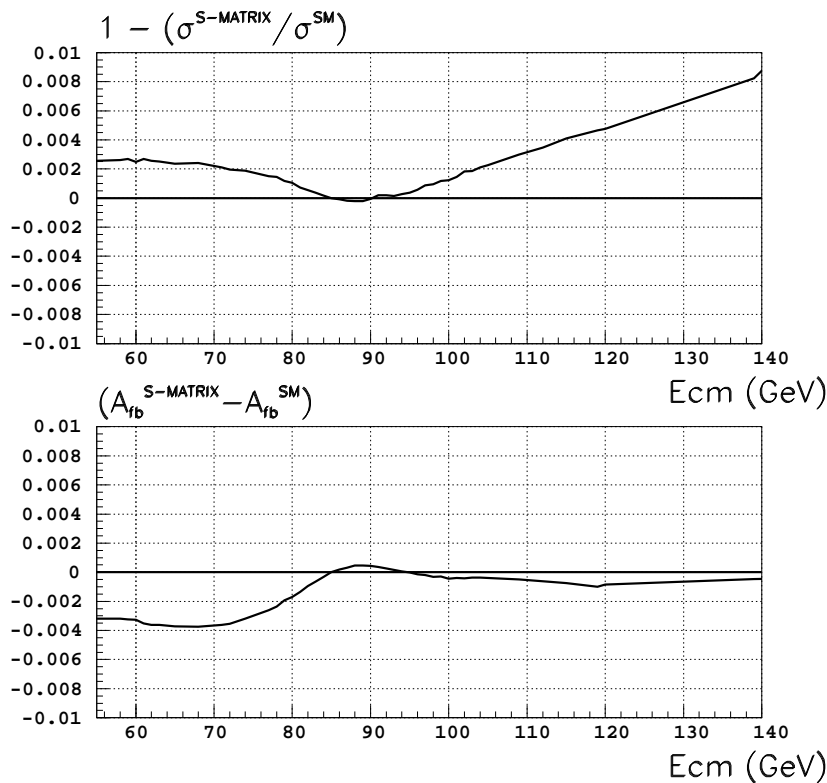


Figure 2.12: Comparison of the S-matrix ansatz with the SM predictions as a function of the centre-of-mass energy. The S-matrix parameters are those shown in table 2.1.

In principle, the Z' influences cross sections in three different ways:

- virtual Z' exchange (also present without ZZ' mixing). For sufficiently large Z' masses the main effect is seen only in the interference terms.
- shift of the mass of the standard Z boson seen at LEP I due to the ZZ' mixing.
- modifications of the couplings of the standard Z boson due to the ZZ' mixing.

The existence of a Z' would mean that the observed mass eigenstate at LEP I needs to be considered as a mixture of the unmixed Z^0 and $Z^{0'}$, predicting a shift in M_Z from its SM value, with the mixing described by a matrix using the mixing

angle θ_3 :

$$\begin{pmatrix} Z \\ Z' \end{pmatrix} = \begin{pmatrix} \cos \theta_3 \sin \theta_3 \\ -\sin \theta_3 \cos \theta_3 \end{pmatrix} \begin{pmatrix} Z^0 \\ Z^{0'} \end{pmatrix}$$

The angle θ_3 is related to the mixed masses M_Z and $M_{Z'}$, and the light unmixed mass M_0 as follows:

$$\tan^2 \theta_3 = \frac{M_0^2 - M_Z^2}{M_{Z'}^2 - M_0^2}$$

The mass M_0 (that corresponds to M_Z in the SM), is related to the weak mixing angle and M_W in the SM expression:

$$M_0 = \frac{M_W}{\sqrt{\rho} \cos \theta_W}$$

where ρ is the usual electroweak parameter ($\rho = 1$ at lowest order).

There are several extensions to the SM that predict a hypothetical additional gauge boson. The most ‘‘popular’’ models among experimentalists are superstring-inspired models based on the E_6 symmetry group and ‘‘left-right’’ symmetric models.

- **E_6 models.** In this kind of models [23], E_6 is the group of gauge symmetries that is broken at the Planck scale as

$$\begin{aligned} E_6 &\rightarrow \text{SO}(10) \otimes \text{U}(1)_\psi \\ &\rightarrow \text{SU}(5) \otimes \text{U}(1)_\chi \otimes \text{U}(1)_\psi \end{aligned}$$

in which the $\text{SU}(5)$ contains the standard $\text{SU}(3)_C \otimes \text{SU}(2)_L \otimes \text{U}(1)_Y$. If there is one extra low-energy Z , it must be a linear combination of Z_χ and Z_ψ , i.e.,

$$Z(\theta_6) = Z_\chi \cos \theta_6 + Z_\psi \sin \theta_6$$

The mixing angle θ_3 and the ‘‘model’’ angle θ_6 completely determine the couplings of the Z and Z' to leptons, trough the gauge structure of the theory. Vector and axial couplings of leptons to the Z boson and the extra neutral gauge boson, at first order in θ_3 , are given by:

$$\begin{aligned} v_l &= \frac{I_3^l + 2 \sin^2 \theta_W - \frac{1}{2} \theta_3 \sin \theta_W (\cos \theta_6 - \sqrt{\frac{5}{3}} \sin \theta_6)}{2 \sin \theta_W \cos \theta_W}, \\ a_l &= \frac{I_3^l - \theta_3 \sin \theta_W (\frac{1}{6} \cos \theta_6 + \frac{1}{2} \sqrt{\frac{5}{3}} \sin \theta_6)}{2 \sin \theta_W \cos \theta_W} \end{aligned} \quad (2.28)$$

and

$$\begin{aligned} v'_l &= \frac{-\theta_3(-\frac{1}{2} + 2 \sin^2 \theta_W) - \frac{1}{2} \sin \theta_W (\cos \theta_6 - \sqrt{\frac{5}{3}} \sin \theta_6)}{2 \sin \theta_W \cos \theta_W}, \\ a'_l &= \frac{-\frac{1}{2} \theta_3 - \sin \theta_W (\frac{1}{6} \cos \theta_6 + \frac{1}{2} \sqrt{\frac{5}{3}} \sin \theta_6)}{2 \sin \theta_W \cos \theta_W} \end{aligned} \quad (2.29)$$

The most popular choices correspond to $\theta_6 = 0, \pi/2$ and $-\arctan(\sqrt{5/3})$ that define the chi-model ($E_6(\chi)$), the psi-model ($E_6(\psi)$) and the eta-model ($E_6(\eta)$) respectively.

- **L-R models.** Left-right symmetric extensions of the SM were first proposed [24] to explain the origin of parity violation in low energy physics. The approach consists in considering a lagrangian intrinsically left-right symmetric, the asymmetry observed in nature arising from a non invariant vacuum under parity symmetry. The gauge group of the model is $SU(2)_L \otimes SU(2)_R \otimes U(1)$. The quantum number associated to the $U(1)$ factor can be identified with $B-L$, B and L being the baryon and lepton numbers.

Another interesting feature of the left-right model is the possibility of explaining the smallness of the neutrino masses [25]. The presence of the right-handed neutrinos, which has no counterpart in the SM, and of a suitable Higgs structure allows for the so called see-saw mechanism to take place and naturally accounts for very light left-handed neutrinos.

The parameter α_{LR} describes the couplings of the heavy bosons to fermions, and it can be expressed in terms of the $SU(2)_{L,R}$ coupling constants $g_{L,R}$ and the weak mixing angle, trough

$$\alpha_{LR} \equiv \sqrt{\frac{\cos^2 \theta_W - \lambda^2 \sin^2 \theta_W}{\lambda \sin^2 \theta_W}} \quad (2.30)$$

with

$$\lambda \equiv \frac{g_L}{g_R} \quad (2.31)$$

The new neutral current is defined with

$$Z(\alpha_{LR}) = \alpha_{LR} Z_R - \frac{1}{2\alpha_{LR}} Z_{B-L}$$

following the convention adopted in the Particle Data Book [26].

For α_{LR} at its lower bound of $\sqrt{2/3}$, the L-R model is identical to the $E_6(\chi)$ model. The upper bound corresponds to $g_L = g_R$ with a value around $\alpha_{LR} \sim 1.53$. We have chosen an intermediate value of $\alpha_{LR} = 1$ as example.

After specifying the model (and without any assumption on the structure of the Higgs sector), only two free parameters remain: i) the mixing angle θ_3 between Z and Z' , ii) and the mass of the heavier-mass eigenstate, $M_{Z'}$. If we want to test one of these particular models, and extract the corresponding limits on these parameters, we can replace the model independent parameterization of $\hat{\sigma}(s)$ and $\hat{\sigma}_{fb}(s)$ by the specific prediction of the model as a function of $M_{Z'}$ and θ_3 .

Figure 2.13 shows the deviations in the non-photonic corrected cross sections and forward-backward asymmetries predicted by these four models. The Z' mass is fixed to $M_{Z'} = 250$ GeV, that is close to the limit of exclusion at 95% confidence level for the most sensitive model ($E_6(\chi)$). The mixing angle (θ_3) is fixed to zero because the existing limits are already very constraining [27].

In the energy range near to the Z^0 pole position, the additional bosons direct contribution to the cross section and forward-backward asymmetry is very small. The deviations from SM expectations arise primarily from interference effects of the hypothesized bosons and the existing ones (γ and Z^0). This is seen specially clear in the case of the forward-backward asymmetry at energies around $\sqrt{s} \sim 85$ GeV.

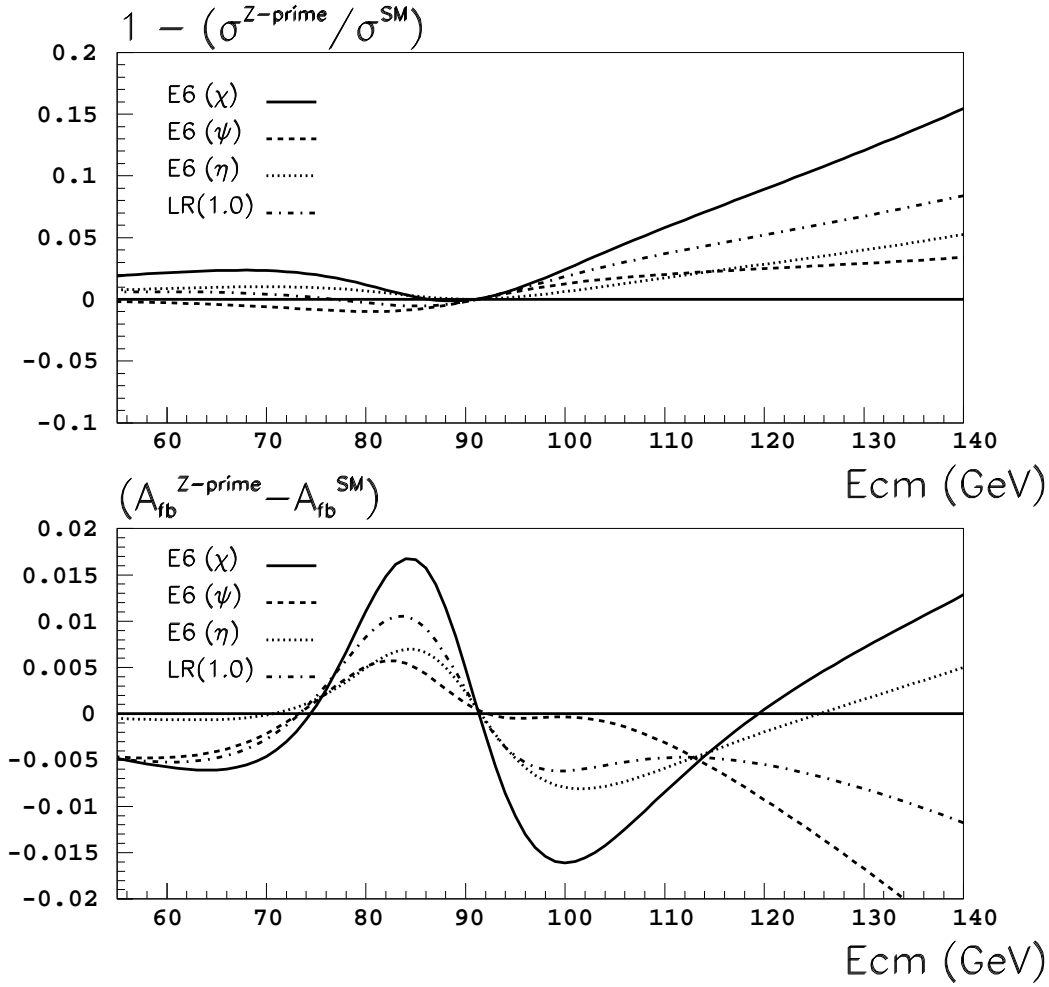


Figure 2.13: Deviation of $\hat{\sigma}$ and $\hat{\sigma}_{fb}$ with respect the SM predictions, for several Z' models. $M_{Z'}$ is fixed to 250 GeV, and the mixing angle θ_3 is fixed to zero.

Chapter 3

The ALEPH detector

The ALEPH detector [28] is one of the four large detectors installed in the LEP collider. The other experiments are DELPHI [29], L3 [30] and OPAL [31]. It has been designed as a general purpose detector for e^+e^- interactions: to study in detail the parameters of the Standard Model, to test QCD at large Q^2 and to search for new phenomena (such as the Higgs boson or supersymmetric particles). Therefore, the detector has been conceived to have good track momentum resolution, fine calorimetric granularity, covering as much solid angle as possible and with good hermiticity.

In this chapter we briefly describe the LEP collider and the beam parameters: beam energy, energy spread... that will be relevant in the analysis. A general description of the ALEPH apparatus with special emphasis in those subdetectors used in the analysis is made in section 3.2. A brief description of the actual event reconstruction and simulation in ALEPH is made in section 3.3.

3.1 The LEP collider

The LEP (Large Electron Positron collider) machine is an e^+e^- storage ring of 27 Km. of circumference sited at the European Centre for Particle Physics (CERN) in Geneva, Switzerland. It is located in a tunnel at a depth between 80 m. and 137 m. spanning the French and Swiss territories, (see figure 3.1). It is the largest collider ever built and the reason for its size is the synchrotron radiation, which is proportional to the square of the inverse mass of the particle and to the fourth power of its energy. So that, for massive particles as protons it can be neglected

but it is fierce for very light particles as electrons. It is also inversely proportional to the square of the radius of the machine, so becomes manageable at high energy circular colliders only if the radius is sufficiently large.

The beams that circulate around the ring are formed by bunches of electrons and positrons. They are accelerated in opposite directions and cross in eight or sixteen points in case the number of bunches per beam is four or eight, respectively, although they are steered to collide every $22 \mu\text{s}$ (or $11 \mu\text{s}$) only in the four points where the detectors are installed. The collisions in the other points are avoided by a system of electrostatic separators. This scheme worked very well and luminosities¹ at the level of $1\text{-}2 \cdot 10^{31} \text{cm}^{-2} \text{s}^{-1}$ have been achieved in the first phase of the accelerator program at energies around 91 GeV (LEP-I phase), producing around 4 million visible Z^0 decays per experiment.

Since November 1995, a new scheme was adopted, in order to increase even more the luminosity, where in fact there were four trains of up to four bunches colliding at each interaction point. This scheme is expected to achieve luminosities up to $5\text{-}6 \cdot 10^{31} \text{cm}^{-2} \text{s}^{-1}$, and compensate in some way the small cross section expected at energies around 180 GeV, just above the W-pair threshold (LEP-II phase).

The LEP injection chain can be seen in figure 3.2. It starts with the LINear ACcelerator (LINAC) which accelerates electrons and positrons in two stages. The electrons are first accelerated up to 200 MeV. Part of the electrons are used to produce positrons and the rest, together with the positrons are accelerated up to 600 MeV. Then, the particles are inserted into a small circular e^+e^- accelerator, the Electron Positron Accumulator (EPA), where they are accumulated until the electron and positron intensities achieve the nominal value. Afterwards, they are inserted in the Proton Synchrotron (PS) accelerator achieving an energy of 3.5 GeV. Then, the particles are injected into the Super Proton Synchrotron (SPS) storage ring, reaching an energy of 20 GeV, and finally, they are injected into the LEP main ring and accelerated to an energy of ~ 45 GeV with a current up to 6 mA per beam.

¹the number of events per unit of time per unit of cross section

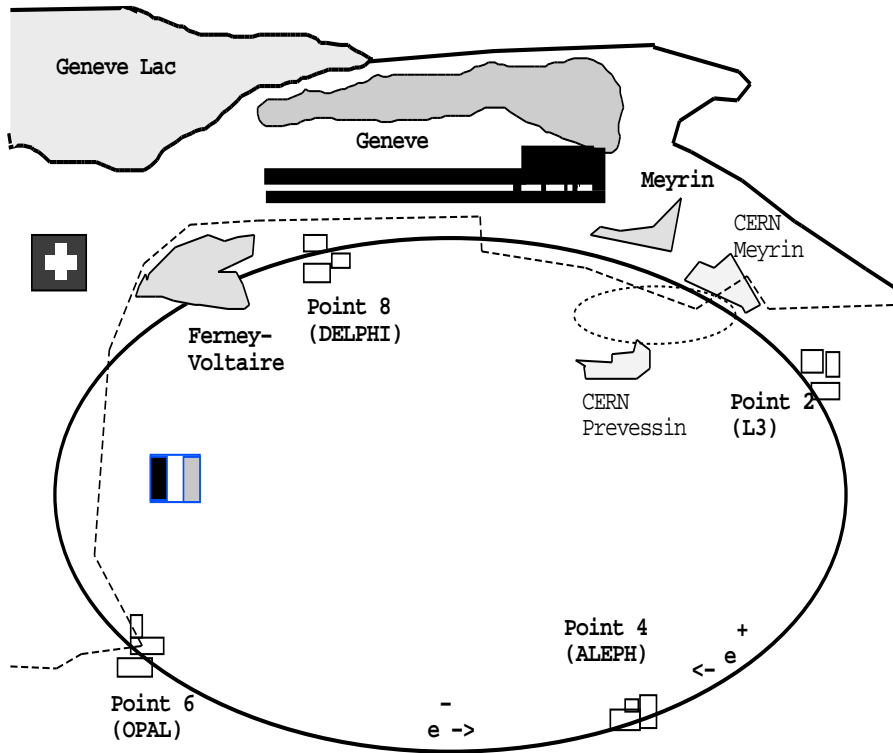


Figure 3.1: Schematic representation of the LEP ring

3.1.1 Determination of the beam energy

The determination of the LEP beam energy constitutes the highest precision measurement performed at LEP so far, and allows to determine M_Z and Γ_Z with an unprecedented precision. Since 1992, the method used to measure the beam energy in LEP-I takes advantage of the fact that, under favourable conditions, transverse beam polarization can be naturally built up in a circular machine due to the interaction of the electrons with the magnetic guide field (Sokolov-Ternov effect [32]). The number of spin precession in one turn around the ring (“spin tune”) is

$$\nu = \frac{g_e - 2}{2} \frac{E_{\text{beam}}}{m_e} = \frac{E_{\text{beam}} \text{ (GeV)}}{0.4406486(1)}$$

where g_e is the gyromagnetic constant and m_e is the electron mass. This relation is exact only for ideal storage rings, and needs to be corrected by small imperfections. In this approximation, the spin precession frequency is equal to

$$f_{\text{prec}} = \nu f_{\text{rev}}$$

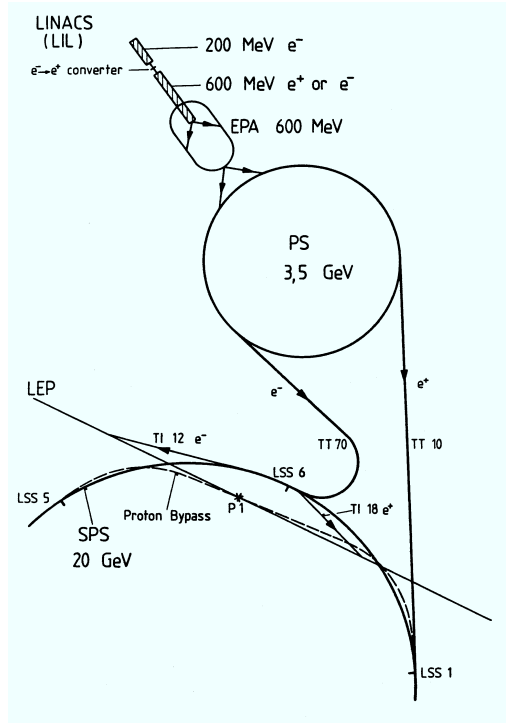


Figure 3.2: Schematic representation of the LEP injectors and accelerators

with f_{rev} the revolution frequency being in typical conditions of $f_{rev} = 11245.5041(1)$ Hz. From the above equations, it is clear that this spin precession frequency (f_{prec}) is predicted with a very high precision as a function of the beam energy. On the other hand, this frequency can be measured using a sweeping kicker magnet which produces an exciting field perpendicular to the beam axis and in the horizontal plane. Then, when $f_{spin-kick} = (n \pm \nu)f_{rev}$ (n integer), that is when the exciting field is in phase with the spin precession, the spin rotations about the radial direction add up coherently from turn to turn. About 10^4 turns (~ 1 second) are needed to turn the polarization vector in the horizontal plane (resonant depolarization). In this way, by plotting the measured beam polarization versus $f_{spin-kick}$, one can determine f_{prec} with a precision which corresponds to an accuracy on the beam energy at the level of 0.2 MeV. This method is often referred to as *energy calibration by resonant depolarization* and has been used extensively for accurate beam energy calibrations and measurements of particle masses [33].

Nevertheless, since just about 2 calibrations per week are, in practice, feasible, this means that these very precise measurements, have to be extrapolated to the

whole running time by correlating them with the energy measurements performed by using some reference magnets. The scatter in this correlation, depends on the stability of the machine energy and is affected by several variables, such as the status of the radiofrequency cavities, the temperature and humidity in the LEP tunnel, the distortions of the ring length, and even by current flow over the vacuum chamber created by trains travelling between the Geneve main station and destinations in France [34]!!!

For instance, due to the tidal forces of the sun and the moon, the circumference of the machine changes by just ~ 1 mm, but they affect the beam energy at the few MeV level (see figure 3.3). The final precision of the measurement improves as these effects are understood and at present is of about 1.5 MeV.

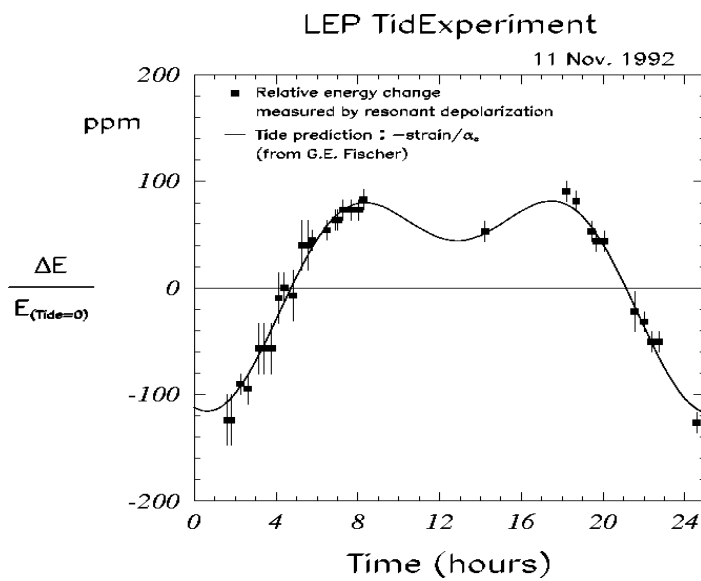


Figure 3.3: Relative change in parts per million of LEP energy during 24 hours as a result of the tide

Note that this measurement of the beam energy corresponds to the mean beam energy of the electrons and positrons inside each bunch. The energy of the individual electrons (or positrons) is distributed with a gaussian probability density, with a

beam energy spread of around 39 MeV [35] that is much bigger than the error on the mean energy. The energy spread of the beams is determined from the measurement of the length of the luminous region, (σ_Z), through the relation:

$$\sigma_{bs} = \frac{\sqrt{s}}{\alpha R} Q_s \sigma_Z$$

where α is the momentum compaction factor ($\alpha \sim 0.00019$), R is the LEP mean radius ($R \sim 4242.893$ m) and Q_s is the Synchrotron tune ($Q_s \sim 0.065$). In this way, the collision energy is gaussian-distributed with an energy spread about² $\sqrt{2} \times 39$ MeV ~ 55 MeV. So that, although the mean energy is known with very high precision (~ 1.5 MeV), the energy of each individual collision is distributed with a gaussian density probability with $\sigma \sim 55$ MeV.

3.2 The ALEPH apparatus

3.2.1 General description

The ALEPH detector (ALEPH: Apparatus for LEP PHysics) is located at experimental point number 4 in a cavern 143 m under the surface. It is a 12 m diameter by 12 m length cylinder positioned around the beam pipe (tube of 10 cm of radius). In the ALEPH reference system the z direction is along the beam line, positive in the direction followed by the e^- . The positive x direction points to the center of LEP, and is horizontal by definition. The positive y direction is orthogonal to z and x and is very close to vertical up.

The detector consist of subdetectors, each of one specialized in a different task. The inner volumes are devoted to perform accurate tracking of charged particles and to identify them using the ionization left in the detectors. They are immersed in a “strong” magnetic field of around 1.5 T, in order to achieve a good momentum resolution. The tracking volumes are surrounded by calorimeters, which are in two layers, an inner layer which measures electromagnetic, and an outer layer which measures hadronic energy. In fact, the calorimeters are the only subdetectors that can determine the energy and direction of neutral particles (except for neutrinos, that are able to traverse all the ALEPH subdetectors without leaving any signal).

²The factor $\sqrt{2}$ is a consequence of the convolution of the two gaussian distributions

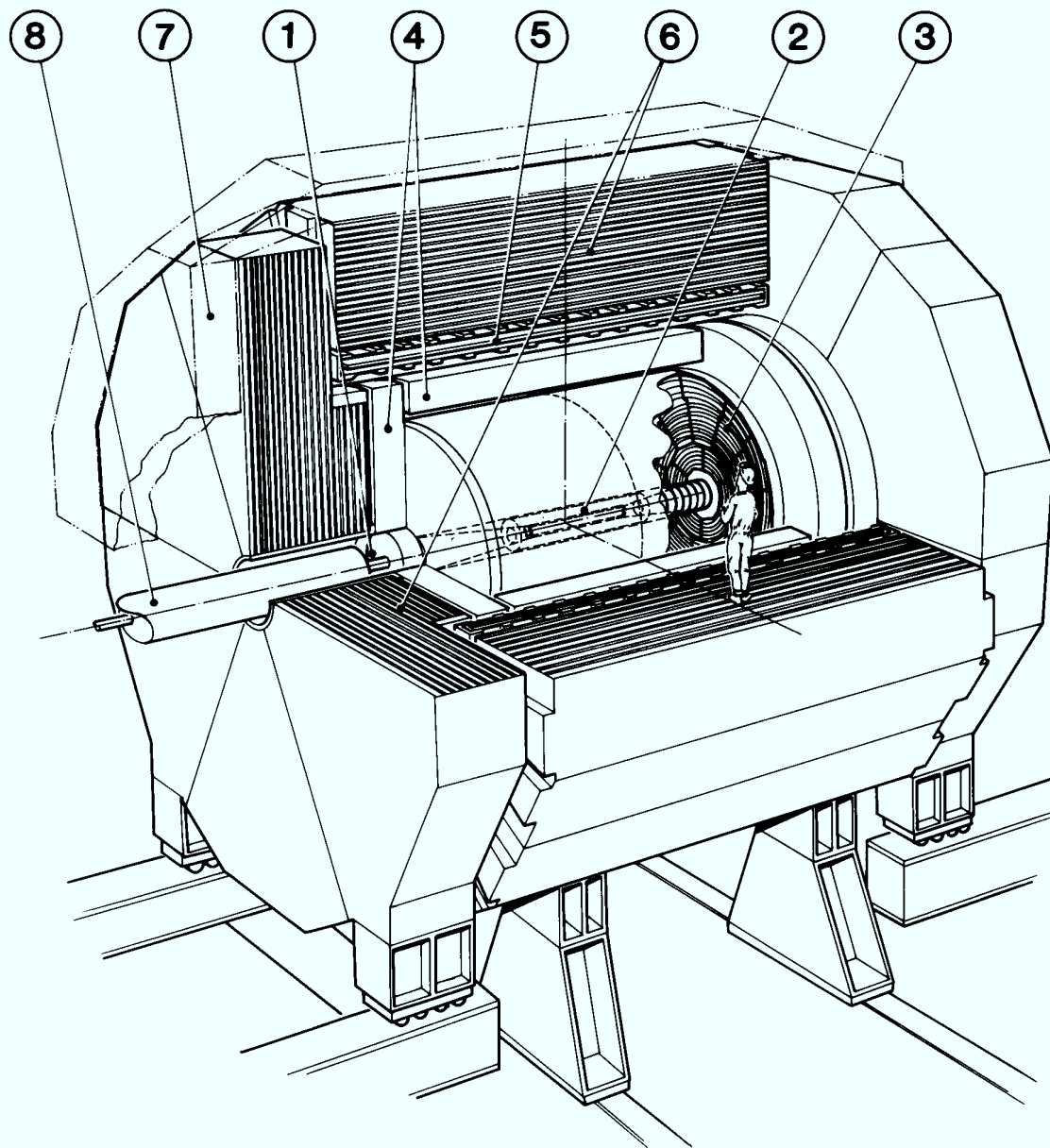


Figure 3.4: Schematic view of the ALEPH detector. (1) Luminosity monitor. (2) Silicon Microvertex Detector and Inner Tracking Chamber. (3) Time Projection Chamber. (4) Electromagnetic Calorimeter. (5) Superconducting Coil. (6) Hadronic Calorimeter. (7) Muon chambers. (8) Focusing Quadrupoles.

The whole is surrounded by wire chambers to detect the penetrating muons. Specialized detectors situated at very low angles from the beam direction, give a precise measurement of the luminosity. Figure 3.4 shows a schematic view of the ALEPH

detector.

Let's discuss briefly the ALEPH subdetectors. Following the order in which a particle leaving the interaction point would encounter them:

- The Vertex DETector (VDET), fully operational since the end of 1991, is a double sided silicon strip device with two layers of $r\phi$ and z strips around the beam pipe, providing a very accurate vertex tagging of tracks coming from the interaction point ($\sigma_{r\phi} = 10\mu m$, $\sigma_z = 13\mu m$). Since October 1995, a new vertex detector twice as long as the former one has been installed, extending the acceptance to lower polar angles, and with similar performance.
- The Inner Tracking Chamber (ITC) is a cylindrical multiwire drift chamber. It is used to provide up to eight precise $r\phi$ coordinates per track, with an average accuracy of $150\mu m$. It contributes to the global ALEPH tracking and is also used for triggering of charged particles coming from the interaction region.
- The Time Projection Chamber (TPC), the central track detector of ALEPH, is a very large three-dimensional imaging drift chamber. It provides a three dimensional measurement (up to 21 coordinate points) of each track (single coordinate resolution of $173\mu m$ in the azimuthal direction and $740\mu m$ in the longitudinal direction are achieved). From the curvature of the tracks in the magnetic field, the TPC gives a measurement of the transverse particle momenta, p_T , with an accuracy of $\Delta p_T/p_T^2 = 0.6 \times 10^{-3} (\text{GeV}/c)^{-1}$ at 45 GeV, if it is used together with the ITC and VDET. The chamber also contributes to particle identification through measurements of energy loss (dE/dx) derived from about 340 samples of the ionization for a track traversing the full radial range.
- The Electromagnetic CALorimeter (ECAL) is a sampling calorimeter consisting of alternating lead sheets and proportional wire chambers read out in projective towers to obtain a very high granularity (about $0.9^\circ \times 0.9^\circ$). It measures the energy and position of electromagnetic showers. The high granularity of the calorimeter leads to a good electron identification and allows to measure photon energy even in the vicinity of hadrons.
- The superconducting coil is a liquid-Helium cooled superconducting solenoid

creating, together with the iron yoke, a 1.5 T magnetic field in the central detector.

- The Hadronic CALorimeter (HCAL) is a sampling calorimeter made of layers of iron and streamer tubes. It provides the main support of ALEPH, the large iron structure serving both as hadron absorber and as return yoke of the magnet. It measures energy and position for hadronic showers and, complemented with the muon chambers, acts as a muon filter.
- The muon chambers (μ -chambers), outside HCAL, are two double layers of limited streamer tubes which identify muons and measure their directions.

An accurate luminosity measurement is absolutely necessary for the precise measurement of cross sections. Instead of computing it from the LEP machine parameters:

$$\mathcal{L} = \frac{N_{e^+} N_{e^-} f_{rev}}{4\pi \sigma_x \sigma_y} N_b$$

where N_e are the number of particles per bunch (typically of about 10^{12} at LEP), f_{rev} is the previously introduced revolution frequency and σ_x and σ_y are the beam transverse sizes (about $200 \mu m$ and $10 \mu m$ respectively), the LEP experiments determine the luminosity by counting the number of events coming from a process with very well known cross section, such the small angle Bhabha scattering ($e^+e^- \rightarrow e^+e^-$). The non-electromagnetic contributions to this process are small and its cross section for small angles is very high, namely

$$\sigma_{\text{Bhabha}} \sim \frac{16\pi\alpha^2}{s} \left(\frac{1}{\theta_{\min}^2} - \frac{1}{\theta_{\max}^2} \right)$$

From the above expression it follows directly that the precise knowledge of the detector inner edge radius is one of the fundamental milestones from the experimental point of view. From the total number of identified Bhabha events, the integrated luminosity follows as:

$$\int \mathcal{L} dt = \frac{N_{\text{Bhabha}} - N_{\text{Back.}}}{\epsilon \sigma_{\text{Bhabha}}}$$

where ϵ is the experimental efficiency and $N_{\text{Back.}}$ is the number of background events. It turns out that the present limitation in the knowledge of the luminosity is not

the experimental error, but it comes from the theoretical calculation of the prediction of the Bhabha cross section which, although being basically a QED problem, technically is a rather difficult task and is “just” known at the 0.11% level [36].

The ALEPH detector has three subdetectors installed around the beam pipe to detect small angle Bhabha scattering events:

- The Luminosity CALorimeter (LCAL) is a lead/wire calorimeter similar to ECAL in its operation. It consists of two pairs of semi-circular modules placed around the beam pipe at each end of the detector. It was used to measure the luminosity until SICAL was installed.
- The Silicon luminosity CALorimeter (SICAL) was installed in September 1992 on each side of the interaction region. It uses 12 silicon/tungsten layers to sample the showers produced by small angle Bhabhas. It improves the statistical precision of the luminosity measurement by sampling at smaller angles than LCAL. The systematic error is also reduced thanks mainly to the greater internal precision of the positioning of its components.
- The very small Bhabha CALorimeter (BCAL) located behind the final focus quadrupoles, is used to monitorize the instantaneous luminosity delivered by LEP. Being sited at lower angles, allows to have high statistics and have more frequent measurements at the cost of increased systematic errors. It is a sampling calorimeter made of tungsten converter sheets sandwiched with sampling layers of plastic scintillator. A single plane of vertical silicon strips is used to locate the shower position.

The optimization of the LEP performance needs also some monitoring of the beam conditions which is accomplished by SAMBA in ALEPH:

- The Small Angle Monitor of BACKground (SAMBA) is positioned in front of the LCAL at each end of the detector. It consists of two multi-wire proportional chambers, and it is used as background monitor.

Not all the collisions that take place at LEP are useful to learn on Z^0 physics. Many of these events are interactions with the residual beam-gas or the beam pipe walls, electronic noise, off-momentum particles,... Moreover, some subdetectors

need some time to be ready from event to event. For instance, it takes up to 45 μsec for the ionization electrons to reach the end-plates of the TPC and the electromagnetic calorimeter takes up to 61 μsec to be cleared and ready for the next event. Since up to six bunch crossings occur in this time, this operation should be performed only when it is really necessary. In order to do that a trigger system was designed in a three-level structure. The first two levels are hardware implemented, in order to give a very fast answer, while the third one is implemented by software.

- **Level one** decides whether or not to read out all the detector elements. Its purpose is to operate the TPC at a suitable rate. The decision is taken approximately 5 μsec after the beam crossing from pad and wire information from ECAL and HCAL and hit patterns from the ITC. The level one rate must not exceed a few hundred Hz.
- **Level two** refines the level one charged track triggers using the TPC tracking information. If level one decision cannot be confirmed, the readout process is stopped and cleaned. The decision is taken approximately 50 μsec after the beam crossing (the time at which the TPC tracking information is available). The maximum trigger rate allowed for level two is about 10 Hz.
- **Level three** is performed by software. It has access to the information from all detector components and is used to reject background, mainly from beam-gas interactions and off-momentum beam particles. It ensures a reduction of the trigger rate to 3-4 Hz, which is acceptable for data storage.

All these electronic signals provided by the different subdetector in ALEPH need to be controlled by software. This task is done by the Data Acquisition system (DAQ), which allows each subdetector to take data independently, process all the information taken by the detector, activate the trigger system at every beam crossing and write finally data in a storage system.

The DAQ [37] architecture is highly hierarchical. Following the data and/or control flow from the bunch crossing of the accelerator down to storage device, the components found and their tasks are:

- **Timing, Trigger and Main Trigger Supervisor:** synchronize the readout electronics to the accelerator and inform the ReadOut Controllers (ROC) about the availability of the data.

- ROC: initialize the front-end modules, read them out and format the data.
- Event Builder (EB): build a subevent at the level of each subdetector and provide a “spy event” to a subdetector computer.
- Main Event Builder (MEB): collects the pieces of an event from the various EB and ensures resynchronization and completeness.
- Level three trigger: as already seen, performs a refined data selection.
- Main host and subdetector computers: the main machine (an AXP cluster) initializes the complete system, collects all data for storage and provides the common services. The subdetector computers get the “spy events” and perform the monitoring of the large subdetectors (TPC,ECAL,HCAL).

The data taken by the online computers is called raw data and is reconstructed quasi online. In less than two hours after the data is taken, the event reconstruction and a check of the quality of the data are done, thus allowing ALEPH to have a fast cross-check of the data and correct possible detector problems. This task has been performed by FALCON (Facility for ALepH COmputing and Networking) [38], nowadays integrated in the DAQ system.

The year by year continuous increase of CPU power of the machines has made the hardware and software of FALCON develop in order to accommodate to the available performance and requirements. In its current configuration, FALCON consists of three processors (three DEC-AXP machines). Each of the processors runs the full ALEPH reconstruction program JULIA (Job to Understand Lep Interactions in Aleph) [39] which, for each event of the raw data file, processes all the information from the different subdetectors. There are other programs like PASS0, which compute the drift velocity of the TPC, or the RunQuality program that also run in FALCON.

After their reconstruction, the events are written in files of a format named POT (Production Output Tape), and are transmitted to the CERN computer center where they are converted into different data types more suitable for physics analysis. In this work the ALPHA (ALepH PHysics Analysis) [40] package has been used, as an interface that allows an easy access to the reconstructed physical quantities of the particles: momenta, energies...

3.2.2 Subdetectors relevant to the analysis

The analysis of radiative muon pair events relies essentially on the excellent ALEPH tracking system, that allows the kinematic reconstruction of the events. This is the reason why in the next sections we devote some more time to the actual performance of the tracking devices: VDET, ITC and TPC. The analysis depends also on the ability to identify photons in the ECAL calorimeter, and on the ability to identify muons in the HCAL and μ -chambers. So a few more words are necessary for these subdetectors.

The Vertex Detector

The VDET [41] was the first double sided silicon microstrip detector installed in a colliding beam experiment. The two concentric layers of silicon microstrips wafers are located at radii of 6.5 cm and 11.3 cm. Particles passing through a wafer deposit ionization energy, which is collected on each side of the wafer. On one side, the wafer is read out in the z direction, while in the other, it is read out in the orthogonal $r\phi$ direction. Hits on the two sides are not associated by hardware, but they are added to tracks during the reconstruction process.

The advantage of the VDET is that it pinpoints a track's location in space quite near to the beam pipe. VDET hits are used by extrapolating a track found by the ITC and/or TPC to the VDET and then refitting the track more precisely using VDET hits which are consistent with it. The addition of VDET to the tracking system improved the momentum resolution to $\Delta p_T/p_T^2 = 0.6 \times 10^{-3} (\text{GeV}/c)^{-1}$ for muon pairs at 45 GeV.

Using VDET, together with the other tracking detectors, the spatial coordinates of the origin of a charged track's helix can be found to within 23 μm in the $r\phi$ view and 28 μm in the rz view measured from dimuon events. This allows tracks produced by decay of short-lived particles to be separated from those at the primary interaction point with good efficiency.

The Inner Tracking Chamber

The ITC [42] using axial wires provides up to eight $r\phi$ coordinates for tracking in the radial region between 16 and 26 cm. It also provides the only tracking information

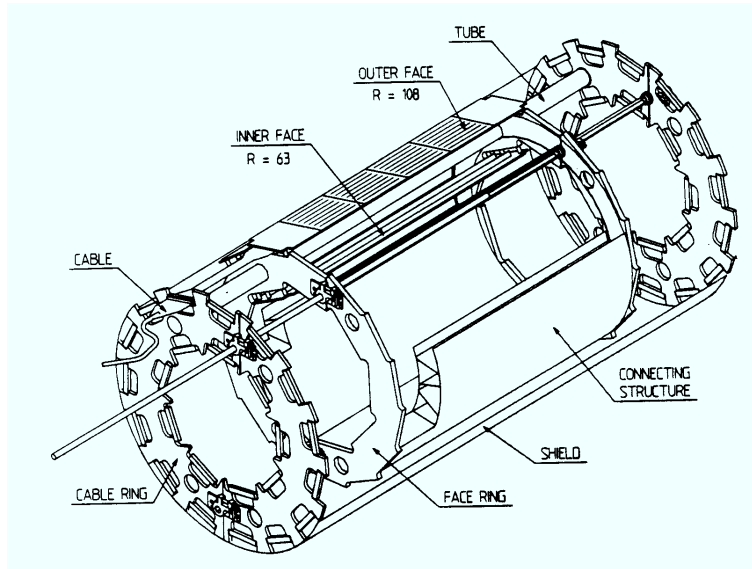


Figure 3.5: Cut-away view of the VDET.

for the level-one trigger system. It is able to identify roughly the number and geometry of tracks, due to its fast response in time (the trigger is available within 2-3 μs of a beam crossing) and allows non-interesting events to be quickly rejected.

The ITC is operated with a gas mixture of argon (50%) and ethane (50%) at atmospheric pressure.

The ITC is composed of 8 layers of sensing wires (operated at a positive potential in the range 1.8-2.5 kV) running parallel to the beam direction, which detect the ionization of particles passing close by. By measuring the drift time, the $r\phi$ coordinate can be measured with a precision of about 150 μm . The z coordinate is found by measuring the difference in arrival time of pulses at the two ends of each sense wire, but with a very poor accuracy of only about 3 cm and it is not used in the standard tracking.

The drift cells of the ITC are hexagonal, with a central sense wire surrounded by six field wires held at earth potential. Four of these field wires are shared by neighboring cells in the same layer (see figure 3.6). The cells in contiguous layers are offset by half a cell width, which helps to resolve the left-right ambiguity in the track fitting.

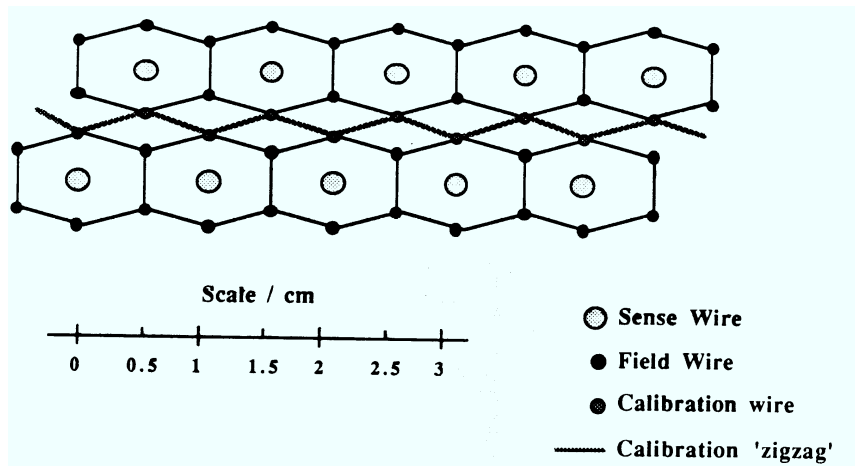


Figure 3.6: The ITC drift cells.

The Time Projection Chamber

The TPC [43] is the main tracking detector in ALEPH. It was designed to obtain high precision measurements of the track coordinates, to get good momentum resolution and to measure the dE/dx depositions of charged particles.

The charged particles that pass through the TPC ionize the gas that fills it. The electrons produced in this ionization are driven by an electric field to the end-plates where wire chambers are located. These are detected and yields the impact point ($r\phi$ coordinate). The time needed for the electrons to reach the end-plates gives the z -coordinate. Due to the presence of a 1.5 T magnetic field parallel to the beam line, the trajectory of a charged particle inside the TPC is a helix and its projection onto the end-plate is an arc of a circle. The measurement of the sagitta of this arc yields the inverse of the curvature radius which is proportional to the modulus of the component of the momentum perpendicular to the magnetic field.

As shown in figure 3.7, it has a cylindrical structure 4.4 m long. Its volume is delimited by two coaxial cylinders which hold the end-plates. The inner cylinder has a radius of 35 cm, the outer one of 180 cm. It was designed with this dimensions in order to reach a 10% resolution in transverse momentum in the worse case (maximum energy of a single particle at 90 GeV in the LEP-II phase).

The device is divided into two half-detectors by a membrane which is situated

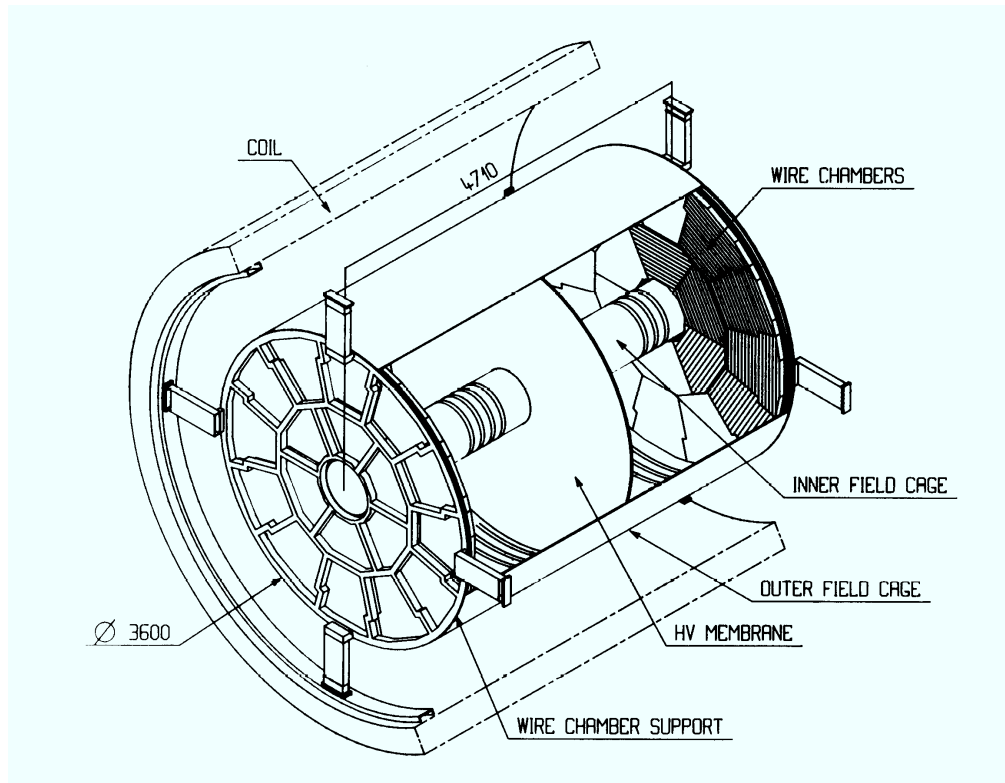


Figure 3.7: View of the TPC.

in the plane perpendicular to the axis and midway between the end-plates. This central membrane is held at a negative high voltage (-26 kV) and the end-plates are at a potential near ground. The curved cylindrical surfaces are covered with electrodes held at potentials such that the electric field (110 V/cm) in the chamber volume is uniform and parallel to the cylinder axis.

The TPC volume is filled with a nonflammable gas mixture of argon (91%) and methane (9%) at atmospheric pressure. This mixture allows to reach high $w\tau$ values (w is the cyclotron frequency and τ is the mean collision time of the drifting electrons). This causes the electrons to drift mainly along the magnetic field lines and thereby reduce the systematic displacements due to the electric field inhomogeneities.

The electrons produced by the ionization are amplified in the proportional wire

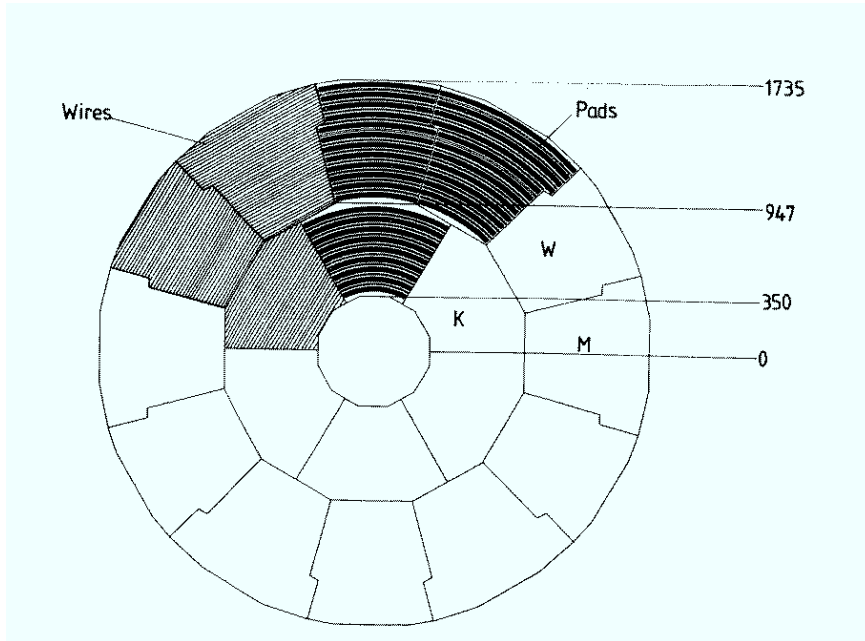


Figure 3.8: View of a TPC end-plate.

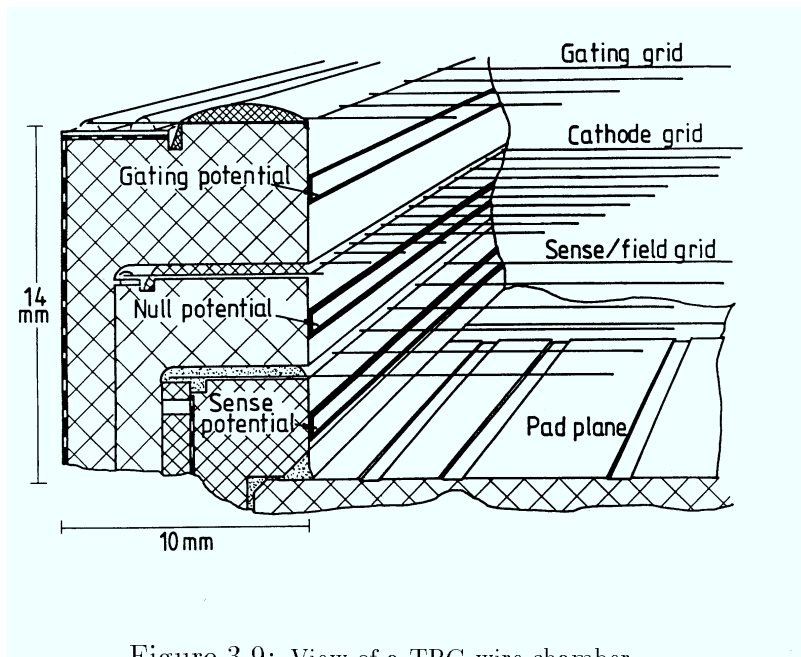


Figure 3.9: View of a TPC wire chamber.

chambers placed in the end-plates. There are 18 wire chambers (“sectors”) on each end-plate. In order to get a minimum loss of tracks at boundaries, the sectors are arranged in a “zig-zag” geometry shown in figure 3.8. In each end-plate, there are six sectors labelled “K” inside a ring of twelve alternating sectors labelled “M” and “W” outside. All sectors are composed of wire chambers and cathode pads. The wire chambers consist of three layers of wires: gating wires, cathode wires and sense/field wires. Figure 3.9 shows a perspective of them.

The gating grid [44] has the purpose of preventing positive ions produced in the avalanches near the sense wires from entering the main volume of the TPC, and thereby distorting the electric field. Potentials of $V_g \pm \Delta V_g$ (with $V_g \sim -67$ V) are placed on alternating wires of the grid. A $\Delta V_g \sim 40$ V is sufficient to block the passage of the positive ions while a much bigger $\Delta V_g \sim 150$ V is required to block also the incoming electrons. In the open state, the grid is transparent to the drifting charged particles. When closed, positive ions are kept off of the drift volume. The gate is opened $3 \mu\text{s}$ before every beam crossing. If a positive trigger signal arrives, the gate is kept open for the maximum $45 \mu\text{s}$ drift time of the electrons in the TPC, otherwise the gate is closed.

The cathode wires keep the end-plates at null potential and, together with the central membrane, create the electric drift field.

The sense wires are kept at a positive potential to provide avalanche multiplication. They are read out to give the energy deposition (dE/dx) for particle identification and the z measurements of the tracks. For the estimation of the dE/dx a truncated mean algorithm is used, taking the mean of the 60% smaller pulses associated with a track. The estimator will be normally distributed and will be sensitive to the particle velocity. The achieved resolution is 4.6% for electrons in hadronic events (slightly better for low multiplicity events). The field wires are kept at null potential to create equipotential surfaces around the sense wires.

The ionization avalanches created around the sense wires are read out by the signal induced on cathode pads at a distance of 4 mm from the sense wires.

The Electromagnetic Calorimeter

The ECAL [45] is located around the TPC and inside the coil. It is divided into a central barrel region closed at both ends with end-caps, as shown in figure 3.11.

Both barrel and end-caps are divided into modules of 30° in azimuthal angle ϕ with the end-cap modules rotated 15° with respect to the barrel modules. The entire calorimeter is rotated a little bit with respect to the HCAL in order to avoid the overlap of crack regions. The barrel is a 4.8 m long cylinder with an inner radius of 1.85 m and an outer radius of 2.25 m. Each module consists of 45 layers of lead and wire chambers. The wire chambers are made of open-sided aluminium extrusions and filled with a gas mixture of xenon (80%) and carbon dioxide (20%). Ionization from an electromagnetic shower developed in the lead sheets is amplified in avalanches around $25 \mu\text{m}$ diameter gold-plated tungsten wires. The signals are read out via the extrusions open faces with cathode pads covered by a graphited mylar sheet. The structure of a typical single layer of the calorimeter is shown in figure 3.10.

The cathode pads are connected internally to form “towers” which point to the interaction point. Each tower is read out in three sections in depth (“storeys”). The size of the pads is approximately $30 \times 30 \text{ mm}^2$ leading to a high granularity very useful to identify photons.

The achieved energy resolution for electrons and photons is

$$\frac{\sigma_E}{E} = \frac{0.18}{\sqrt{E/\text{GeV}}} + 0.009$$

The Hadronic Calorimeter and μ -chambers

Surrounding the superconducting coil one finds the main mechanical support of the ALEPH detector: a large iron structure which returns the magnetic flux of the magnet and constitutes the passive material of the HCAL [46].

The Hadronic calorimeter is a sampling calorimeter made by iron layers and streamer tubes, which are the active elements of the calorimeter. The mechanical structure is very similar to the ECAL one, with a 6.3 m long barrel that extends from an inner radius of 3 m to an outer radius of 4.68 m (see figure 3.11). It is segmented in 12 modules, each one with 22 layers of 5 cm iron sheets and 23 streamer tubes filled with a mixture of argon (21%), carbon dioxide (42%) and isobutane (37%). The radial length of the barrel corresponds to about 7.2 interaction lengths, which is enough to contain the hadronic showers at LEP energies.

Three different kind of signals are read out in the hadronic calorimeter: signals from the pads situated outside the modules containing the streamer tubes, which are used to measure the energy of the showers; signals from the strips situated along the streamer tubes modules, which give the pattern of the streamer tubes in the event and are used as a “tracking” of the showers and to identify muons (see section 3.3.2); and the signal from the wires, which measures the energy released in the planes and is used mainly for triggering.

The energy resolution for pions at normal incidence is given by

$$\frac{\sigma_E}{E} = \frac{0.85}{\sqrt{E/\text{GeV}}} + 0.009$$

The digital information on individual strips in the HCAL is already an essential part of the muon detector. In addition, surrounding the HCAL calorimeter, (both in the barrel and in the end-caps), two double layers of streamer tubes filled with a mixture of argon (13%), carbon dioxide (57%) and isobutane (30%) (called, in the following μ -chambers) were installed to identify tracks crossing the full iron and to

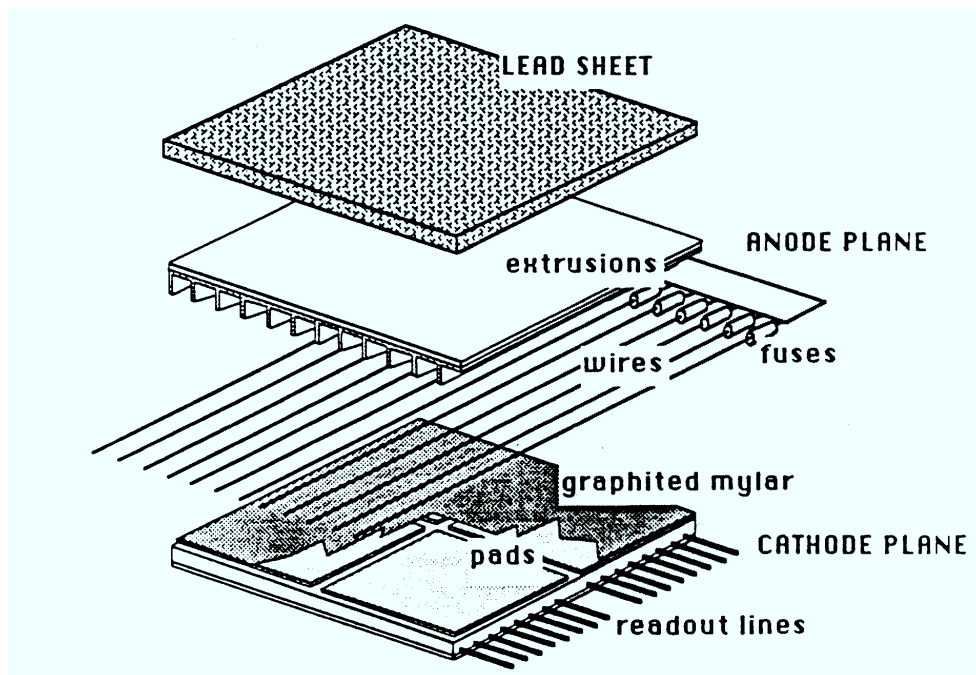


Figure 3.10: View of an ECAL stack layer.

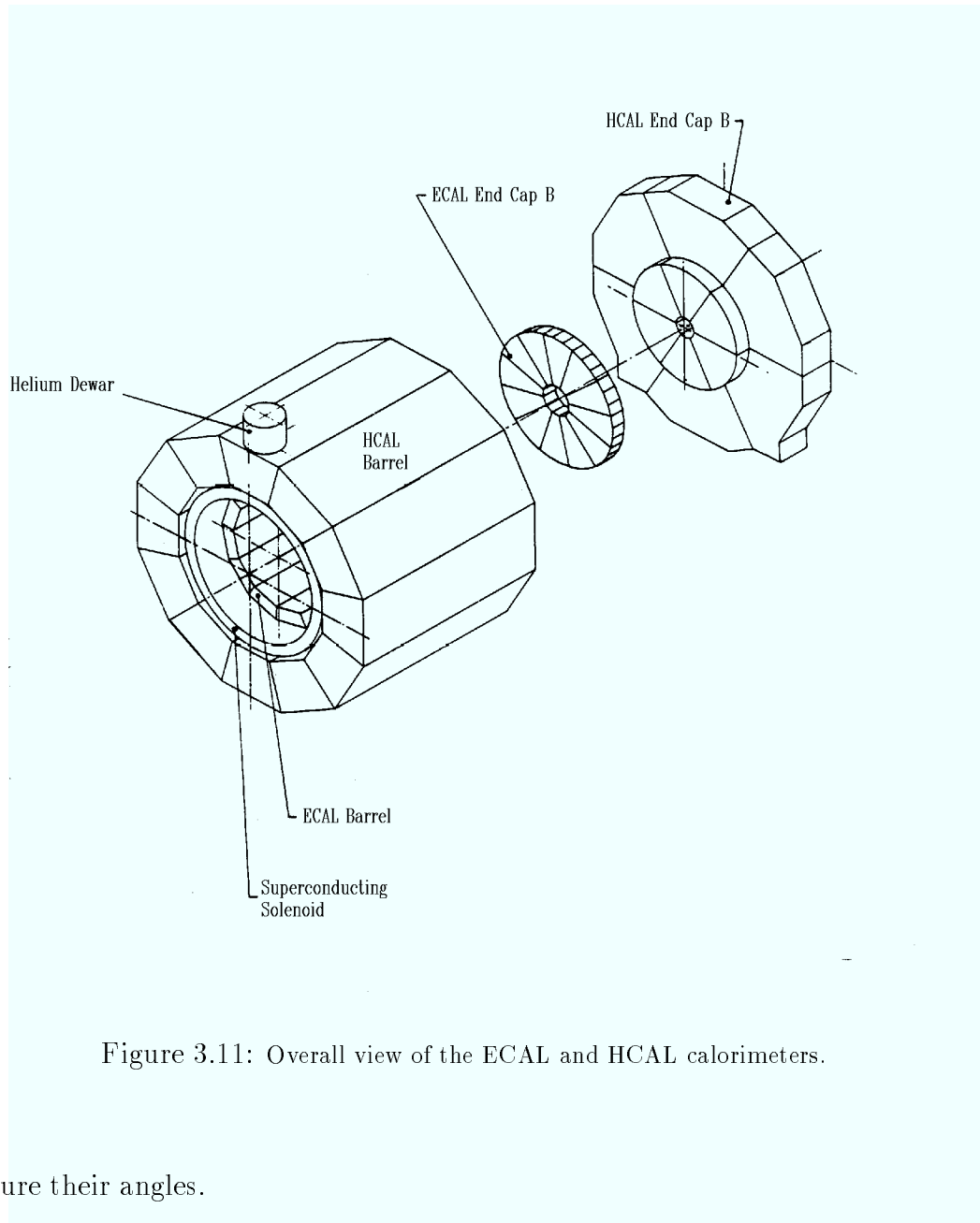


Figure 3.11: Overall view of the ECAL and HCAL calorimeters.

measure their angles.

Since the layers backing the barrel and the end-caps reproduce the structure of the hadron calorimeter, additional streamer tubes (called middle-angle chambers) are needed to cover the gaps left open in the boundary region. Each layer of tubes has, on one side, strips that are parallel to the wires (x -strips), 4 mm wide with a 10 mm pitch; on the other side there are strips which, being orthogonal to the wires (y -strips), are 10 mm wide with a 12 mm pitch to get an appreciable induced signal. As the muon chambers constitute a tracking device, no pads are provided.

3.3 Event reconstruction and simulation

In this section we briefly describe the performance of the ALEPH detector reconstructing the relevant physical parameters in this analysis: track reconstruction, muon and photon identification. A description of the event simulation process and its limitations is also given.

3.3.1 Tracking in ALEPH

Tracks are reconstructed starting in the TPC. Nearby hits are linked to form track segments, and the segments are connected to make tracks by requiring consistency with a helix hypothesis. These tracks candidates are extrapolated to the inner detectors where consistent hits are assigned. Coordinate errors are determined using the preliminary track parameters. The final track fit based on Kalman filter [47] techniques uses these errors and takes into account multiple scattering between each measurement.

The track finding efficiency in the TPC has been studied using Monte Carlo simulation. In hadronic Z events, 98.6% of tracks that cross at least four pad rows in the TPC are reconstructed successfully; the small inefficiency, due to track overlaps and cracks, is reproduced to better than 0.1% by the simulation. The efficiency of associating a vertex detector hit to an isolated track is about 94% per layer, within the geometrical acceptance.

The performance of the track reconstruction is studied using dimuon events. Figure 3.12 shows the ratio of the beam energy to the measured momentum. Here a track is required to have at least 19 TPC hits, at least six ITC hits and at least one VDET hit in the $r\phi$ plane. The acollinearity angle between the positive and the negative muon is required to be smaller than 0.2° in order to eliminate radiative events. These events are also removed by requiring the sum of the energies of all clusters in the electromagnetic calorimeter which are not associated with the two muons to be less than 100 MeV. In this way, one obtains the already mentioned several times transverse momentum resolution of

$$\sigma(1/p_T) = 0.6 \times 10^{-3} (\text{GeV}/c)^{-1} \quad (3.1)$$

for 45 GeV muons in the angular acceptance $|\cos\theta| < 0.8$. Table 3.1 summarizes the measured resolution for TPC only, for TPC and drift chamber, and for all three

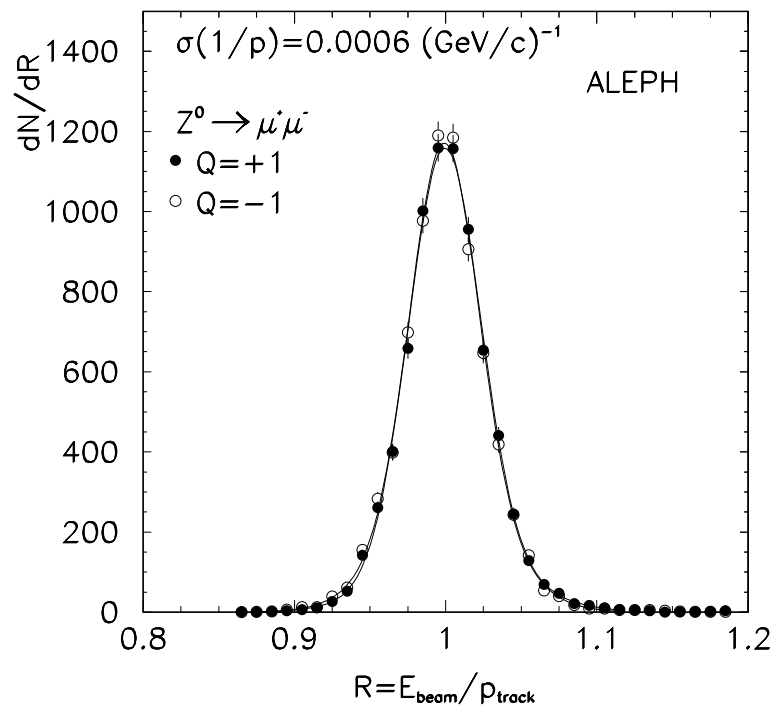


Figure 3.12: The ratio of the beam energy to the track momentum in the tracking system for muons.

detectors together. At low momentum multiple scattering dominates and adds a constant term of 0.005 to $\sigma(p_T)/p_T$.

Detector	$\sigma(1/p_T)$ (GeV/c) ⁻¹
TPC	1.2×10^{-3}
+ ITC	0.8×10^{-3}
+ VDET	0.6×10^{-3}

Table 3.1: Momentum resolution of the tracking system. The successive rows show the effect of including the detectors indicated in the fit.

The angular resolution of the tracking is really good. For instance the resolution achieved in the measurement of the polar angle ($\cos \theta$) of dimuon events is better than 0.3×10^{-3} with a negligible impact on the analysis presented here.

3.3.2 Particle identification: μ and γ

Muon identification

Muons are identified by making use of the tracking capabilities of the HCAL, together with the muon chambers information. Muon identification in the calorimeter uses the digital readout (described in section 3.2.2) to check whether particles penetrate through the whole depth of the calorimeter.

Tracks are extrapolated (as if they were a muon) through the calorimeter material taking into account a detailed magnetic field map and estimated energy losses. A “road” is opened around the extrapolated track, with a width of three times the estimated extrapolation uncertainty due to multiple scattering. A calorimeter plane is said to be expected to fire (N_{expected}) if the extrapolated track intersects it within an active region, and the plane is said to have fired (N_{fired}) if a digital hit lies within the multiple scattering road. For a hit to be counted, the number of adjacent firing tubes must not be greater than three.

A track is defined to have hit the muon chambers if at least one of the two double-layers yields a space point whose distance from the extrapolated track is less than four times the estimated standard deviation from multiple scattering.

The identification is performed by selecting tracks that penetrate through the whole depth of the hadron calorimeter without showering. The identification efficiency does not vary significantly with momentum. The cuts used to define a penetrating track are:

$$\left(\frac{N_{\text{fired}}}{N_{\text{expected}}} \right)_{\text{allplanes}} > 0.5 \quad (3.2)$$

$$\left(\frac{N_{\text{fired}}}{N_{\text{expected}}} \right)_{\text{last10planes}} > 0.3 \quad (3.3)$$

in this way, a track is identified as a muon if it satisfies equations 3.2 and 3.3, or if it has at least one hit in the muon chambers. Monte Carlo simulation predicts a muon identification inefficiency below 0.05% inside the angular acceptance $|\cos\theta| < 0.9$.

Photon identification

The three-dimensional segmentation of the electromagnetic calorimeter allows a good spatial resolution to be achieved for photons up to the highest energies available at LEP. The algorithm to identify photons in ALEPH, (GAMPECK [48]), uses the facts that electromagnetic showers generally start in the first segment in depth of the electromagnetic calorimeter and that storeys receiving energy from a photon have a compact arrangement and most of them share a face with another storey associated to the same photon.

The storeys of the first segment in depth of the electromagnetic calorimeter are scanned in the order of decreasing energy. A storey without a more energetic neighbour defines a new cluster. Other storeys are assigned to the cluster of their highest energy neighbour. To take advantage of the compact nature of electromagnetic showers and of the projective geometry of the calorimeter two storeys are considered neighbours only when they share a common face. The same procedure is then applied to the storeys of the second and third segments in depth but then, when processing a storey, the algorithm looks first for a neighbour in the previous segment. The clusters found by the algorithm are retained as candidate photons if their energy is greater than 0.25 GeV and if there is no charged track impact at a distance of less than 2 cm from the cluster barycenter.

The position of a photon impact point is computed in two steps. A first approximation is given by the cluster barycenter i.e. the energy-weighted mean of the coordinates of each storey centre. This position is corrected for the finite size of the calorimeter cells using a parameterization of the typical S-shape curve that always appears when the calorimeter granularity is comparable to the electromagnetic shower size.

In order to reduce the sensitivity of the energy measurement to hadronic background and clustering effects, the photon energy is computed from the energy collected in the four central towers of the cluster, and the expected value of the fraction of energy in the four towers, F_4 . This fraction is computed from a parameterization of the shower shape for a single photon in the calorimeter. The computation takes into account the calorimeter pad area and the distance between the photon impact and the nearest tower corner, as well as the variation with energy of the expected F_4 . Corrections to the energy are computed for energy losses before and after the

calorimeter and energy loss in the overlap.

The angular resolution for an isolated cluster is

$$\sigma_{\theta,\phi} = \left(\frac{2.5}{\sqrt{E/\text{GeV}}} + 0.25 \right) \text{ mrad.}$$

The use of only a part of the storeys to measure the energy degrades the energy resolution to

$$\frac{\sigma_E}{E} = \frac{0.25}{\sqrt{E/\text{GeV}}}$$

from the previous quoted $\frac{\sigma_E}{E} = \frac{0.18}{\sqrt{E/\text{GeV}}}$.

3.3.3 Monte Carlo simulation

The selection procedure and the resolution of the ALEPH subdetectors modify the expected distributions. In order to evaluate these effects and the possible background contamination Monte Carlo simulated events are used. The chain to produce such kind of events is as follows:

- *Generation of the event kinematics.* The particle four-momenta are generated according to the different physics process that could produce similar final states in the detector, (in parenthesis the names of the computer program used):
 - $e^+e^- \rightarrow \mu^+\mu^-$ (KORALZ 4.0 [49])
 - $e^+e^- \rightarrow \tau^+\tau^-$ (KORALZ 4.0)
 - $e^+e^- \rightarrow e^+e^-$ (BABAMC [50])
 - $e^+e^- \rightarrow e^+e^-\mu^+\mu^-$ (PHOPHO [51])

In ALEPH, all these programs have been unified through the common interface KINGAL [52].

- *Simulation of the detector response.* This is done using a GEANT [53] based program (GALEPH [54]) where all the information about the geometry and materials involved in the experimental setup are simulated. For the tracking

simulation, the primary long-lived particles are followed through the detector. Secondary particles are also produced by interaction with the detector material. Bremsstrahlung, Compton scattering and ionization are some of the processes simulated. GEANT and GHEISHA [55] are used to simulate the electromagnetic and nuclear interactions respectively. The energy depositions are converted to measurable electrical signals.

- *Reconstruction.* The same reconstruction program (JULIA) used for the real data is used in the simulated events. Thus, the output of all the simulation process has the same format as the real data.

Physics limitations of the simulation

KORALZ 4.0 is a Monte Carlo generator that treats the generation of hard photons in the initial state to $\mathcal{O}(\alpha^2)$, and the radiation of soft ISR photons is considered to all orders in perturbation theory by exponentiation. The program has also the possibility to exponentiate FSR, and in an approximate way it can generate up to two hard photons in the final state. Moreover, non-photonic radiative corrections are taken into account at the one loop level, with resummation of leading top dependences.

The main physics limitation is that QED initial-final state bremsstrahlung interference in the presence of multiple QED hard bremsstrahlung is not included. In other words, as long as there is no strong cut on the radiated energy (see figure 2.8) the simulation is good enough.

Chapter 4

Data analysis

In chapter 2 we have seen how the current measurements taken at the nominal LEP centre-of-mass energy, are a centre-of-mass average of the “hard scattering” process, because the ISR energy losses are effectively “scanning” the effective centre-of-mass energy ($\sqrt{s'}$). We have seen that we can define s' theoretically being the square of the four-momentum of the intermediate boson as long as the effect of the I-F QED interference can be neglected, (whis is the case if $x > \frac{\Gamma_Z}{M_Z} \sim 0.03$).

In this chapter we consider the problem of determining the effective energy ($\sqrt{s'}$) experimentally. The approximations used and a Monte Carlo study of the performance of the method are discussed in section 4.1. Section 4.2 is devoted to explain the selection procedure necessary to separate the process we want to study $e^+e^- \rightarrow \mu^+\mu^-(n\gamma)$ from potential sources of background. This procedure inevitably distorts the probability density $\frac{d^2\hat{\sigma}}{dx d\cos\theta}(s)$ introduced in equation 2.17. Section 4.3 deals with the corrections, to remove this distortions while in the last section we built the final loglikelihood function as a function of the electroweak parameters.

4.1 Determination of the effective centre-of-mass energy

The first idea that one could think of would be to compute the effective centre-of-mass energy from the invariant mass of the detected particles in the final state ($\mu^+\mu^-(\gamma)$). This is the simplest approach experimentally, but the resolution is not so good. For instance, if we only consider the invariant mass of the muon system

(i.e. neglecting FSR), and we neglect the experimental error in the determination of the polar angles, the total energy resolution is completely determined by the resolution on the transverse component of the momentum. In this case, if we quote the total energy E_μ in GeV, we have:

$$\begin{aligned} s' &= 2E_{\mu^+} E_{\mu^-} (1 - \cos \theta_{\mu^+ \mu^-}) \\ \frac{\Delta s'}{s'} &= 0.6 \times 10^{-3} (\text{GeV})^{-1} \sqrt{E_{\mu^+}^2 \sin^2 \theta_{\mu^+} + E_{\mu^-}^2 \sin^2 \theta_{\mu^-}} \end{aligned}$$

which is a good approximation of the ALEPH tracking system resolution in the angular acceptance $|\cos \theta| < 0.8$, as we have shown in section 3.3.1. This gives a precision of approximately $\frac{\Delta s'}{s'} \sim \Delta x \sim 0.03 - 0.04$, which is of the same order as the ‘‘optimal’’ size of the binning needed to be as insensitive as possible to I-F QED interference effects. Moreover, if we don’t neglect FSR, the resolution will be much worse because we need to introduce the resolution of the Electromagnetic calorimeter (ECAL).

On the other hand, if we consider that the predominant effect of the initial-state photon radiation is to boost the centre-of-mass system, (i.e. the photons are emitted along the direction of the beams), we can compute the radiated energy, E_γ^{ISR} , from the measured directions of the final state particles, which are determined with very good precision as has been described in section 3.3.1. In this approximation, all photons detected in ECAL are presumed to be radiated in the Final State.

The radiated energy can be calculated in terms of the boost, $\beta = \frac{V}{c}$, that relates the *LAB* system and the *CM* system through:

$$E_\gamma^{ISR} = \frac{|\beta|}{1 + |\beta|} \sqrt{s} \quad (4.1)$$

where \sqrt{s} is the nominal centre-of-mass energy. Moreover, if we neglect the possibility to radiate two or more photons in opposite directions, we find:

$$\begin{aligned} s' &= s \left(1 - \frac{2E_\gamma^{ISR}}{\sqrt{s}} \right) \\ x &= \frac{2|\beta|}{1 + |\beta|} \end{aligned} \quad (4.2)$$

so that the desired variable x is related in a simple manner with the boost of the *LAB* system. The explicit demonstration of these formulae can be found in appendix B.

In the case where there is no signal in ECAL, we can assume that there is no relevant Final State Radiation, and we can impose the condition that the two muon candidates have to be back-to-back in the CM system. If we call θ_{12} the relative angle between both muons measured in the LAB system, and θ'_{12} the relative angle in the CM system, we can derive from the Lorentz invariance of the scalar product the relation:

$$\begin{aligned} (P'_i \cdot P'_j) &= (P_i \cdot P_j) \\ \cos \theta'_{ij} &= 1 - \frac{(1 - \beta^2)(1 - \cos \theta_{ij})}{(1 + \beta \cos \theta_i)(1 + \beta \cos \theta_j)} \end{aligned} \quad (4.3)$$

With the constraint $\theta'_{12} = \pi$, this equation can be solved analytically and gives as a result:

$$|\beta| = \frac{|\sin(\theta_1 + \theta_2)|}{\sin \theta_1 + \sin \theta_2} \quad (4.4)$$

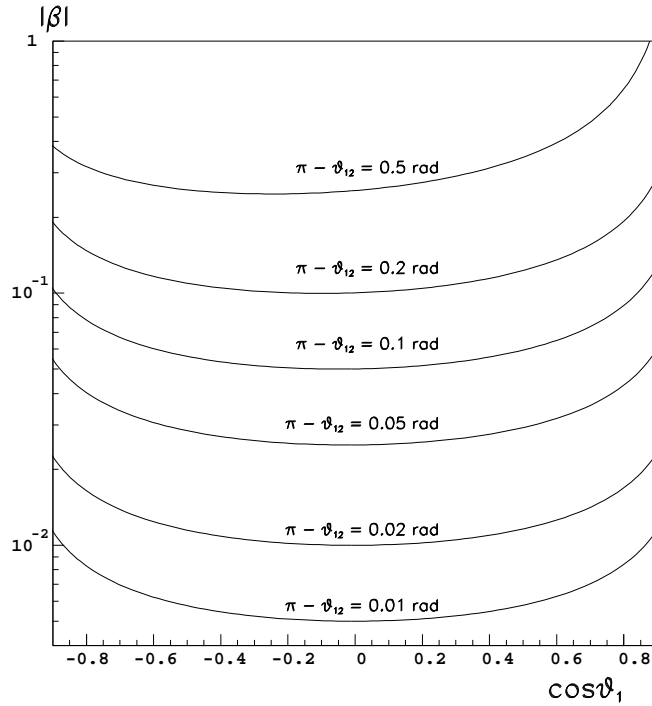


Figure 4.1: $|\beta|$ as a function of the acollinearity (η) defined as $\eta = \pi - \theta_{12}$ and $\cos \theta_1$, in the absence of Final State Radiation.

This is shown in figure 4.1, where one can see how the magnitude of the boost (or the radiated energy) depends not only on the acollinearity of the two particles, but it also depends on their angular distribution.

In the most general case, there will be FSR. If we consider also the possibility to have one radiated photon in the final state, the three particles ($\mu^+ \mu^- \gamma_{FSR}$) will be contained in a plane in the CM system. So, from the relative angles measured in the LAB system (see fig. 4.2), θ_{ij} , and the event orientation, θ_i , we compute β such that the angles in the CM system, θ'_{ij} satisfy the condition:

$$\theta'_{12} + \theta'_{23} + \theta'_{31} = 2\pi \quad (4.5)$$

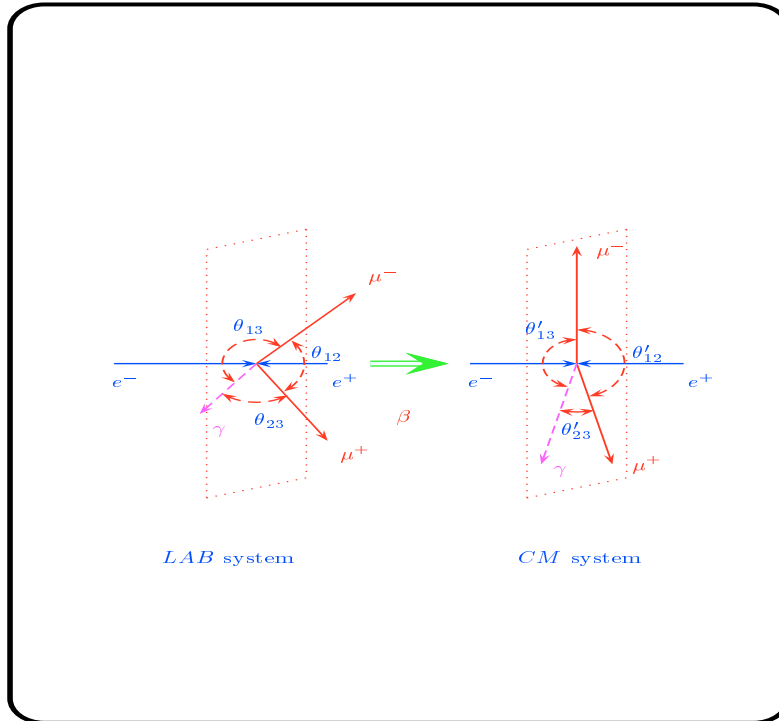


Figure 4.2: Definition of the angles used to compute β . The measured angles in the LAB system (θ_{ij}), are used to determine the magnitude of the boost along the beam direction, that satisfies that the transformed angles (θ'_{ij}) are contained in a plane.

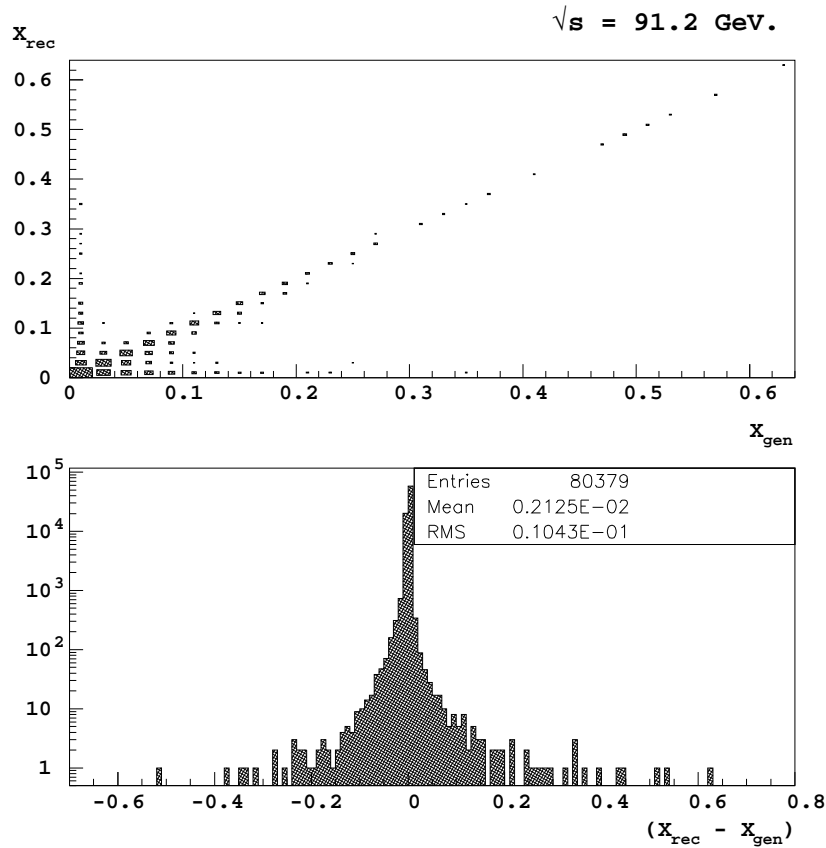


Figure 4.3: MonteCarlo study of the performance of the $s' \equiv s(1-x)$ reconstruction at $\sqrt{s} \sim 91.2 \text{ GeV}$. The size of the squares is proportional to the logarithm of the number of events.

Note that β is found from the measured directions of the particles, and we are not limited by the energy resolution in ECAL, or by the momentum resolution of the ALEPH tracking system. Actually, the resolution on x is very good and, as can be observed in fig. 4.3, the RMS of the differences between the reconstructed (x_{rec}) and the generated (x_{gen}) radiated energy is around $\Delta x \sim 0.01$ (to be compared with a binning size of $\Delta x \sim 0.04$). The selection procedure that has been applied to determine x_{rec} is explained in the next section.

One can see in this figure two bands at $x_{rec} = 0$ and at $x_{gen} = 0$. The horizontal band ($x_{rec} = 0$) is mainly due to the approximations used to define x experimentally, i.e. only one hard collinear photon in the initial state. The vertical band ($x_{gen} = 0$) is mainly due to events that have radiated in the final state, but the photon has

not been reconstructed properly in ECAL.

For three particles lying in a plane, their energies can be expressed in terms of their total energy and the angles between them (see for instance [56] or appendix B). In particular the energy of the final state photon, $E_\gamma^{FSR'}$, can be calculated in this way from the computed β and the nominal centre-of-mass energy \sqrt{s} , through:

$$E_\gamma^{FSR'} = \sqrt{s'} \frac{\sin \theta'_{12}}{\sin \theta'_{12} + \sin \theta'_{23} + \sin \theta'_{31}} \quad (4.6)$$

where, as usual, the primed quantities refer to the CM system, while E_γ^{FSR} is computed from equation 4.6 and the Lorentz equations that relates both reference systems. This usually results in a smaller uncertainty than the expected $25\% \sqrt{E}$ which is obtained from the ECAL energy resolution, and therefore can be used to cross-check the consistency of the calculation on an event-by-event basis.

4.2 Event selection

In order to study the effect of the experimental cuts, we have generated and reconstructed around 10^6 MC events at different energies with KORALZ 4.0 (KORL07). This Monte Carlo program [49] treats the generation of hard photons in the initial state to $\mathcal{O}(\alpha^2)$, and the radiation of soft ISR photons is considered in all orders by exponentiation. The program also has the possibility to exponentiate Final State Radiation, and in an approximate way generates up to two hard photons (parameter KEYRAD set to 12). However, we have generated FSR computing only to $\mathcal{O}(\alpha)$, (parameter KEYRAD set to 112), and therefore allowing only the possibility to have up to one photon coming from FSR. This is a technical detail that simplifies the computation of x_{gen} , and allows the comparison with most of the official ALEPH MC that was generated using this conditions. In any case, the formalism developed in the previous section is only valid when we assume that the maximum number of photons in the Final State is one, and therefore the possibility to have more than one hard photon in the Final State will be suppressed in the data with appropriate cuts. Moreover, even from a pure theoretical point of view, there are good reasons to eliminate such events, because when there are two hard photons in the FS and there is one hard photon in the IS, one needs to know the theory at least to $\mathcal{O}(\alpha^3)$.

The effect of I-F QED interference is neglected in KORALZ when one considers corrections higher than $\mathcal{O}(\alpha)$, allowing the straightforward definition of $x_{gen} = 1 - s'_{gen}/s$, where s'_{gen} is the generated invariant mass of the $\mu^+\mu^-(\gamma_{FS})$ system.

An appropriate value for the limit between the soft and hard photon emission, x_0 , has been carefully chosen. The program only generates the full kinematics of the event for values of $x > x_0$ and we have chosen $x_0 = 0.001$, which is far enough from the experimental resolution in this variable, and not the default value $x_0 = 0.01$.

Table 4.1 shows the total statistics generated for each energy point, and also the official ALEPH MC statistics used to study possible sources of background.

Energy (GeV)	Process	Number of evts.	Generator
91.200 (PEAK) 91.250 (PEAK) 91.270 (PEAK)	$e^+e^- \rightarrow \mu^+\mu^-$	600000	KORL07
90.200 (P-1) 92.000 (P+1)	$e^+e^- \rightarrow \mu^+\mu^-$	100000	KORL07
89.450 (P-2) 93.000 (P+2)	$e^+e^- \rightarrow \mu^+\mu^-$	160000	KORL07
88.450 (P-3) 93.700 (P+3)	$e^+e^- \rightarrow \mu^+\mu^-$	85000	KORL07
130.0 (HE) 136.0 (HE)	$e^+e^- \rightarrow \mu^+\mu^-$	20000	KORL07
91.250 (PEAK)	$e^+e^- \rightarrow \tau^+\tau^-$	100000	KORL06
91.200 (PEAK)	$e^+e^- \rightarrow e^+e^-$	100000	BHAB01
91.250 (PEAK)	$e^+e^- \rightarrow (e^+e^-)\mu^+\mu^-$	20000	PHOT01

Table 4.1: MonteCarlo statistics used for several energies and processes.

In order to separate the signal process from potential sources of background, we have optimized a selection procedure. An event is accepted if the relevant detectors for the analysis were operative (XLUMOK criteria [40]), and it fulfills the following requirements:

- Two charged tracks with at least 4 TPC pad row hits.

- The two charged particles are contained in the angular acceptance of the TPC, ($|\cos \theta_i| < 0.90$).
- Both tracks are originated in a cylinder of radius $D0 = 0.2$ cm and length $|Z0| < 3$ cm around the interaction point.
- The tracks have opposite electric charge, ($q1 + q2 = 0$).
- The sum of the momenta of both charged particles does not exceed 150% of the nominal LEP centre-of-mass energy, ($p1 + p2 < 1.5 \times \sqrt{s}$).
- There is at least 1 ITC hit within both tracks.

Muon candidates are selected using the HCAL digital readout and the muon chambers information, as explained in section 3.3.2. An event is selected if at least one of the two tracks satisfies the requirements to be identified as a muon.

Figure 4.4 shows the Monte Carlo predictions for the distribution of the momentum of the most energetic track, (normalized to the nominal centre-of-mass energy), for events that have been selected. One can see that there is a considerable background from tau and two-photon processes, due to the fact that we have not applied any cut on the momentum or acollinearity of the two tracks selected. Nevertheless, if we require the momentum of the most energetic track ($p1$) to be greater than 35 GeV there is essentially no loss in the signal, while the two-photon background is eliminated. Therefore, we require

- $p1 > 35 \times \frac{\sqrt{s}}{91.2}$,

Moreover, as we have already mentioned, the formalism developed in section 4.1 is only valid when there is only one photon in the Final State. In order to be consistent, we require to have a maximum of one identified photon in ECAL with an energy larger than 0.3 GeV, with the criteria described in section 3.3.2.

Now, we can compute x for each selected event as described in section 4.1. This allows to compute E_γ^{FSR} using the Lorentz transformation of equation 4.6, and compare with the measured energy in the ECAL. In fig. 4.5 one can see how the MC is able to reproduce the measured energy in ECAL, (although it seems not to reproduce so well the possibility to emit high energy photons), and also the performance of the calculation of E_γ^{FSR} compared with the energy reconstructed in

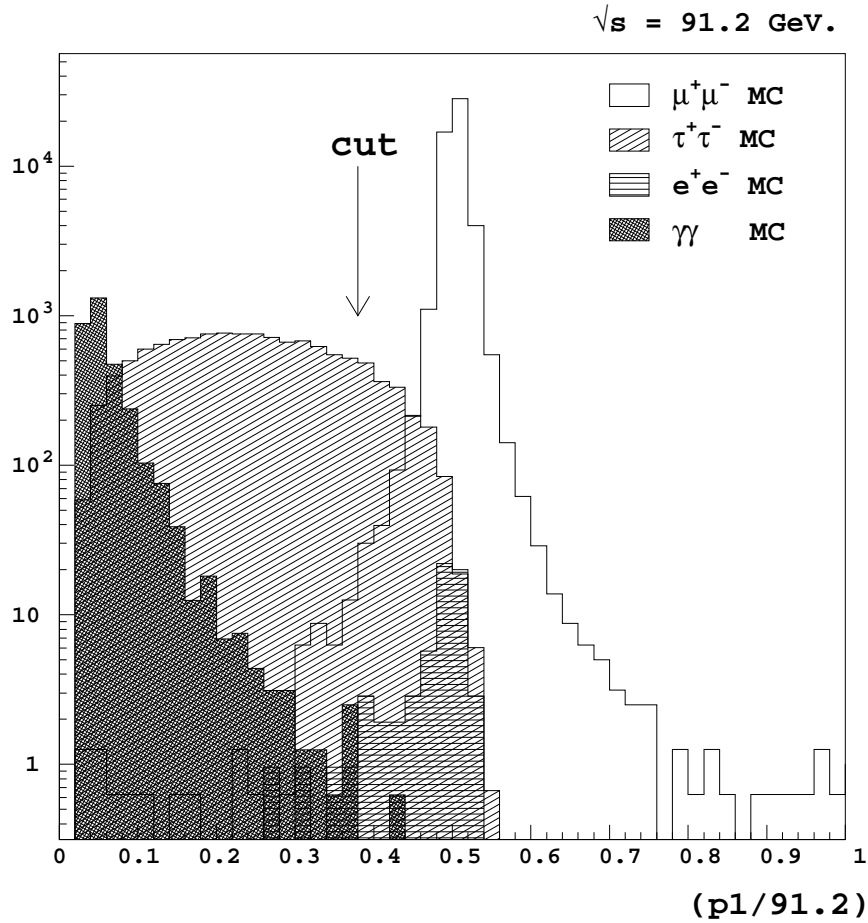


Figure 4.4: Momentum of the most energetic track normalized to the nominal centre-of-mass energy, that have survived the acceptance and digital selection.

ECAL from Monte Carlo simulation. We require these quantities to be consistent at the level of four times the energy resolution in ECAL,

- $(E_{\gamma}^{FSR} - ECAL) < 4\sigma$

In this way, most of the photons detected in ECAL, (and therefore at a polar angle larger than 26°) that were coming from ISR are removed from the data sample.

After the cut on particle momentum is applied, the only non-negligible background is tau events, with at least one of them decaying into a muon. This is a potentially dangerous background, because it can be confused with a radiative

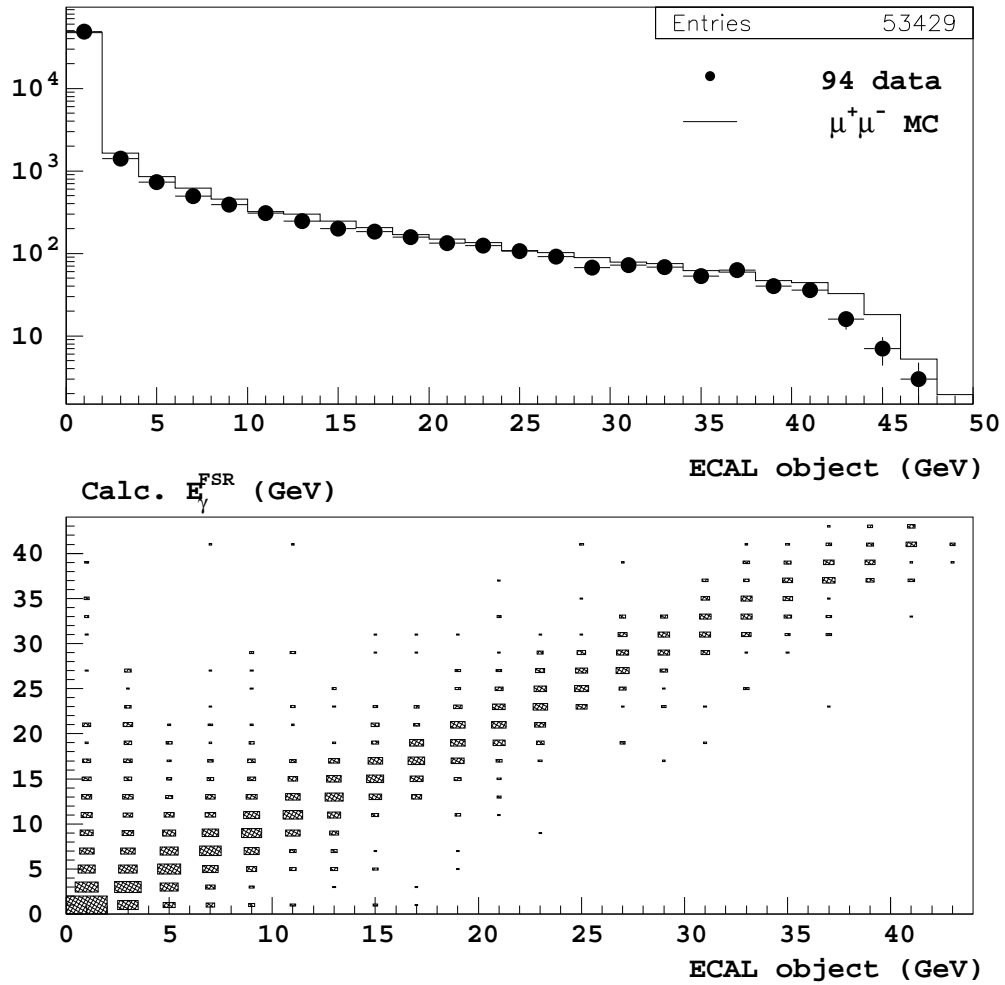


Figure 4.5: The upper figure compares the measured energy in ECAL for the photon candidate with MC simulation. The lower figure compares the computed energy of the FSR photon using the angular information and the actual energy measured in ECAL. The size of the squares is proportional to the logarithm of the number of events.

dimuon event, and can modify drastically the energy dependence we want to determine. However, it can be eliminated taking profit of the missing energy in the tau decay carried by the neutrinos. We require that the total energy left after radiation, $(\sqrt{s} - E_\gamma^{ISR})$, has to be consistent at the level of four times the total energy resolution in the ALEPH detector.

- $(\sqrt{s} - E_{\gamma}^{ISR}) - (p_{\mu^+} + p_{\mu^-} + ECAL) < 4\sigma$

As can be seen in table 4.2, the remaining background after all the cuts have been applied is completely negligible, and dominated by missidentified Bhabhas (0.09%), while the total selection efficiency is 0.80337 ± 0.00051 at the Z peak.

$\sqrt{s} = 91.2$ GeV	$e^+e^- \rightarrow \mu^+\mu^-$	$e^+e^- \rightarrow \tau^+\tau^-$	$e^+e^- \rightarrow e^+e^-$	$e^+e^- \rightarrow (e^+e^-)\mu^+\mu^-$
total	600000	100000	100000	20000
Accept. cuts	495883	42476	47682	5119
p1 cut	495411	5417	45735	1
Dig. Sel. cuts	495374	2366	62	1
$N_{\gamma} < 2$ in ECAL	494373	1707	62	1
$(E_{\gamma}^{FSR} - ECAL)$ cut	489863	1673	57	1
$(\sqrt{s} - E_{\gamma}^{ISR})$ cut	482021	6	33	1
Efficiency (ϵ)	80.337%	0.006%	0.03%	0.005%
Purity	99.89%	0.01%	0.09%	0.01%

Table 4.2: Breakdown of the effect of the selection cuts on the signal and on possible sources of background.

This selection procedure has been applied both to real data and Monte Carlo simulation for the different LEP nominal centre-of-mass energies that appear in table 4.1. The resulting efficiencies obtained from the MC simulation are shown in table 4.3.

The efficiency for the HE run at 130-136 GeV is much lower due to the inclusion of new cuts to deal with the new experimental conditions at these energies [58]. The invariant mass of the muon system is required to be greater than 80 GeV in order to reduce the substantial background from $\gamma\gamma$ processes. Moreover, there is a high “radiative return” to the Z peak that produces an increase on the number of events with ISR photons emitted at large angles and, therefore, visible in the detector. Some of them are not removed by the consistency check between the computed photon energy with Eq. 4.6 and the measured one. Therefore, the invariant mass of the muon system is required to be greater than 110 GeV in events where the reconstructed x_{rec} is below 0.25.

Energy (GeV)	Efficiency
91.2 (PEAK)	$80.337 \pm 0.051\%$
90.2 (P-1)	$80.81 \pm 0.18\%$
92.0 (P+1)	$79.93 \pm 0.18\%$
89.4 (P-2)	$80.59 \pm 0.13\%$
93.0 (P+2)	$79.38 \pm 0.17\%$
88.4 (P-3)	$80.17 \pm 0.18\%$
93.7 (P+3)	$79.04 \pm 0.22\%$
130.0 (HE)	$55.71 \pm 0.53\%$
136.0 (HE)	$54.96 \pm 0.53\%$

Table 4.3: Computed efficiency from Monte Carlo simulation at the different LEP nominal centre-of-mass energies.

4.3 Correction functions ($\epsilon_{F(B)}(s, x)$)

So far we have defined the experimental procedure that allows to obtain for each dimuon event x and $\cos \theta$, with high efficiency and negligible background, where $\cos \theta$ is the scattering angle in the CM system, computed from Equation 2.18.

The probability to obtain a specific value for these two variables, is given by the two-dimensional density function in equation 2.17, ($\frac{d^2\hat{\sigma}}{dx d\cos\theta}(s)$),

However, the selection cuts distort the probability density and we need to consider in addition the efficiency as a function of x and $\cos \theta$ at each nominal centre-of-mass energy, $\epsilon(s, x, \cos \theta)$.

In the next section we will explain why, we will use the probability density as a function of $\cos \theta$, but we will integrate it in the forward and backward hemispheres. In other words, the forward-backward asymmetry is computed counting the number of events in the forward and backward hemispheres, instead of using the angular distribution. In this way we only need to know, as a function of the radiated energy, the efficiency to find an event in each hemisphere

$$\epsilon_{F(B)}(s, x) = \int_{0(-1)}^{1(0)} \epsilon(s, x, \cos \theta) d\cos \theta$$

where ϵ_F denotes the efficiency in the FORWARD hemisphere and ϵ_B in the BACKWARD hemisphere.

These correction functions are computed using the generated Monte Carlo events in table 4.1. The distribution in x is binned in intervals of $\Delta x = 0.04$, which is four times the experimental resolution, and satisfies the criteria ($\Delta x > \frac{\Gamma_Z}{M_Z}$), and in intervals of $\Delta x = 0.08$ when ($0.16 \leq x < 0.64$) due to the small number of events there. The analysis is restricted up to $x_{\max.} = 0.64$ which corresponds to an effective centre-of-mass energy of 55 GeV, at $\sqrt{s} = 91.2$ GeV. This lower limit spans the energy region not covered by present accelerators.

The computed efficiencies at the different LEP nominal energies ($\epsilon_{F(B)}^i(s)$) to find an event in the interval $x_i \leq x < x_{i+1}$ are shown explicitly in Appendix C, and some of them are plotted in figure 4.6, where

$$\epsilon_{F(B)}^i(s) \equiv \sum_{j=1, \text{nbins}} \epsilon_{F(B)}^{ij}(s) \frac{\hat{\sigma}_{F(B)}^j(s)}{\hat{\sigma}_{F(B)}^i(s)} \quad (4.7)$$

with

$$\epsilon_{F(B)}^{ij}(s) = \frac{N_{sel}(s, x_i \leq x_{rec} < x_{i+1}, \cos \theta_{rec} \geq (<)0)}{N_{gen}(s, x_j \leq x_{gen} < x_{j+1}, \cos \theta_{gen} \geq (<)0)} \quad (4.8)$$

and

$$\hat{\sigma}_{F(B)}^i(s) \equiv \int_{x_i}^{x_{i+1}} dx H(s, x) \hat{\sigma}_{F(B)}(s, x)$$

where the radiator function $H(s, x)$ and the total cross section $\hat{\sigma}(s' = s(1-x))$ have been introduced in chapter 2.

The efficiency of the selection is not independent of x , and in fact its dependence is far from being trivial. This is due to the cut on the angular acceptance ($\cos \theta < 0.9$), and the cuts on the reconstructed photon in the detector.

The different shape in both hemispheres can be explained as a kinematic effect, due to the fact that events are produced asymmetrically, ($\hat{A}_{FB} \neq 0$ when $x \neq 0$), and therefore the acceptance cut is less effective in one hemisphere or the other depending on the sign of the asymmetry. Moreover, events produced at low angles that would have been accepted in the CM system, can be lost due to the effect of the boost, because one of the two tracks lies outside the acceptance.

There is a common characteristic in the qualitative behaviour at the different nominal centre-of-mass energies, that is a sizable drop in the efficiency after the first bin. This can be traced back to the cuts on the number of photons detected

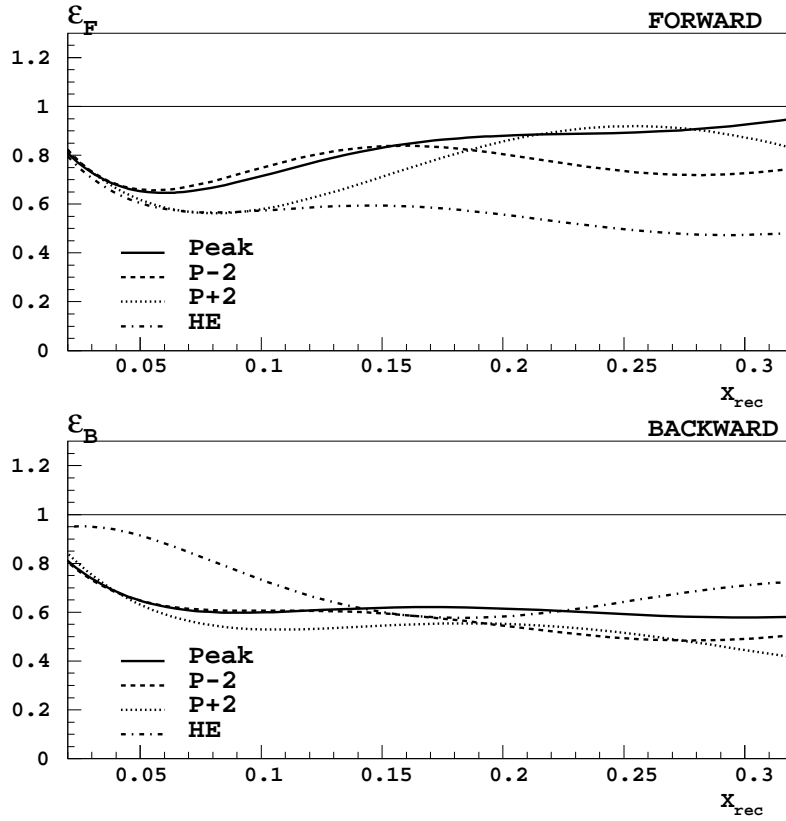


Figure 4.6: $\epsilon_{F,B}(x)$ at different nominal centre-of-mass energies.

and the cuts on the consistency of the computed energy radiated with the radiative dimuon hypothesis. It is clear that when $x \sim 0$, the effect of these cuts on the radiated photon is much lower, essentially because there are no photons detected in most of these events.

The relative change of $\epsilon_{F(B)}$ from bin to bin computed from the numbers in table C.1, will be used in the next section to correct the probability density of equation 2.17.

4.4 The loglikelihood function

As we have explained in section 2.17, the process $e^+e^- \rightarrow \mu^+\mu^-$ in a wide range of energies can be parameterized in the S-matrix language as a function of six parameters,

$$M_Z, \Gamma_Z, r_\mu^{tot}, j_\mu^{tot}, r_\mu^{fb}, j_\mu^{fb}$$

In principle, we could use directly formula 2.17 corrected for the experimental efficiency to build a loglikelihood function and extract the S-matrix parameters from the measured $\cos\theta$ and x in an event-by-event basis.

However, as we have explained in section 2.1.1, the probability density of equation 2.17 is well defined only when $|\hat{A}_{fb}| < 3/4$. This implies that when one tries to extract the forward-backward asymmetry from a loglikelihood fit using equation 2.17, one is “condemned” to get a value lower than this limit, because the probability to have a higher value is strictly zero if there are events found in all the angular range.

In fact, there are two regions in energy, ($\sqrt{s} \sim 80$ GeV and $\sqrt{s} \sim 113$ GeV), where the SM predictions for the forward-backward asymmetry is very close ¹ to $|\hat{A}_{fb}| \sim 3/4$. This implies that the parameter-space of the S-matrix parameters is heavily reduced at these energies, and they will be strongly correlated. To be more precise, if we consider that r_μ^{tot} and r_μ^{fb} are determined by the measurements taken at $x \sim 0$, the forward-backward asymmetry at an effective centre-of-mass energy around 80 GeV will be given by,

$$\hat{A}_{fb}((80 \text{ GeV})^2) \sim \frac{3}{4} \left[\frac{((80 \text{ GeV})^2 - \overline{M}_Z^2)J_{fb}}{C + ((80 \text{ GeV})^2 - \overline{M}_Z^2)J_{tot}} \right]$$

with a “constant” contribution from the Z^0 and γ interchange to the total cross-section at the level of $C \sim (39.5 \text{ GeV})^2$. In this case the ratio between brackets is very close to one, and we can write for a small variation in the forward-backward asymmetry

$$\Delta\hat{A}_{fb} \sim \frac{3}{4J_{fb}} (\Delta J_{fb} + \Delta J_{tot})$$

¹ $|\hat{A}_{fb}|$ is slightly lower than 3/4 due to the inclusion of non-photonic radiative corrections.

It is clear from the above expression that J_{fb} and J_{tot} are not independent from each other due to the limit $|\hat{A}_{fb}| < 3/4$. In this way any fluctuation in J_{fb} upwards will necessary be compensated by a fluctuation downwards, and in fact, they are almost 100% anticorrelated.

Strictly speaking, this is not a problem. The correlation is what it is, and it just complicates the interpretation of the extracted electroweak parameters. However, there is an alternative way in which these correlations are removed. The limit on $|\hat{A}_{fb}|$ is a consequence of the angular distribution imposed, but it is not present if we come back to the “original” definition of the forward-backward asymmetry,

$$\hat{A}_{fb} = \frac{\hat{\sigma}_f - \hat{\sigma}_b}{\hat{\sigma}_f + \hat{\sigma}_b} \equiv \frac{N_F - N_B}{N_F + N_B}$$

computed from the difference in the number of events in the forward and backward hemispheres. This also has the advantage of simplifying the corrections due to the experimental cuts, and the loss of sensitivity in the electroweak parameters is negligible small.

In this case, the probability density for an event being in the interval $x_i \leq x < x_{i+1}$ will be given by:

$$\begin{aligned} P^0(x_i, \cos \theta \geq 0, s) &\equiv \frac{1}{2} \epsilon_F^i(s) (\hat{\sigma}^i(s) + \hat{\sigma}_{fb}^i(s)) \\ P^0(x_i, \cos \theta < 0, s) &\equiv \frac{1}{2} \epsilon_B^i(s) (\hat{\sigma}^i(s) - \hat{\sigma}_{fb}^i(s)) \end{aligned} \quad (4.9)$$

and

$$\begin{aligned} \hat{\sigma}^i(s) &\equiv \int_{x_i}^{x_{i+1}} dx H(s, x) \hat{\sigma}(s, x) \\ \hat{\sigma}_{fb}^i(s) &\equiv \int_{x_i}^{x_{i+1}} dx \tilde{H}(s, x) \hat{\sigma}_{fb}(s, x) \end{aligned}$$

where the radiator functions $H(s, x)$ and $\tilde{H}(s, x)$, the total cross section $\hat{\sigma}(s' = s(1-x))$ and $\hat{\sigma}_{fb}(s' = s(1-x))$ have been introduced in chapter 2, whereas the correction functions $\epsilon_{F(B)}^i(s)$ have been introduced in the previous section.

With this definition, the forward-backward asymmetry is just bounded to be $|\hat{A}_{fb}| < 1$, and the probability density in equation 4.9 is well defined in a wide region of the parameter space.

On the other hand, as we have discussed in section 2.1.2, the effect of the I-F QED interference on $\hat{\sigma}$ is completely negligible for a convenient minimum size

of the binning as the one we have choose ($\Delta x \sim 0.04$). But even with this bin size, the effect on $\hat{\sigma}_{fb}$ cannot be completely neglected, and we should not forget that this effect is not present in the Monte Carlo simulation, and therefore the correction functions $\epsilon_{F(B)}^i(s)$ are not correcting the theoretical probability density for this effect.

In order to take the I-F QED interference into account, equation 4.9 is modified with

$$\hat{\sigma}_{fb}^i(s) \rightarrow \hat{\sigma}_{fb}^i(s) + \delta_{FB}^i(s)$$

where $\delta_{FB}^i(s)$ is the contribution of the I-F QED interference to the antisymmetric cross section, in the angular acceptance $|\cos \theta| < 0.9$ and in the interval $x_i \leq x < x_{i+1}$. This is computed from an analytical calculation up to $\mathcal{O}(\alpha)$, integrating the expression for the interference ($\delta(\sigma_f - \sigma_b)$) in $\cos \theta$ up to the limit in the angular acceptance ($|\cos \theta| < 0.9$) and x between the corresponding limits (x_i and x_{i+1}). These corrections are essentially independent of the electroweak parameters we want to measure, except from the Z^0 width. But as we will show later, Γ_Z is constrained by the hadronic lineshape with high precision, so that the uncertainty in δ_{FB}^i is negligible.

We have cross-checked the computed effect δ_{FB}^i by generating and reconstructing 3×10^5 MC events with KORALZ 4.0 [49], using the complete calculation to $\mathcal{O}(\alpha)$ that includes I-F QED interference, (parameter KEYRAD set to 1). In this conditions, the one dimensional probability density $\frac{d\hat{\sigma}}{dx}(s)$ is not well reproduced, due to the importance of higher order corrections, but the effect of including or not the I-F QED interference is confirmed to be negligible for $\hat{\sigma}$ and compatible with the analytic calculation for δ_{FB}^i , at least for the first bins where there is enough statistics to do these checks and where the corrections are non-negligible. These corrections have been computed for each of the nominal LEP centre-of-mass energies, and as an example of their size, table 4.4 shows the SM predictions for $\hat{\sigma}_{fb}^i$ (corresponding to the central values quoted in table 2.1), and the computed δ_{FB}^i at $\sqrt{s} \sim 91.2$ GeV for the first four bins in x .

In addition, since we are going to extract the electroweak parameters on an event-by-event basis, we need to know the nominal centre-of-mass energy of each individual collision. We have already mentioned in section 3.1.1 that there is a sizable beam energy spread between the individual electron and positron collisions

$x_i \leq x < x_{i+1}$	$\hat{\sigma}_{fb}^i$	δ_{FB}^i	$\delta_{FB}^i(\text{MC})$
$0.00 \leq x < 0.04$	0.00606	+0.00352	+0.0048 \pm 0.0031
$0.04 \leq x < 0.08$	-0.00271	+0.00012	-0.00047 \pm 0.00027
$0.08 \leq x < 0.12$	-0.00104	+0.00002	+0.00001 \pm 0.00001
$0.12 \leq x < 0.16$	-0.00057	+0.00001	+0.00001 \pm 0.00001

Table 4.4: I-F QED interference corrections to the antisymmetric cross-section at $\sqrt{s} \sim 91.2$ GeV, when $|\cos\theta| < 0.9$ and $x_i \leq x < x_{i+1}$. The last column shows the results obtained from the 3×10^5 MC events.

of about 55 MeV (depending on the year of data taking). This effect is taken into account by convolving equation 4.9 with a gaussian probability density

$$P(x_i, \cos\theta \geq (<)0, s) \equiv \int_{-\infty}^{\infty} ds'' P^0(x_i, \cos\theta \geq (<)0, s'') \exp\left\{-\frac{-(\sqrt{s} - \sqrt{s''})^2}{2\sigma_{bs}^2}\right\}$$

where σ_{bs} is the centre-of-mass beam energy spread that is different from year to year. In practice, the numerical integration is only performed in the interval $[-6\sigma_{bs}, +6\sigma_{bs}]$.

The probability to find in the data sample an event with nominal centre-of-mass energy $\sqrt{s_j}$ is proportional to the integrated luminosity taken at this energy, \mathcal{L}_j . The final probability density to find an event with: centre-of-mass energy $\sqrt{s_j}$, effective centre-of-mass energy $\sqrt{s_i} = \sqrt{s_j(1-x_i)}$ and polar angle $\cos\theta_i$ is given by the product

$$\mathcal{L}_j \cdot P(x_i, \cos\theta_i, s_j)$$

In this way, we can find those S-matrix parameters that maximize the normalized product of probabilities, (equivalently the normalized sum of the logarithms of the probabilities), or introducing a negative sign those that minimize the loglikelihood function

$$\frac{-2}{\text{Normal.}} \left[\sum_{j=1, N_p} \sum_{i=1, N_{evt}} \ln(\mathcal{L}_j P(x_i, \cos\theta_i, s_j)) \right] \quad (4.10)$$

where N_p is the number of energy points to analyze, N_{evt} is the number of selected events at each energy point, and ‘‘Normal.’’ is the sum of the probabilities for all the possible values of $\sqrt{s_j}$, x_i and $\cos\theta_i$. The factor two is introduced in order to have the same definition of errors as if we were using a χ^2 minimization.

Total normalization constraint (χ_1^2)

Note that in this process the S-matrix parameters are extracted from the “shape” of the loglikelihood function we have just introduced. This is the reason why we don’t need to know the total efficiency of the selection, and we are only concern with the relative changes as a function of the three quantities that enter in the loglikelihood function, namely: \sqrt{s} , x and $\cos \theta$.

In this way, one can introduce a constraint computed from the total cross section measurements [58] and [59] in ALEPH (σ_j^{exp}),

$$\chi_1^2 = \frac{\left(\sum_{j=1, N_p} \mathcal{L}_j (\sigma_j^{exp} - \sigma_j^{th})\right)^2}{\Delta^2} \quad (4.11)$$

where σ_j^{th} is the total cross-section, (convolved with ISR), for each energy point as a function of the S-matrix parameters. The error in the denominator, Δ^2 , is computed from the errors on the total cross-section ($\sigma_j^{exp} \pm \Delta\sigma_j^{stat} \pm \Delta\sigma_j^{syst}$), and the luminosity measurements ($\mathcal{L}_j \pm \Delta\mathcal{L}_j^{stat} \pm \Delta\mathcal{L}_j^{syst}$), with

$$\begin{aligned} \Delta^2 = & \sum_{j=1, N_p} \sum_{k=1, N_p} (\mathcal{L}_j \Delta\sigma_j)^2 + (\sigma_j^{exp} \Delta\mathcal{L}_j)^2 + (\sigma_j^{th} \Delta\mathcal{L}_j)^2 + \\ & \rho_{jk} \sigma_j^{exp} \sigma_k^{exp} \Delta\mathcal{L}_j \Delta\mathcal{L}_k + \rho_{jk} \sigma_j^{th} \sigma_k^{th} \Delta\mathcal{L}_j \Delta\mathcal{L}_k + \\ & \mathcal{L}_j \mathcal{L}_k \Delta\sigma_j^{syst} \Delta\sigma_k^{syst} \end{aligned}$$

where $\Delta\sigma_j^{syst}$ are considered to be 100% correlated between different energy points, and ρ_{jk} is the luminosity correlation matrix shown in table 4.5.

	90 data	91 data	92 data	92 (SI)	93 data	94 data	95 data	95 (HE)
90 data	1.000	0.376	0.376	0.202	0.247	0.000	0.000	0.000
91 data		1.000	0.629	0.269	0.331	0.000	0.000	0.000
92 data			1.000	0.269	0.331	0.000	0.000	0.000
92 (SI)				1.000	0.685	0.630	0.667	0.000
93 data					1.000	0.764	0.810	0.000
94 data						1.000	0.837	0.000
95 data							1.000	0.000
95 (HE)								1.000

Table 4.5: Luminosity correlation matrix between different years of data taking. 92(SI) corresponds to the data taken in 1992 after the installation of the SICAL luminosity detector.

The experimental measurements of σ_j^{exp} and the integrated luminosity at each energy point \mathcal{L}_j are shown in table 4.6 from references [58] and [59].

This constraint determines r_μ^{tot} with high precision, and therefore this parameter is essentially uncorrelated with the others.

Hadronic lineshape constraint (χ_2^2)

The Z mass and the Z width are determined with high precision from the ALEPH hadronic lineshape in reference [57], and therefore it does not make too much sense extracting these two parameters from the muon lineshape. So that, the ALEPH measurements of M_Z and Γ_Z in the S-matrix formalism, ($M_Z^{exp} = 91.1978 \pm 0.0074$ GeV and $\Gamma_Z^{exp} = 2.4928 \pm 0.0049$ GeV) are used as a second constraint with

$$\chi_2^2 = \frac{(M_Z - M_Z^{exp})^2}{(\Delta M_Z)^2} + \frac{(\Gamma_Z - \Gamma_Z^{exp})^2}{(\Delta \Gamma_Z)^2} \quad (4.12)$$

In this way, the final function to be minimized is:

$$l = \frac{-2}{\text{Normal.}} \left[\sum_{j=1, N_p} \sum_{i=1, N_{evt}} \ln(\mathcal{L}_j P(x_i, \cos \theta_i, s_j)) \right] + \chi_1^2 + \chi_2^2 \quad (4.13)$$

	\sqrt{s} (GeV)	$\mathcal{L} \pm \Delta\mathcal{L}$ (nb^{-1})	σ (nb) \pm stat. \pm syst.	Nevt
90 data	88.223	480.2 ± 2.7	$0.248 \pm 0.025 \pm 0.0012$	94
	89.217	520.4 ± 3.0	$0.503 \pm 0.034 \pm 0.0025$	190
	90.217	444.0 ± 2.5	$0.908 \pm 0.049 \pm 0.0045$	302
	91.215	3632 ± 21	$1.429 \pm 0.022 \pm 0.0071$	3950
	92.207	553.9 ± 3.2	$1.006 \pm 0.047 \pm 0.0050$	426
	93.209	594.2 ± 3.4	$0.638 \pm 0.036 \pm 0.0032$	282
	94.202	641.7 ± 3.7	$0.437 \pm 0.029 \pm 0.0022$	208
91 data	88.464	670.6 ± 2.9	$0.262 \pm 0.022 \pm 0.0013$	137
	89.455	798.4 ± 3.4	$0.542 \pm 0.029 \pm 0.0027$	335
	90.212	748.2 ± 3.2	$0.926 \pm 0.039 \pm 0.0046$	526
	91.207	2939 ± 13	$1.540 \pm 0.025 \pm 0.0077$	3659
	91.238	4608 ± 20	$1.479 \pm 0.020 \pm 0.0074$	5458
	91.952	693.8 ± 3.0	$1.212 \pm 0.047 \pm 0.0061$	662
	92.952	679.6 ± 2.9	$0.665 \pm 0.035 \pm 0.0033$	342
93.701	764.6 ± 3.3	$0.517 \pm 0.029 \pm 0.0026$	295	
92 data	91.270	8749 ± 19	$1.484 \pm 0.016 \pm 0.0074$	10192
	91.276	13684 ± 59	$1.499 \pm 0.012 \pm 0.0075$	14390
93 data	89.430	8065 ± 15	$0.484 \pm 0.009 \pm 0.0011$	3055
	91.184	9131 ± 17	$1.480 \pm 0.015 \pm 0.0033$	10718
	91.284	5331.9 ± 9.7	$1.471 \pm 0.019 \pm 0.0033$	6176
	93.012	8693 ± 16	$0.674 \pm 0.0099 \pm 0.0015$	4539
94 data	91.194	42704 ± 75	$1.4792 \pm 0.0068 \pm 0.0035$	50077
95 data	89.438	8295 ± 16	$0.491 \pm 0.0086 \pm 0.0011$	3178
	91.280	4961.3 ± 9.3	$1.465 \pm 0.019 \pm 0.0033$	5750
	92.970	9355 ± 17	$0.7132 \pm 0.0096 \pm 0.0015$	5174
	130.24	2877 ± 23	$0.0229 \pm 0.0034 \pm 0.0004$	35
	136.21	2863 ± 23	$0.0206 \pm 0.0032 \pm 0.0003$	28

Table 4.6: Inclusive cross-section and luminosities used in the evaluation of the normalization constraint, χ_1^2 . The total number of events selected are shown in the last column.

Chapter 5

Results and systematic studies

In the previous chapter we have described the experimental procedure to determine the effective centre-of-mass energy, ($\sqrt{s'} = \sqrt{s(1-x)}$), in an event-by-event basis. We have also built a loglikelihood function based on the probability that one selected event has a particular value for s, x and $\cos \theta$ as a function of the S-matrix parameters introduced in chapter 2, ($M_Z, \Gamma_Z, r_\mu^{tot}, j_\mu^{tot}, r_\mu^{fb}, j_\mu^{fb}$).

In section 5.1 we present the specific results of this analysis in terms of the S-matrix electroweak parameters, and a specific study of the systematic uncertainties in the extraction of these parameters is shown in section 5.2.

As we have mentioned before, the SM predicts a cancellation of some helicity amplitudes at $\sqrt{s'} \sim 80$ GeV and $\sqrt{s'} \sim 113$ GeV. This means that in these energy regions we have minimal “background” from the SM for the search of new physics effects. A specific study in terms of helicity cross sections is presented in section 5.3.

Finally, once we have confirmed the agreement of the observed energy dependence with the SM predictions, we can extract restrictions on new theories that would predict the existence of extra Z bosons. The last section is devoted to show these limits for a specific set of theoretical models.

5.1 Extraction of the S-matrix parameters

The data sample used was recorded in the years 1990 to 1995 at nominal centre-of-mass energies from 88.2 GeV up to 136.2 GeV, and corresponds to a total integrated

luminosity of 143.5 pb^{-1} . A total of 130,178 events pass the selection cuts. Table 4.6 shows the number of muon pair candidates selected at each energy point.

Equation 4.13 is minimized with respect the S-matrix parameters and the results are shown in table 5.1.

	SM predictions	Fit results	Correlation matrix			
r_μ^{tot}	0.14298	0.14186 ± 0.00080	1.00	0.04	0.04	0.11
j_μ^{tot}	0.004	-0.033 ± 0.022		1.00	-0.04	-0.34
r_μ^{fb}	0.00278	0.00273 ± 0.00054			1.00	0.13
j_μ^{fb}	0.800	0.807 ± 0.026				1.00

Table 5.1: Results obtained for the electroweak parameters from a maximum log-likelihood fit to the events selected. The SM predictions are computed with $M_Z = 91.1863 \text{ GeV}$, $\alpha^{-1}(M_Z^2) = 128.896$, $M_{\text{top}} = 175 \text{ GeV}$ and $M_H = 150 \text{ GeV}$.

The results are in good agreement with the SM predictions, and the statistical precision of the measured j_μ^{tot} and j_μ^{fb} has improved by a factor $\frac{1}{\sqrt{2}}$ from the previous measurement in ALEPH [57] using the same data ($j_\mu^{\text{tot}} = -0.011 \pm 0.033$, $j_\mu^{\text{fb}} = 0.823 \pm 0.038$), equivalently to have effectively doubled the statistics.

In particular, the ‘‘apparent’’ problem that was observed in the past in ALEPH with the energy dependence of the leptonic forward-backward asymmetries [60], where j_μ^{fb} was higher than the SM predictions by more than two gaussian sigmas with the data recorded up to 1993, (or almost four gaussian sigmas when combining the three leptonic species), seems to be compensated with the addition of 1995 data and the new information added by our method.

For instance, almost 50% of all the data taken at LEP was accumulated in 1994 at a single centre-of-mass energy $\sqrt{s} = 91.194 \text{ GeV}$, so that there was no information in this data for the parameters that describe the energy dependence: j_μ^{tot} and j_μ^{fb} . In table 5.2 one can see the results obtained for the S-matrix parameters when only 1994 data is used, and when the rest of the data is added in successive steps. Although it seems that the data taken before 1994 prefers a higher value for j_μ^{fb} , the different measurements are statistically compatible with a $\chi^2 = 5.4$ for the combination of seven periods of data taking, and therefore one can conclude that we were victims of a statistical fluctuation.

One can compare directly the number of events observed in each bin of energy,

	r_μ^{tot}	j_μ^{tot}	r_μ^{fb}	j_μ^{fb}
94 data	0.14185 ± 0.00100	-0.037 ± 0.052	0.00227 ± 0.00088	0.753 ± 0.074
93 \rightarrow 94 data	0.14132 ± 0.00097	-0.065 ± 0.033	0.00321 ± 0.00073	0.820 ± 0.042
92 \rightarrow 94 data	0.14160 ± 0.00086	-0.075 ± 0.030	0.00313 ± 0.00063	0.821 ± 0.037
91 \rightarrow 94 data	0.14176 ± 0.00083	-0.075 ± 0.029	0.00281 ± 0.00059	0.830 ± 0.036
90 \rightarrow 94 data	0.14166 ± 0.00083	-0.073 ± 0.027	0.00277 ± 0.00058	0.839 ± 0.034
90 \rightarrow 95 data	0.14188 ± 0.00080	-0.036 ± 0.023	0.00272 ± 0.00055	0.808 ± 0.028
90 \rightarrow 95 (+HE)	0.14186 ± 0.00080	-0.033 ± 0.022	0.00273 ± 0.00054	0.807 ± 0.026

Table 5.2: Results obtained for the electroweak parameters for different samples of data as a function of the running period.

with the predictions of the fit results. The results of this direct comparison are shown in table 5.3 where we have accumulated events coming from different nominal centre-of-mass energies in single bins of $\sqrt{s'}$.

$\sqrt{s'}$ GeV	$\langle\sqrt{s'}\rangle$ GeV	N_F^{obs}	N_F^{fit}	Pull	N_B^{obs}	N_B^{fit}	Pull
55 \rightarrow 65	63.13	11	10.5	+0.1	17	19.9	-0.5
65 \rightarrow 75	72.18	22	16.9	+1.1	37	39.9	-0.5
75 \rightarrow 80	78.29	17	12.3	+1.2	35	38.0	-0.5
80 \rightarrow 84	82.50	26	23.2	+0.6	74	76.9	-0.3
84 \rightarrow 86	85.20	70	64.9	+0.6	169	168.1	+0.1
86. \rightarrow 87.8	87.49	160	153.2	+0.5	306	297.5	+0.5
87.8 \rightarrow 88.6	88.37	89	89.0	0.0	145	143.9	+0.1
88.6 \rightarrow 89.6	89.42	3336	3399.4	-1.1	4683	4562.9	+1.8
89.6 \rightarrow 90.3	90.21	376	378.7	-0.1	459	438.4	+1.0
90.3 \rightarrow 91.3	91.22	55258	54873.5	+1.6	53974	53778.6	+0.8
91.3 \rightarrow 92.3	92.05	619	609.8	+0.4	511	536.8	-1.1
92.3 \rightarrow 93.3	92.99	5268	5216.3	+0.7	4036	3985.3	+0.8
93.3 \rightarrow 100	93.96	239	228.0	+0.7	183	154.1	+2.3
100 \rightarrow 127	110.25	7	6.1	+0.2	1	1.7	0.0
127 \rightarrow 133	130.17	17	13.8	+0.7	3	2.4	+0.2
133 \rightarrow 136	136.21	13	9.3	+1.0	3	1.8	+0.6

Table 5.3: Number of observed events in the different intervals of $\sqrt{s'}$ compared with the number of events predicted from the fit results.

From the loglikelihood fit we have obtained the most probable values for the S-matrix parameters, but we cannot say anything on the actual goodness of the

fit. In order to quantify the confidence level of the fit, we have used a Poisson distribution to compute the probability, $P(N_i^{obs}, N_i^{fit})$, to see N_i^{obs} events in the interval $\sqrt{s'_{i+1}} > \sqrt{s'} \geq \sqrt{s'_i}$ when the expected number is N_i^{fit} . This probability can be interpreted in terms of a “gaussian” error, which can be used to build a χ^2 summing the square of the “pulls” (δ_i) defined with the implicit equation,

$$P(N_i^{obs}, N_i^{fit}) = \frac{2}{\sqrt{2\pi}} \int_0^{\delta_i} \exp\left[-\frac{x^2}{2}\right] dx$$

and the contribution of the two constraints introduced in the previous chapter.

$$\chi^2 = \sum_i (\delta_i)^2 + \chi_1^2 + \chi_2^2$$

The confidence level of the results shown in table 5.1 is 35% with a $\frac{\chi^2}{d.o.f.} = \frac{193.7}{187}$. We have checked that the parameters obtained from the loglikelihood fit and shown in table 5.1 minimize this χ^2 too.

The statistical behaviour of the results shown in table 5.3 is quite reasonable. The number of measurements that is expected to be at more than one sigma is 10.1 while we found 9, (1.4 expected to be at more than two sigmas and we found 1).

The results shown in table 5.3 are the direct measurements of our analysis but, usually, one wants to give “universal” measurements which are deconvolved from the specific selection procedure and that can be compared directly with theory. With this philosophy, we can define $\hat{\sigma}$ and \hat{A}_{fb} as:

$$\hat{\sigma}_F(\langle\sqrt{s'}\rangle) \equiv \hat{\sigma}_F^{fit}(\langle\sqrt{s'}\rangle) \cdot \frac{N_F^{obs}}{N_F^{fit}} \quad (5.1)$$

$$\hat{\sigma}_B(\langle\sqrt{s'}\rangle) \equiv \hat{\sigma}_B^{fit}(\langle\sqrt{s'}\rangle) \cdot \frac{N_B^{obs}}{N_B^{fit}} \quad (5.2)$$

$$\hat{\sigma} = \hat{\sigma}_F + \hat{\sigma}_B$$

$$\hat{\sigma}_{fb} = \hat{\sigma}_F - \hat{\sigma}_B$$

$$\hat{A}_{fb} = \frac{\hat{\sigma}_{fb}}{\hat{\sigma}}$$

where $\hat{\sigma}_{F(B)}^{fit}$ is the predicted cross section from the fitted S-matrix parameters, in the forward (backward) hemispheres at the mean centre-of-mass energy quoted in table 5.3.

In this way, we have a measurement of the deconvolved cross section and forward-backward asymmetry in a wide range of energies. The results are shown in table 5.4.

In fig. 5.1 and fig. 5.2 one can compare also this measurements with previous measurements made at PEP [62], PETRA [63] and TRISTAN [64] at lower energies. These measurements were quoted with α evaluated at $q^2 = 0$, i.e. correcting for the running of the fine structure “constant” α . In order to be consistent with the S-matrix formulae introduced in chapter 2, which includes this running in the definition of r^γ , we have corrected them back.

In these figures, one can observe a nice agreement between the results of the fit in a wide region of energies, spanning from 20 GeV up to 136 GeV.

$\langle\sqrt{s'}\rangle$ GeV	σ^0 (nb)	σ^{fit}	pull	A_{FB}^0	A_{FB}^{fit}	pull
63.12	0.0253 ± 0.0085	0.0278	-0.3	$-0.35_{-0.19}^{+0.22}$	-0.435	+0.5
72.18	0.0263 ± 0.0037	0.0263	0.0	$-0.52_{-0.12}^{+0.14}$	-0.637	+1.0
78.29	0.0325 ± 0.0048	0.0330	-0.1	$-0.60_{-0.11}^{+0.14}$	-0.716	+1.0
82.50	0.0520 ± 0.0053	0.0525	-0.1	$-0.593_{-0.082}^{+0.096}$	-0.641	+0.6
85.20	0.0956 ± 0.0061	0.0934	+0.4	$-0.472_{-0.059}^{+0.063}$	-0.499	+0.5
87.49	0.219 ± 0.010	0.2118	+0.7	$-0.317_{-0.045}^{+0.047}$	-0.324	+0.1
88.37	0.336 ± 0.022	0.3341	+0.1	-0.250 ± 0.067	-0.246	-0.1
89.42	0.6759 ± 0.0075	0.6710	+0.6	-0.171 ± 0.011	-0.149	-2.0
90.21	1.276 ± 0.044	1.2487	+0.6	-0.101 ± 0.036	-0.075	-0.7
91.23	2.0018 ± 0.0060	1.9911	+1.8	0.0216 ± 0.0030	0.0199	+0.6
92.05	1.322 ± 0.040	1.3403	-0.5	0.128 ± 0.030	0.096	+1.0
92.99	0.6570 ± 0.0068	0.6498	+1.1	0.178 ± 0.010	0.179	-0.1
94.03	0.381 ± 0.018	0.3466	+1.9	0.201 ± 0.049	0.260	-1.2
110.46	0.019 ± 0.010	0.0175	+0.1	$0.75_{-0.46}^{+0.21}$	0.788	-0.2
130.20	0.0102 ± 0.0028	0.0083	+0.7	$0.73_{-0.25}^{+0.16}$	0.736	0.0
136.21	0.0104 ± 0.0026	0.0072	+1.2	$0.66_{-0.30}^{+0.20}$	0.712	+0.2

Table 5.4: Measured cross sections and asymmetries compared with those predicted from the fit results.

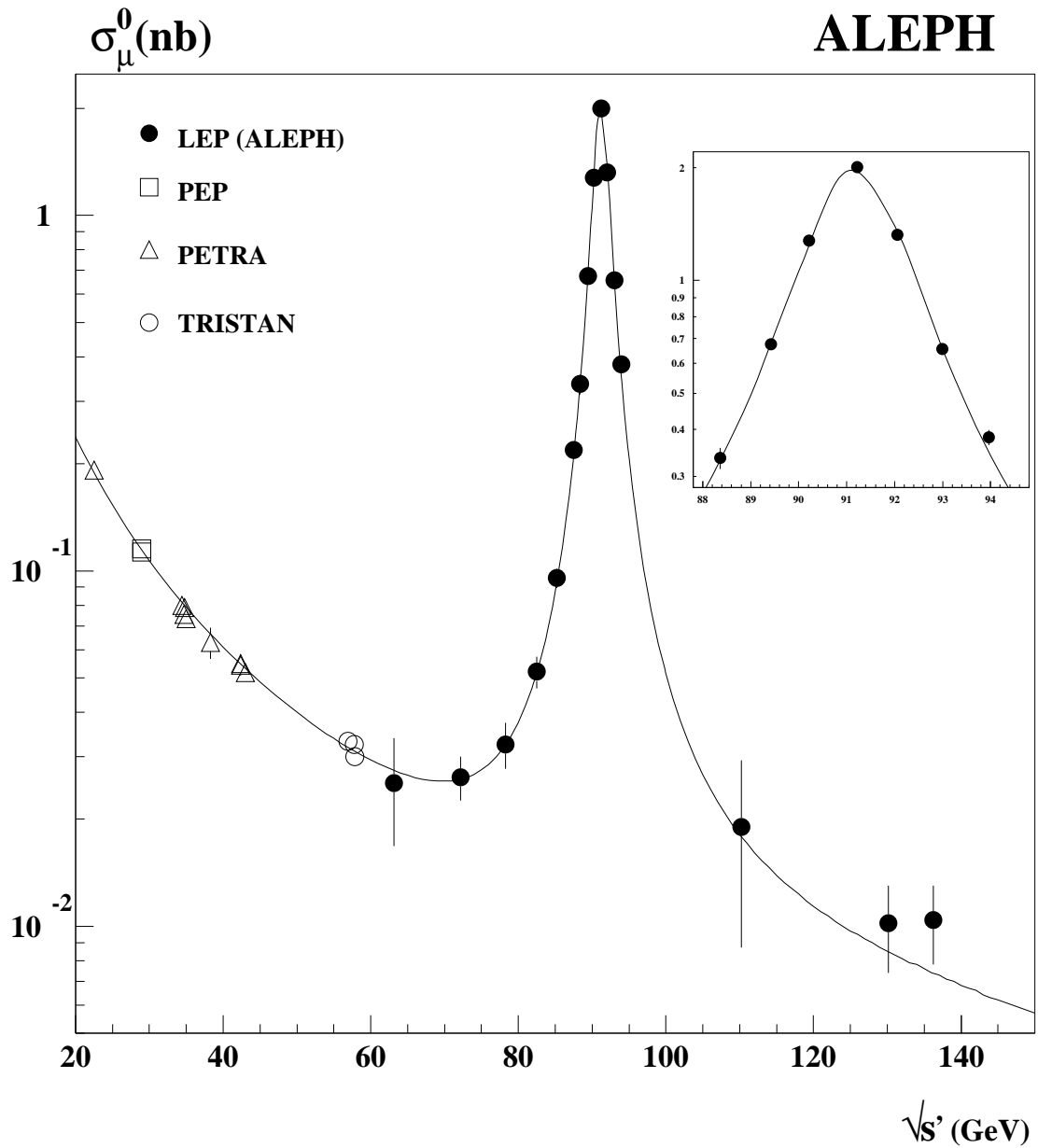


Figure 5.1: Measured cross sections of muon-pair production compared with the fit results. For comparison the measurements at lower energies from PEP, PETRA and TRISTAN are included. The region around the Z pole has been amplified in the inserted box.

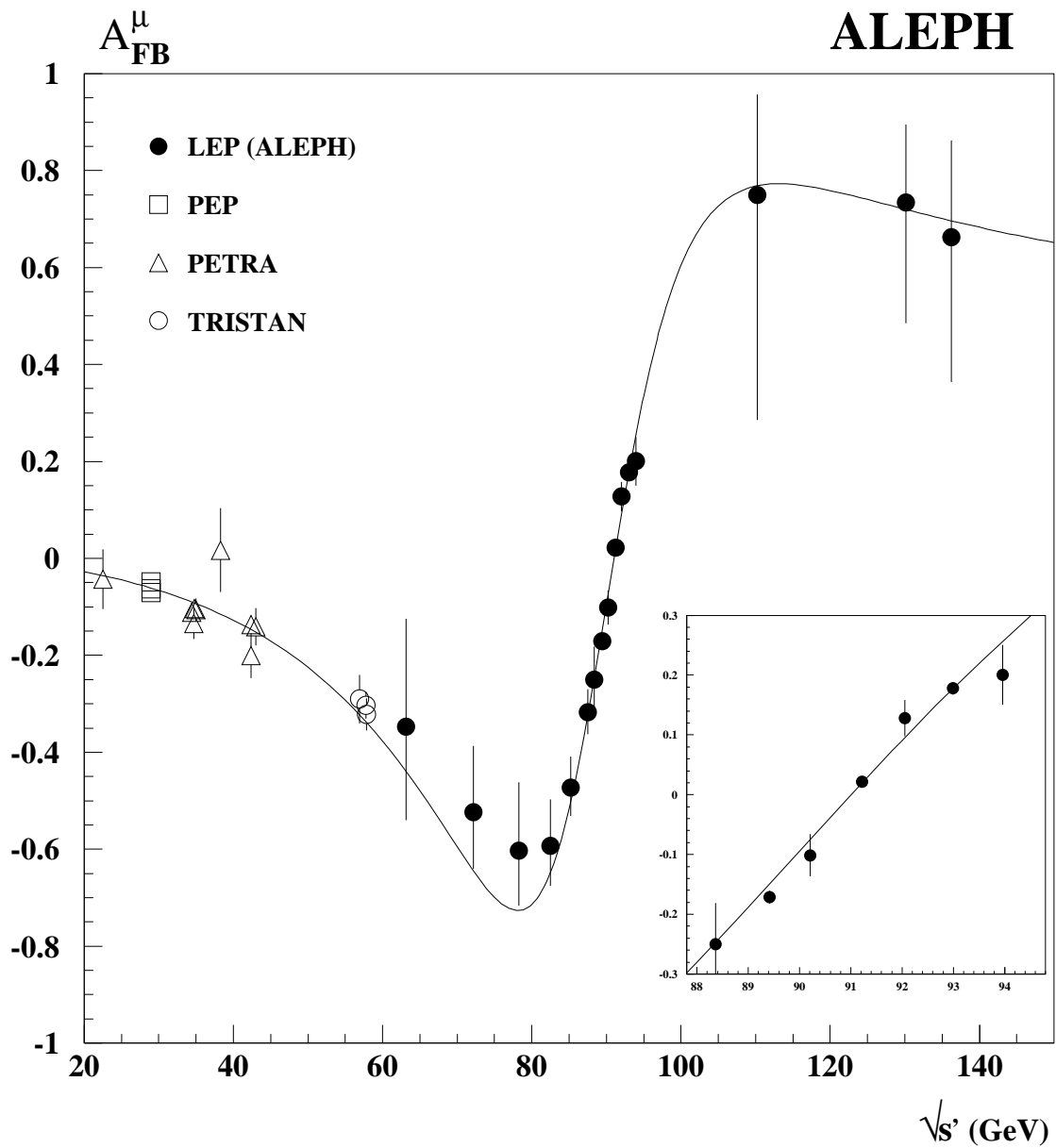


Figure 5.2: Measured forward-backward asymmetries of muon-pair production compared with the fit results. For comparison the measurements at lower energies from PEP, PETRA and TRISTAN are included. The region around the Z pole has been amplified in the inserted box.

5.2 Systematic studies

In this section we have evaluated the systematic uncertainties in the extraction of the S-matrix parameters. The main systematic errors are due to the limited MC statistics used, and the uncertainty on the effect of the I-F QED interference.

Monte Carlo statistics

One obvious source of systematic errors on the fitted electroweak parameters, is the limited MC statistics used to determine $\epsilon_{F(B)}^i$. In order to evaluate this error, we have generated different samples of $\epsilon_{F(B)}^i$ according to a multinomial distribution with the generated statistics at each energy point in table 4.1. We have generated a total of fifty different samples of efficiencies, and repeated the loglikelihood fit fifty times.

The results of these fits are distributed around the central values quoted in table 5.1 following a gaussian distribution. The R.M.S. of these distributions are taken as a systematic error for each of the electroweak parameters, due to the statistical uncertainty on $\epsilon_{F(B)}^i$. Table 5.5 shows the specific values.

Precision of the I-F QED interference corrections

We have already mentioned that the analytic computation of δ_{FB}^i in Eq. (4.10) has been cross-checked with 3×10^5 MC events generated with KORALZ at $\mathcal{O}(\alpha)$. In any case, this is just a computation to $\mathcal{O}(\alpha)$ and, likely, effects of higher orders could affect sizably these corrections. In order to have an idea of how well they are known, we can use the data itself.

The trick is that this effect is more and more important when the asymmetry is computed with a decreasing value of x^{max} , (see fig. 2.9). So that, we can compute the forward-backward asymmetry when $x < x_i^{max}$, and when $x < x_{i+1}^{max}$, and compute the relative change,

$$\frac{A_{fb}(x < x_i^{max}) - A_{fb}(x < x_{i+1}^{max})}{\Delta x_i}$$

This quantity is different from zero due to the energy dependence of the forward-backward asymmetry, and if x^{max} is small enough due to the effect of the I-F QED interference corrections.

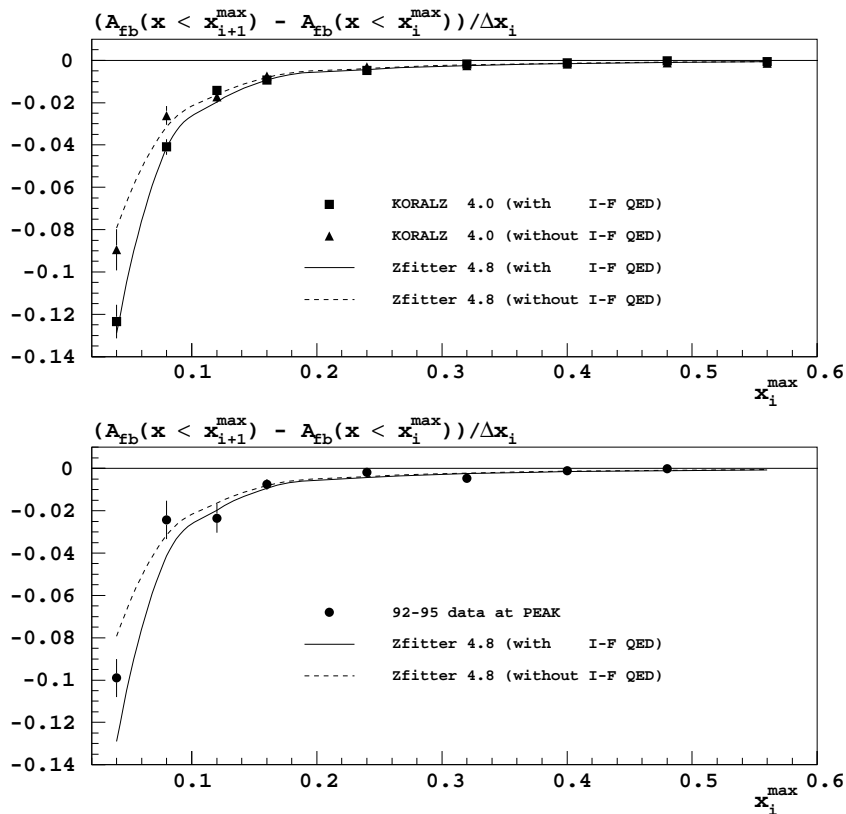


Figure 5.3: Relative change in the asymmetry as a function of x_{max} . The lines correspond to the analytical calculation (ZFITTER 4.8) [61], and the points correspond to the MC predictions in the upper figure, and to real data at the Z peak in the lower figure.

In fig. (5.3) one can see how the analytic calculation of ZFITTER [61] agrees nicely with the MC, as we have already said. But, the lower figure shows also how the data apparently is much less affected than the analytic $\mathcal{O}(\alpha)$ predictions. The fact that the discrepancy is only observed at low values of x^{max} indicates that the problem is related with the effect of I-F QED interference, and not with the data preferring a different value for J_{fb} . It looks like higher order corrections (with opposite sign) decrease the size of these corrections, assuming that ISR is well reproduced by the MC. As we don't know the origin of such discrepancies, we are forced to consider as systematic error these differences. This has been done assuming that the corrections δ_{FB}^i are not known better than a 60%, which is the

difference between the predicted shift when $x_i^{max} = 0.04$ by ZFITTER and the one observed in the data itself. The maximal deviation of the electroweak fitted parameters is quoted in table 5.5.

A similar conclusion on the size of these discrepancies between data and the $\mathcal{O}(\alpha)$ I-F QED interference predictions can be found in ref. [17].

Final State Radiation simulation

We have already mentioned that the MC used to compute the efficiencies was generated with KORALZ 4.0 with the option of single final state bremsstrahlung, (parameter KEYRAD set to 112). We have applied the selection procedure described to a sample of 10^5 MC events generated with exponentiated FSR, (parameter KEYRAD set to 12), and the resulting $\epsilon_{F(B)}^i$ are compared with the previous ones in fig. (5.4). Both samples of efficiencies agree within the statistical errors and no systematic effect is seen.

As we have shown in fig. (4.5), the energy distribution of the detected photons, (mostly FSR), is well reproduced by the MC. The angular distribution of such photons, (that is the relevant information in our case), is well reproduced too, except in the case of hard photons ($E_\gamma > 2$ GeV) that are emitted at large angles ($\cos(\theta_{13}) > 0.2$). This is shown in fig. (5.5), where we have plotted the angle between the measured object in ECAL and the most energetic charged track, ($\cos(\theta_{13})$). This is most probably due to the approximate treatment in the MC of this situation.

In order to evaluate if there is a systematic bias due to this problem, we have removed those events where an ECAL object is detected with more than 2 GeV, and $\cos(\theta_{13}) > 0.2$. This cut is indicated with an arrow in fig. (5.5). The difference on the fitted EW parameters obtained is perfectly compatible with zero, so to be conservative and, as we suspect that these events cannot be reproduced perfectly by the MC simulation, we have taken as systematic errors the statistical errors of these differences. These are shown in table 5.5.

Background

In table 4.2 we have shown that the non $\mu^+\mu^-$ background that survives the selection procedure is at the level of 0.1%, and completely dominated by electrons that leave

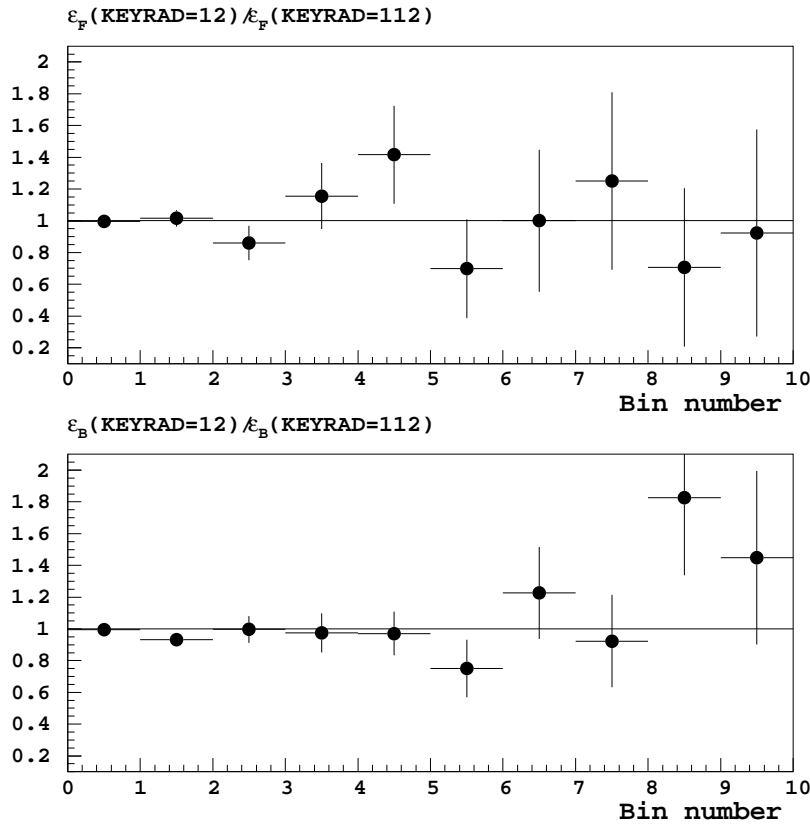


Figure 5.4: Comparison of the efficiencies computed with KORALZ when FSR is exponentiated, (parameter KEYRAD set to 12), and when FSR is calculated to $\mathcal{O}(\alpha)$, (parameter KEYRAD set to 112).

enough signal in the last planes of HCAL.

We can study the effect of this background cutting on the total energy left in ECAL by the two charged tracks selected, requiring $\text{ECAL1} + \text{ECAL2} < \frac{\sqrt{s}}{2}$. This removes most of the Bhabha events and not signal as can be seen in figure (5.6), where we have separated both contributions.

We have removed these events from the data sample, and refit again the S-matrix parameters. The differences are very small, and are considered as systematic error. Table 5.5 shows the magnitude of this effect.

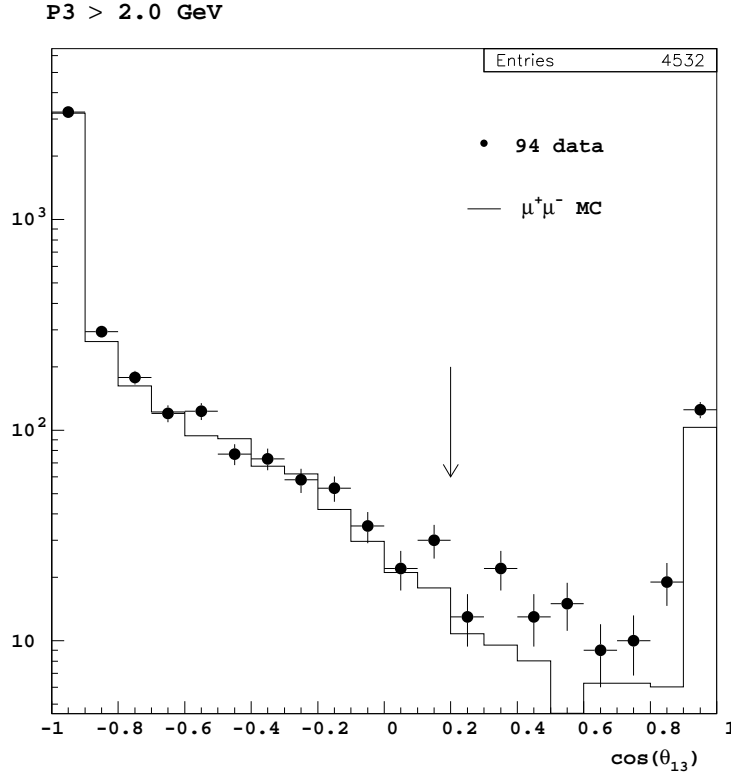


Figure 5.5: Distribution of the angle between the most energetic charged track, and the photon candidate when the measured energy of the photon is greater than 2 GeV. The arrow indicates the cut applied to study the effect of the discrepancies between data and MC.

Uncertainty on the Beam Energy Spread

As we have explained in section 3.1.1, the energy spread of the beams is determined from the measurement of the length of the luminous region, (σ_Z), through the relation:

$$\sigma_{bs} = \frac{\sqrt{s}}{\alpha R} Q_s \sigma_Z$$

The error on this measurement is completely dominated by the systematic due to the Synchrotron tune determination (Q_s), and gives an uncertainty at the level of 2.5% in the beam energy spread [35].

We have changed the values of σ_{bs} in eq. (4.10) by $\pm 2.5\%$, and the changes in the EW parameters are completely negligible.

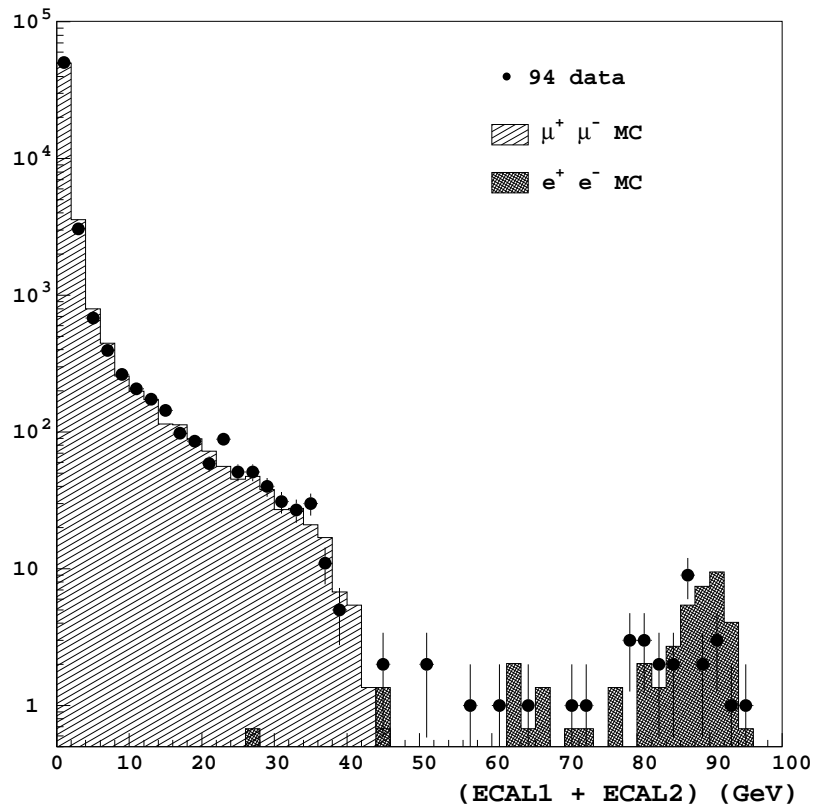


Figure 5.6: Sum of the energy deposited by the two charged tracks selected in the Electromagnetic CALorimeter (ECAL). The agreement between data and MC is reasonably good.

Source of Syst.	Δr_{μ}^{tot}	Δj_{μ}^{tot}	Δr_{μ}^{fb}	Δj_{μ}^{fb}
MC statistics	0.00003	0.006	0.00003	0.009
I-F QED interf.	0.00002	0.002	0.00032	0.009
FSR	nil	0.003	0.00005	0.004
Background	nil	0.001	0.00002	0.003
TOTAL SYST.	0.00004	0.007	0.00032	0.013

Table 5.5: Breakdown of the different contributions to the total systematic errors.

5.3 Analysis of the helicity cross sections and new scalar interactions

An alternative way of presenting the angular distribution information is in terms of helicity cross sections. Let's define:

$$\begin{aligned}\sigma_{LL}^0 &\equiv e_L^- e_R^+ \rightarrow \mu_L^- \mu_R^+ \\ \sigma_{RR}^0 &\equiv e_R^- e_L^+ \rightarrow \mu_R^- \mu_L^+ \\ \sigma_{LR}^0 &\equiv e_L^- e_R^+ \rightarrow \mu_R^- \mu_L^+ \\ \sigma_{RL}^0 &\equiv e_R^- e_L^+ \rightarrow \mu_L^- \mu_R^+\end{aligned}$$

where the symbols L(R) stands for the left (right)-handed helicity. Then, we can write the total and antisymmetric cross sections as

$$\begin{aligned}\sigma^0 &= \frac{1}{2}(\sigma_{LL}^0 + \sigma_{RR}^0 + \sigma_{LR}^0 + \sigma_{RL}^0) \\ \sigma_{fb}^0 &= \frac{3}{8}(\sigma_{LL}^0 + \sigma_{RR}^0 - \sigma_{LR}^0 - \sigma_{RL}^0)\end{aligned}$$

the factor 1/2 corresponds to the spin averaging for unpolarized initial beams.

In the context of the SM, the interference between the Z contribution (dominated by the axial coupling) and the γ contribution (that is only vector coupling) is destructive or constructive as a function of $\sqrt{s'}$. One can compute the different $\sqrt{s'}$ that corresponds to the zeroes of σ_{ij}^0 . From reference [8], we have that at lowest order

$$\begin{aligned}\sigma_{RR}^0(\sqrt{s'}) = 0 &\Rightarrow \sqrt{s'} = 76.9 \text{ GeV} \\ \sigma_{LL}^0(\sqrt{s'}) = 0 &\Rightarrow \sqrt{s'} = 80.0 \text{ GeV} \\ \sigma_{RL}^0(\sqrt{s'}) = 0 &\Rightarrow \sqrt{s'} = 113.1 \text{ GeV} \\ \sigma_{LR}^0(\sqrt{s'}) = 0 &\Rightarrow \sqrt{s'} = 113.1 \text{ GeV}\end{aligned}$$

and this is the reason of the two maxima seen in the forward-backward asymmetry in figure 5.2. In fact, higher order corrections prevent to have exactly a zero for σ_{ij}^0 , but this is not relevant for the discussion here.

We can take profit of the fact that the SM predicts nearly zeroes at $\sqrt{s'} \sim 80(113)$ GeV, to search for scalar particles, which will not interfere with the gauge boson contribution due to the conservation of helicity in the massless fermion limit.

The best place to look for such a signal is at the minimum of the gauge contribution, because there the “background” from the SM will be minimum, while at the Z peak (or at energies close to the photon peak at $\sqrt{s'} \sim 0$) the potential signal will be diluted. Having this in mind, we can write,

$$\begin{aligned}\sigma_{RR}^0 + \sigma_{LL}^0 &= \frac{1}{3}(7\sigma_F^0 - \sigma_B^0) \\ \sigma_{RL}^0 + \sigma_{LR}^0 &= \frac{1}{3}(7\sigma_B^0 - \sigma_F^0)\end{aligned}$$

and therefore we can define the ratio $R_H = (\sigma_{RR}^0 + \sigma_{LL}^0)/(\sigma_{RL}^0 + \sigma_{LR}^0)$ as a function of $\hat{\sigma}_F$ and $\hat{\sigma}_B$ defined in Eqs. (5.1) and (5.2) from the observed number of events. At energies greater than 100 GeV the ratio is inverted in order to have a finite number for all the energy range studied.

In figure 5.7 we can see this ratio of helicity cross sections as a function of the effective centre-of-mass energy obtained with our analysis, together with the results obtained by previous experiments at PEP [62], PETRA [63] and TRISTAN [64]. The continuous line corresponds to the SM predictions. Note, that this figure is very similar to figure 5.2 because, as we have already mentioned, it is another way to look at the angular distribution information, but now we have much more sensitivity to potential new scalar interactions in a single observable.

Although the SM describes well enough the data in all the energy range studied ($\chi^2 = 21.0$ corresponding to 32 measurements, 16 from ALEPH ($\chi^2 = 13.3$) and 16 from the low energy experiments ($\chi^2 = 7.7$)), it’s somehow intriguing the apparent disagreement that can be observed in the energy region where the sensitivity to new scalar particles is maximal. In order to quantify a little bit more this statement, we have considered the possibility to have a narrow scalar resonance with negligible width, with mass (M_{SCAL}) and dimensionless residua R_{SCAL} . In this case,

$$\hat{\sigma}_{SCAL}(s) = \frac{1}{G_F^2} \left[\frac{R_{SCAL}}{s(s - M_{SCAL}^2)^2} \right] \quad (5.3)$$

$$\hat{\sigma}_{fb(SCAL)}(s) = 0 \quad (5.4)$$

and therefore, the ratio R_H would be modified with,

$$R_H = \frac{7\hat{\sigma}_F - \hat{\sigma}_B + 3\hat{\sigma}_{SCAL}}{7\hat{\sigma}_B - \hat{\sigma}_F + 3\hat{\sigma}_{SCAL}} \quad (5.5)$$

$\hat{\sigma}_{SCAL}$ is normalized with the Fermi coupling constant that fixes the weak energy scale. In this way, the parameter R_{SCAL} does not have dimensions.

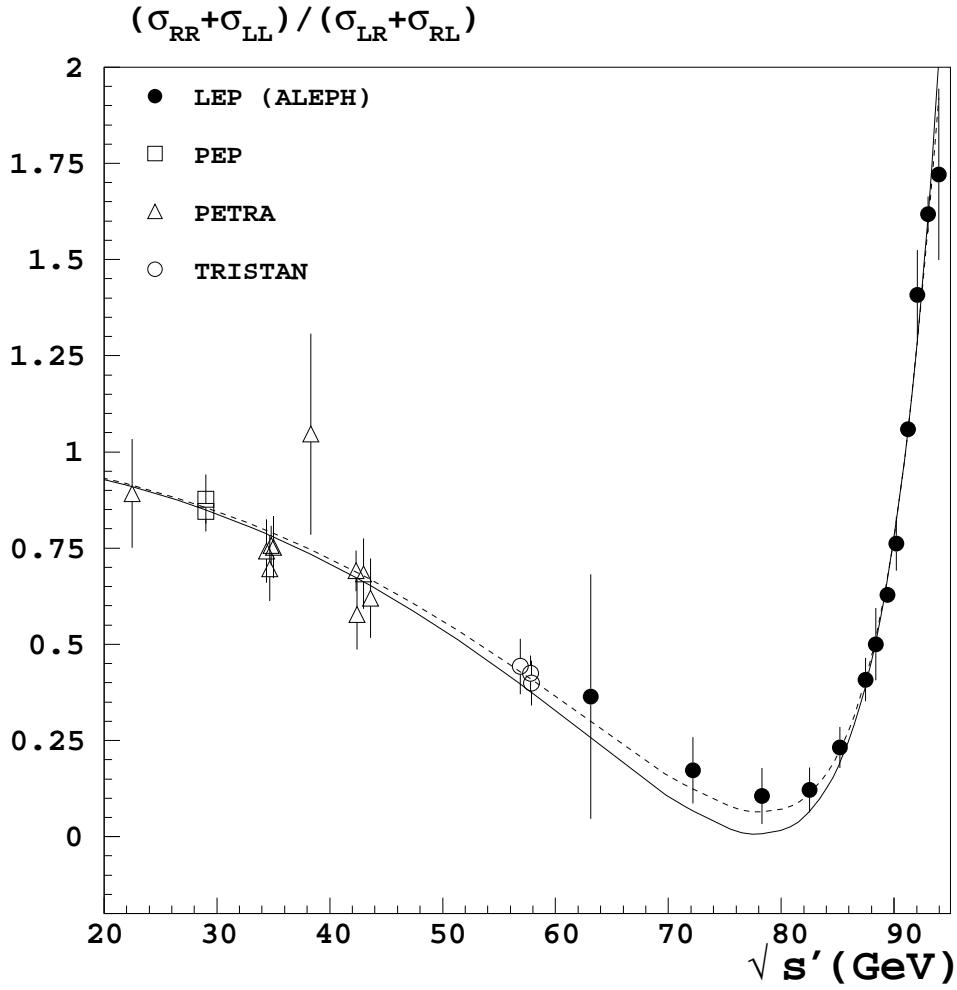


Figure 5.7: Computed helicity cross sections from the measured total cross sections and forward-backward asymmetries of muon-pair production. The continuous line corresponds to the SM predictions while the dashed line corresponds to the best fit when an hypothetical scalar interaction is allowed, (see text).

If we minimize the χ^2 with respect to the mass and residua of the hypothetical scalar particle, we find a minimum ($\chi^2 = 17.0$ with $\chi^2 = 9.9 + 7.1$ from ALEPH and the low energy experiments respectively) at $M_{SCAL} = 101$ GeV and $R_{SCAL} = 1.4 \times 10^{-7}$. In figure 5.8 we have plotted the contours that contain the 39% ($\Delta\chi^2 = 1.00$) and 68% ($\Delta\chi^2 = 2.30$) probability around the minimum. At 95% confidence level, the data is compatible with the absence of any kind of scalar interactions and its

contribution is constrained to be $\hat{\sigma}_{SCAL} < 0.0092$ nb at $\sqrt{s'} = 78.3$ GeV with 95% confidence level.

Note, that in fact the SM itself predicts a scalar interaction through the interchange of a Higgs. However, in the hypothesis of massless fermions the SM Higgs contribution is zero, and even in the case of considering the mass of the fermions R_{SCAL} is suppressed with a factor $(m_e m_\mu)^4 G_F^4$ and therefore $R_{SCAL} \sim 10^{-31}$.

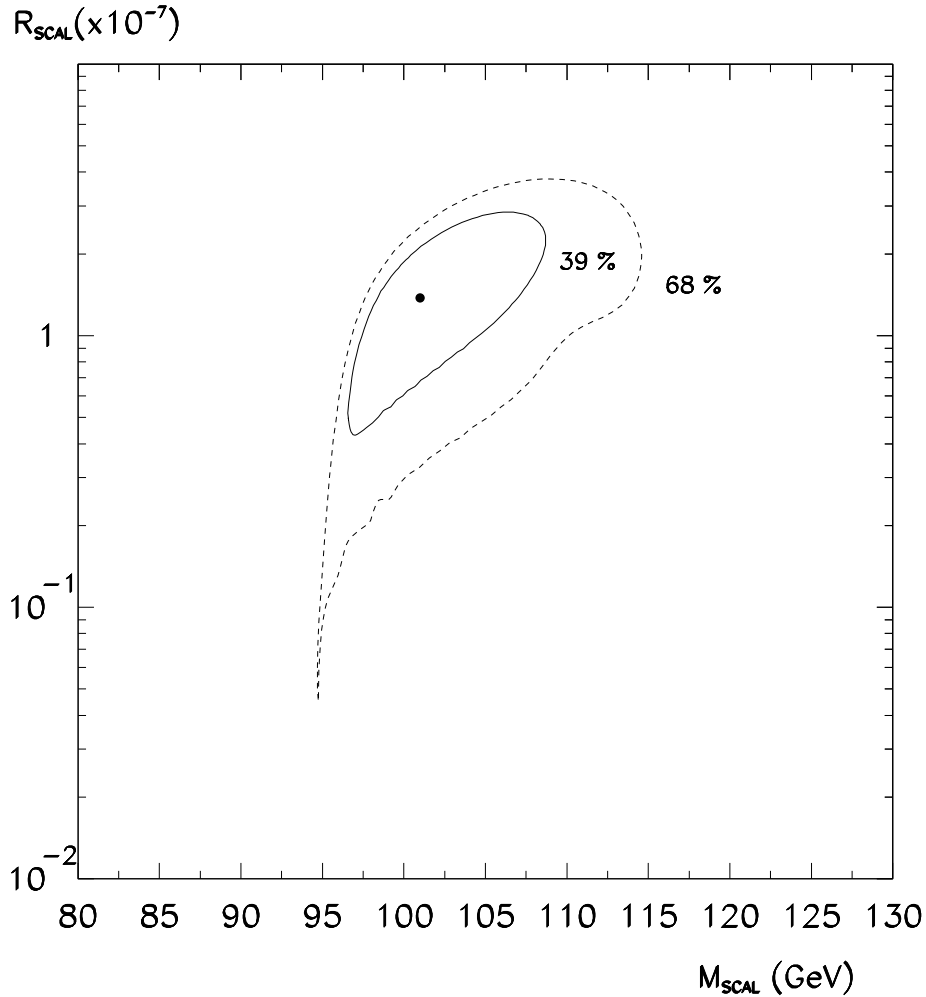


Figure 5.8: Contours of equal probability in the plane R_{SCAL} vs M_{SCAL} . At 95% confidence level data is consistent with no new scalar interactions.

5.4 Limits on extra Z bosons

As we have mentioned in section 2.3 the existence of a new neutral gauge boson Z' will modify the predicted energy dependence of the total cross section, and specially the energy dependence of the forward-backward asymmetry. In this case, there's no gain in the analysis in terms of helicity cross sections, but we can take profit of the measurement of the energy dependence to improve the limits on the mass of new gauge bosons from LEP.

After specifying the model (and without any assumption on the structure of the Higgs sector), only two free parameters remain: the mixing angle θ_3 between $Z - Z'$ and the mass of the heavier-mass eigenstate, $M_{Z'}$. If we want to test one of this particular models, and extract the corresponding limits on these parameters, we can replace the model independent parameterization of $\hat{\sigma}_{tot}(s')$ and $\hat{\sigma}_{fb}(s')$ in Eq. 2.17 by the specific prediction of the model as a function of $M_{Z'}$ and θ_3 .

This procedure takes into account all the possible information in an event-by-event analysis, but at the expenses of being extremely CPU demanding. We have checked that one obtains identical results, if the fit is made, instead, directly to the cross section and asymmetries that appear in table 5.4. This procedure is much faster than the previous one, being the only approximation used that the cross section and asymmetries behave like their SM expectation within the energy bins defined.

We have considered four of the most popular models that introduce a new Z boson, which have been discussed in section 2.3. Three of them (χ -model, ψ -model and η -model) are superstring-inspired models based on the E_6 symmetry group. The other one, is a left-right symmetric model that includes a right-handed $SU(2)_R$ extension of the Standard Model gauge group $SU(2)_L \otimes U(1)$. This kind of models are characterized by the parameter α_{L-R} that describes the coupling of the Z' to fermions, and it can be expressed in terms of the $SU(2)_{L,R}$ coupling constants and the weak mixing angle. We have chosen the specific value $\alpha_{L-R} = 1$.

The effects of the Z' for the L-R and E_6 models on the cross sections and asymmetries were calculated using an addition to the ZFITTER program, called ZEFIT (vers. 3.1) [65], that provides radiatively corrected cross sections and asymmetries for the process $e^+e^- \rightarrow \mu^+\mu^-$. As the standard Z mass changes due to the presence

of a mixed Z' , M_Z was also fitted (using the direct M_Z measurement constraint) along with the mixing angle θ_3 and the Z' mass.

To obtain exclusion limits, we have computed a χ^2 comparing the values that appear in table 5.4 with the different theoretical models. The ALEPH measurements of the hadronic cross section reported in [59] and [58] are also included, but they only improve the sensitivity to the mixing angle. The region defined by $\chi^2 < \chi_{min}^2 + 5.99$ correspond to 95% confidence level for one sided exclusion bounds for two parameters. This is plotted in fig. 5.9 for the models considered, and in table 5.6 the explicit limits are given. In fig. 5.9 the exclusion limits published by CDF [66] in a direct search for Z' bosons are shown.

In order to asses the impact of the measurements obtained with the analysis of radiative events, we can compute these exclusion limits using only those events that are in the first bin ($x < 0.04$), so that $\sqrt{s'} \sim \sqrt{s}$. This is not exactly the same situation that using the inclusive measurements at \sqrt{s} , that would have been even less sensitive to the effects of new physics, but can give us an idea on the effect. We have done this exercise for the χ -model as an example, and the limits in this case are: $M_{Z'} > 222$ GeV while the limits on θ_3 are exactly the same ($-0.0016 < \theta_3 < +0.0036$).

	$E_6(\chi)$	$E_6(\psi)$	$E_6(\eta)$	LR($\alpha_{LR} = 1$)
$M_{Z'} \text{ (GeV)} >$	236	160	173	190
$\theta_3 \text{ (rads)} >$	-0.0016	-0.0020	-0.021	-0.0017
$\theta_3 \text{ (rads)} <$	+0.0036	+0.0038	+0.012	+0.0035
$\chi^2 / \text{d.o.f}$	25.8/39	26.0/39	27.0/39	25.9/39

Table 5.6: 95% confidence level limits on $M_{Z'}$ and θ_3 from fits to the predictions of several models.

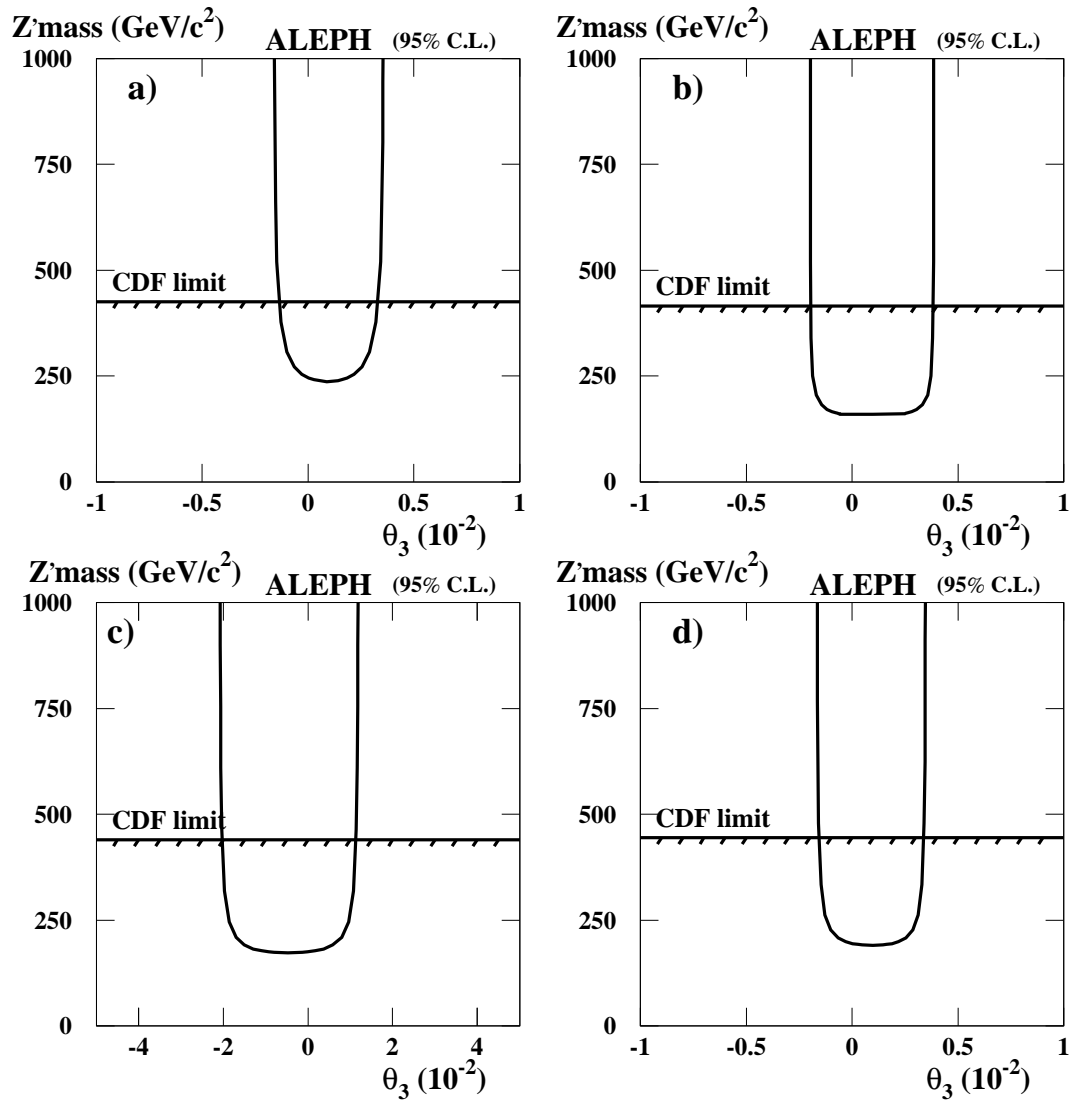


Figure 5.9: Curves corresponding to 95% confidence level contours. a) χ model, b) ψ model, c) η model and d) L-R model.

Chapter 6

Summary and conclusions

The actual scan due to initial state radiation in muonic events has been used to perform a precise measurement of the total cross section and the forward-backward asymmetry in a range of energy still uncovered by present accelerators, spanning from 60 GeV to 136 GeV. These measurements are found to agree reasonable well with the Standard Model expectations.

Our method uses the full statistical power of the event sample by reconstructing, for all events, the effective centre-of-mass energy $\sqrt{s'}$ in an event-by-event basis. This allows the precise analysis of the energy dependence and hence, as a result, the electroweak parameters that describe in a general way the energy dependence of these observables are determined with an unprecedented precision equivalent to have doubled the statistics in ALEPH using the standard analysis.

The energy dependence of the total cross section and the forward-backward asymmetry has been parameterized in a general way using the S-matrix formalism. The accuracy of such approach has been cross-checked with the most up to date SM calculations, and found to cope with the experimental precision.

The results obtained for the S-matrix electroweak parameters are

$$\begin{aligned} r_{\mu}^{\text{tot}} &= 0.14186 \pm 0.00080 \pm 0.00004 \\ j_{\mu}^{\text{tot}} &= -0.033 \pm 0.022 \pm 0.007 \\ r_{\mu}^{\text{fb}} &= 0.00273 \pm 0.00054 \pm 0.00032 \\ j_{\mu}^{\text{fb}} &= 0.807 \pm 0.026 \pm 0.013 \end{aligned}$$

where the second error corresponds to the systematic uncertainty in the extraction

of these parameters.

The precise measurements of the helicity cross sections at centre-of-mass energies around 80 GeV, allows to search for new scalar interactions that are highly suppressed at the Z peak. At 95% confidence level, the data is consistent with the SM predictions.

The improved precision on the measured energy dependence, especially the energy dependence of the forward-backward asymmetry j_μ^{fb} , allows the existing limits from LEP on $M_{Z'}$ to be improved. The sensitivity to the mixing angle θ_3 is completely determined by the existing measurements at the Z peak, and does not benefit from the inclusion of the radiative events.

Appendix A

Writing the helicity cross sections in the S-matrix language.

As we have introduced in section 2.2.2, the helicity amplitude for the process $e^+e^- \rightarrow \mu^+\mu^-$ is written in the S-matrix language as

$$\mathcal{M}^{ij} \equiv \frac{R_\gamma}{s} + \frac{R_Z^{ij}}{s - s_Z}$$

where i (j) stands for the polarization of the incoming e^- (outgoing μ^-).

Therefore, the helicity cross section $\hat{\sigma}_{ij}$ is

$$\begin{aligned} \hat{\sigma}_{ij}(s) \equiv \frac{s}{2} |\mathcal{M}^{ij}|^2 &= \frac{|R_\gamma|^2}{2s} + \frac{s |R_Z^{ij}|^2}{2 |s - s_Z|^2} \\ &\quad + \frac{2\Re(R_\gamma^* R_Z^{ij})(s - \overline{M}_Z^2) + 2\Im(R_\gamma^* R_Z^{ij})\overline{M}_Z \overline{\Gamma}_Z}{2 |s - s_Z|^2} \\ &= \frac{|R_\gamma|^2}{2s} \\ &\quad + \frac{s \left(|R_Z^{ij}|^2 + 2\Im(R_\gamma^* R_Z^{ij}) \frac{\overline{\Gamma}_Z}{\overline{M}_Z} \right)}{2 |s - s_Z|^2} \\ &\quad + \frac{(s - \overline{M}_Z^2) \left(2\Re(R_\gamma^* R_Z^{ij}) - 2\Im(R_\gamma^* R_Z^{ij}) \frac{\overline{\Gamma}_Z}{\overline{M}_Z} \right)}{2 |s - s_Z|^2} \end{aligned}$$

where s_Z is defined to be $s_Z \equiv \overline{M}_Z^2 - i\overline{\Gamma}_Z \overline{M}_Z$.

If we introduce now the notation,

$$\begin{aligned} r^\gamma &= \frac{3}{4\pi\alpha^2} |R_\gamma|^2 \\ r_{ij} &= \frac{3}{4\pi\alpha^2} \left[|R_Z^{ij}|^2 + 2\frac{\bar{\Gamma}_Z}{M_Z} \Im(R_\gamma^* R_Z^{ij}) \right] \\ J_{ij} &= \frac{3}{4\pi\alpha^2} \left[2\Re(R_\gamma^* R_Z^{ij}) - 2\frac{\bar{\Gamma}_Z}{M_Z} \Im(R_\gamma^* R_Z^{ij}) \right] \end{aligned}$$

then it is obvious that

$$\hat{\sigma}_{ij}(s) = \frac{2}{3}\pi\alpha^2 \left[\frac{r^\gamma}{s} + \frac{sr_{ij} + (s - \overline{M}_Z^2)J_{ij}}{(s - \overline{M}_Z^2)^2 + \overline{M}_Z^2\bar{\Gamma}_Z^2} \right]$$

From the definition of the total cross section and antisymmetric cross section,

$$\begin{aligned} \hat{\sigma} &= \frac{1}{2}(\hat{\sigma}_{LL} + \hat{\sigma}_{RR} + \hat{\sigma}_{LR} + \hat{\sigma}_{RL}) \\ \hat{\sigma}_{fb} &= \frac{3}{8}(\hat{\sigma}_{LL} + \hat{\sigma}_{RR} - \hat{\sigma}_{LR} - \hat{\sigma}_{RL}) \end{aligned}$$

we have,

$$\begin{aligned} r_{tot} &= \frac{1}{2}(r_{LL} + r_{RR} + r_{LR} + r_{RL}) \\ J_{tot} &= \frac{1}{2}(J_{LL} + J_{RR} + J_{LR} + J_{RL}) \\ r_{fb} &= \frac{3}{8}(r_{LL} + r_{RR} - r_{LR} - r_{RL}) \\ J_{fb} &= \frac{3}{8}(J_{LL} + J_{RR} - J_{LR} - J_{RL}) \end{aligned}$$

and therefore we have the expressions shown in equations 2.26 and 2.27

$$\begin{aligned} \hat{\sigma}(s) &= \frac{4}{3}\pi\alpha^2 \left[\frac{r^\gamma}{s} + \frac{sr_{tot} + (s - \overline{M}_Z^2)J_{tot}}{(s - \overline{M}_Z^2)^2 + \overline{M}_Z^2\bar{\Gamma}_Z^2} \right] \\ \hat{\sigma}_{fb}(s) &= \pi\alpha^2 \left[\frac{sr_{fb} + (s - \overline{M}_Z^2)J_{fb}}{(s - \overline{M}_Z^2)^2 + \overline{M}_Z^2\bar{\Gamma}_Z^2} \right] \end{aligned}$$

If we neglect the small contribution from weak boxes diagrams in the SM, and we neglect the energy dependence of the effective couplings that absorb higher order corrections, we can write the SM prediction for the complex helicity amplitudes R_γ and R_Z^{ij} as,

$$\begin{aligned}
R_\gamma &= \sqrt{\frac{4\pi}{3}} \bar{\alpha}(s) \\
R_Z^{LL} &= \sqrt{\frac{4\pi}{3}} \left(\frac{\overline{G}_F M_Z^2}{2\sqrt{2}\pi} \right) (g_{V_e} + g_{A_e})(g_{V_\mu} + g_{A_\mu}) \\
R_Z^{RR} &= \sqrt{\frac{4\pi}{3}} \left(\frac{\overline{G}_F M_Z^2}{2\sqrt{2}\pi} \right) (g_{V_e} - g_{A_e})(g_{V_\mu} - g_{A_\mu}) \\
R_Z^{LR} &= \sqrt{\frac{4\pi}{3}} \left(\frac{\overline{G}_F M_Z^2}{2\sqrt{2}\pi} \right) (g_{V_e} + g_{A_e})(g_{V_\mu} - g_{A_\mu}) \\
R_Z^{RL} &= \sqrt{\frac{4\pi}{3}} \left(\frac{\overline{G}_F M_Z^2}{2\sqrt{2}\pi} \right) (g_{V_e} - g_{A_e})(g_{V_\mu} + g_{A_\mu})
\end{aligned}$$

where the couplings g_V and g_A are complex quantities, and $\bar{\alpha}(s)$ is the effective complex electromagnetic coupling constant, defined as:

$$\bar{\alpha}(s) = \frac{\alpha}{1 + \Pi^\gamma(s)}$$

where $\Pi^\gamma(s)$ is the photon self energy.

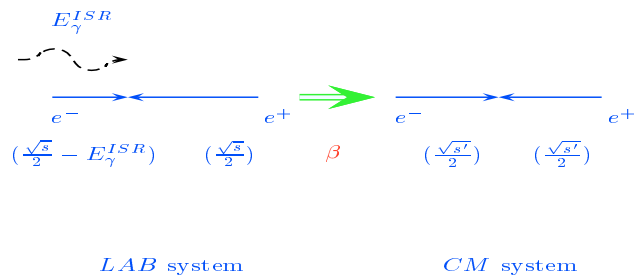
In this way, the SM predictions for the S-matrix parameters are approximately proportional to:

$$\begin{aligned}
r_{tot} &\propto ((\Re(g_{V_e}))^2 + (\Re(g_{A_e}))^2)((\Re(g_{V_\mu}))^2 + (\Re(g_{A_\mu}))^2) \\
J_{tot} &\propto \Re(g_{V_e})\Re(g_{V_\mu}) \\
r_{fb} &\propto \Re(g_{A_e})\Re(g_{V_e})\Re(g_{A_\mu})\Re(g_{V_\mu}) \\
J_{fb} &\propto \Re(g_{A_e})\Re(g_{A_\mu})
\end{aligned}$$

Appendix B

Relativistic kinematics.

B.1 Effective centre-of-mass energy.



From the Lorentz equation that predicts the change in energy as,

$$E' = \frac{E + |\beta| P_z}{\sqrt{1 - |\beta|^2}}$$

one can compute the energy of the electron and positron in the CM system as,

$$\begin{aligned} \frac{\sqrt{s'}}{2} &= \left(\frac{\sqrt{s}}{2} - E_\gamma^{ISR} \right) \frac{1 + |\beta|}{\sqrt{1 - |\beta|^2}} \\ \frac{\sqrt{s'}}{2} &= \frac{\sqrt{s}}{2} \frac{1 - |\beta|}{\sqrt{1 - |\beta|^2}} \end{aligned}$$

Therefore, the radiated energy and the effective centre-of-mass energy can be written as a function of the magnitude of the boost with:

$$\begin{aligned} E_\gamma^{ISR} &= \frac{|\beta|}{1 + |\beta|} \sqrt{s} \\ s' &= s \left(\frac{1 - |\beta|}{1 + |\beta|} \right) \end{aligned}$$

B.2 Final State Radiation in the CM system.

For three particles lying in a plane, their energies can be defined in terms of their total energy ($\sqrt{s'}$) and the angles between them (θ'_{ij}). In particular, the energy of the photon (E'_3) can be calculated in this way when the position of the object in ECAL is known. Conservation of momentum in the CM system constrains the three momentum vectors to form a closed triangle.

The interior angles of this triangle (α_{ij}) are related to the angles between the track vectors by $\alpha_{ij} = \pi - \theta'_{ij}$. The conservation of energy constrains the sum of the magnitude of the momenta to be $\sqrt{s'}$, that is just the perimeter of this triangle.

Now, applying the law of sines,

$$\frac{\sin(\alpha_{12})}{E'_3} = \frac{\sin(\alpha_{13})}{E'_2}$$

and the relation $\sin(\alpha_{ij}) = \sin(\theta'_{ij})$ we have,

$$E'_3 = \frac{\sin(\theta'_{12})}{\sin(\theta'_{13})} E'_2$$

$$\begin{aligned}
&= \frac{\sin(\theta'_{12})}{\sin(\theta'_{13})}(\sqrt{s'} - E'_3 - E'_1) \\
&= \frac{\sin(\theta'_{12})}{\sin(\theta'_{13})}(\sqrt{s'} - E'_3(1 + \frac{\sin(\theta'_{23})}{\sin(\theta'_{12})}))
\end{aligned}$$

and solving the last equation we have,

$$E'_3 = \sqrt{s'} \left(\frac{\sin(\theta'_{12})}{\sin(\theta'_{12}) + \sin(\theta'_{13}) + \sin(\theta'_{23})} \right)$$

Appendix C

Efficiencies computed from Monte Carlo simulation.

The correction functions $\epsilon_{F(B)}^i(s)$ are computed using Monte Carlo simulated events. These functions are defined from the efficiency matrix $\epsilon_{F(B)}^{ij}(s)$ through,

$$\epsilon_{F(B)}^i(s) \equiv \sum_{j=1, \text{nbin}} \epsilon_{F(B)}^{ij}(s) \frac{\hat{\sigma}_{F(B)}^j(s)}{\hat{\sigma}_{F(B)}^i(s)} \quad (\text{C.1})$$

with

$$\epsilon_{F(B)}^{ij}(s) = \frac{N_{sel}(s, x_i \leq x_{rec} < x_{i+1}, \cos \theta_{rec} \geq (<)0)}{N_{gen}(s, x_j \leq x_{gen} < x_{j+1}, \cos \theta_{gen} \geq (<)0)}$$

and

$$\hat{\sigma}_{F(B)}^i(s) \equiv \int_{x_i}^{x_{i+1}} dx H(s, x) \hat{\sigma}_{F(B)}(s, x)$$

where the radiator function $H(s, x)$ and the total cross section $\hat{\sigma}(s' = s(1-x))$ have been introduced in chapter 2.

They are given in table C.1 as a function of the nominal centre-of-mass energy, and the percentage of radiated energy (x). The size of the bins correspond to the ones choosed in the experimental analysis.

\sqrt{s} (GeV)	$0.00 \leq x < 0.04$		$0.04 \leq x < 0.08$		$0.08 \leq x < 0.12$	
	ϵ_F (%)	ϵ_B (%)	ϵ_F (%)	ϵ_B (%)	ϵ_F (%)	ϵ_B (%)
91.2	80.904 ± 0.073	81.051 ± 0.073	64.29 ± 0.82	61.71 ± 0.66	72.7 ± 1.9	61.9 ± 1.3
90.2	81.71 ± 0.21	80.91 ± 0.19	61.0 ± 3.6	60.3 ± 2.8	68 ± 10	66.7 ± 5.4
92.0	80.16 ± 0.20	81.60 ± 0.22	63.7 ± 2.1	58.0 ± 1.7	64.4 ± 6.3	59.3 ± 3.9
89.4	82.28 ± 0.16	80.44 ± 0.13	66.6 ± 2.4	62.5 ± 1.7	70.0 ± 5.6	60.9 ± 2.8
93.0	81.64 ± 0.20	84.14 ± 0.25	58.43 ± 0.95	58.74 ± 0.88	60.6 ± 2.8	56.6 ± 2.4
88.4	82.48 ± 0.25	80.46 ± 0.18	64.6 ± 3.0	63.4 ± 2.0	63.6 ± 6.1	56.6 ± 2.8
93.7	84.35 ± 0.28	88.86 ± 0.41	57.42 ± 0.88	58.74 ± 0.89	55.1 ± 2.3	55.9 ± 2.1
130.0	77.45 ± 0.85	92.0 ± 1.9	68.4 ± 4.4	88 ± 13	55.0 ± 5.2	59 ± 14
136.0	79.51 ± 0.87	94.9 ± 1.6	57.9 ± 3.9	89 ± 12	58.3 ± 5.0	71 ± 13
\sqrt{s} (GeV)	$0.12 \leq x < 0.16$		$0.16 \leq x < 0.24$		$0.24 \leq x < 0.32$	
	ϵ_F (%)	ϵ_B (%)	ϵ_F (%)	ϵ_B (%)	ϵ_F (%)	ϵ_B (%)
91.2	87.3 ± 2.9	65.2 ± 2.1	78.9 ± 4.6	57.1 ± 2.2	110.0 ± 6.7	60.8 ± 3.5
90.2	71 ± 13	60.8 ± 7.1	50 ± 18	68.7 ± 7.5	150 ± 61	54 ± 11
92.0	75 ± 13	50.0 ± 6.3	85 ± 25	50.0 ± 7.9	120 ± 58	56 ± 11
89.4	80.0 ± 8.7	60.8 ± 4.1	90 ± 12	53.6 ± 4.0	89 ± 13	49.0 ± 5.4
93.0	60.2 ± 6.8	50.2 ± 3.6	86 ± 10	55.0 ± 5.0	100 ± 17	50.0 ± 7.5
88.4	77 ± 11	61.3 ± 4.6	81 ± 11	54.7 ± 4.1	100.0 ± 8.8	60.2 ± 5.6
93.7	59.8 ± 6.1	50.2 ± 4.1	66.1 ± 6.6	52.1 ± 5.3	111 ± 26	46.6 ± 7.2
130.0	55.6 ± 5.4	62.1 ± 9.7	49.0 ± 4.1	60 ± 10	55.3 ± 4.7	63 ± 12
136.0	59.7 ± 5.2	63 ± 11	53.5 ± 4.2	53.1 ± 8.8	55.0 ± 4.5	93 ± 19
\sqrt{s} (GeV)	$0.32 \leq x < 0.40$		$0.40 \leq x < 0.48$		$0.48 \leq x < 0.56$	
	ϵ_F (%)	ϵ_B (%)	ϵ_F (%)	ϵ_B (%)	ϵ_F (%)	ϵ_B (%)
91.2	97.7 ± 7.0	60.2 ± 4.4	115 ± 11	62.4 ± 5.3	60 ± 11	48.6 ± 5.6
90.2	0_{-0}^{+84}	33 ± 11	166 ± 61	75 ± 15	43 ± 19	25 ± 13
92.0	67 ± 47	60 ± 18	80 ± 47	70 ± 28	100 ± 50	30 ± 14
89.4	57 ± 14	55.5 ± 7.3	79 ± 19	58.9 ± 7.6	16.7 ± 9.4	30.3 ± 8.3
93.0	67 ± 60	34.5 ± 9.7	62 ± 17	41 ± 13	50 ± 21	45 ± 10
88.4	74 ± 14	50.0 ± 7.5	80 ± 20	49.0 ± 8.2	37 ± 11	31.1 ± 7.1
93.7	133 ± 38	36.6 ± 8.8	67 ± 60	50 ± 13	14 ± 13	45 ± 11
130.0	56.7 ± 4.4	64.1 ± 9.6	59.8 ± 2.8	76.4 ± 5.5	36.5 ± 1.0	39.3 ± 1.0
136.0	49.3 ± 4.8	48 ± 11	64.9 ± 4.1	72.2 ± 9.2	37.6 ± 1.1	39.8 ± 1.3
\sqrt{s} (GeV)	$0.56 \leq x < 0.64$					
	ϵ_F (%)	ϵ_B (%)				
91.2	45 ± 11	44.6 ± 7.0				
90.2	100 ± 28	9.0 ± 9.5				
92.0	0_{-0}^{+50}	25_{-25}^{+50}				
89.4	46 ± 16	24.3 ± 7.1				
93.0	57 ± 24	29 ± 12				
88.4	25.0 ± 9.6	28.1 ± 8.2				
93.7	29 ± 17	20 ± 12				
130.0	22.6 ± 5.9	33.3 ± 3.5				
136.0	27.6 ± 2.0	30.3 ± 1.8				

Table C.1: Computed $\epsilon_{F(B)}(s, x)$ from Monte Carlo simulation at the different LEP nominal energies.

Bibliography

- [1] S.L.Glashow, Nucl. Phys. **B22** (1961) 579.
S.Weinberg, Phys. Rev. Lett. **19** (1967) 1264.
A.Salam, *Elementary Particle Theory*, ed. N.Svartholm, Almqvist and Wiksell, Stockholm (1968) 367.
S.L.Glashow, J.Iliopoulos and L. Maiani, Phys. Rev. **D2** (1970) 1285.
- [2] ALEPH collaboration, D. Buskulic et al. Z. Phys. **C62** (1994) 539.
DELPHI collaboration, P. Abreu et al., Nucl. Phys. **B418** (1994) 403.
L3 collaboration, M. Acciarri et al., Z. Phys. **C62** (1994) 551.
OPAL collaboration, R. Akers et al., Z. Phys. **C61** (1994) 19.
- [3] OPAL collaboration, P. Acton et al., Phys. Lett. **B273** (1991) 338.
DELPHI collaboration, P. Abreu et al., Z. Phys. **C65** (1995) 603.
L3 collaboration, M. Acciarri et al., Phys. Lett. **B374** (1996) 331.
- [4] H.White, *Evidence for $\bar{\nu}_\mu - \bar{\nu}_e$ oscillations from Muon decay at rest*, talk presented at ICHEP'96, Warsaw, 25-31 July (1996).
- [5] G.'t Hooft, Nucl. Phys. **B33** (1971) 173.
- [6] J.-P.Martin, *Higgs particle searches at LEP*, talk presented at ICHEP'96, Warsaw, 25-31 July (1996).
- [7] M.Grünwald, *Combined precision Electroweak results from LEP/SLC*, talk presented at ICHEP'96, Warsaw, 25-31 July (1996).
- [8] J-M Frere, V.A. Novikov and M.I. Vysotsky, *Zeroes of the process $e^+e^- \rightarrow \bar{f}f$ cross section and search for new physics*, ULB-TH/96-5, HEP-PH/9605241

- [9] M. Rijssenbeek, *Measurement of the Mass of the W boson from CDF/D0*, talk presented at ICHEP'96, Warsaw, 25-31 July (1996).
- [10] CDHS Coll., A.Blondel *et al.*, Z. Phys. **C45** (1990) 361.
CHARM Coll., J.V.Allaby *et al.*, Z. Phys. **C36** (1987) 611.
CCFR Coll., K.McFarland, *An improved measurement of $\sin^2 \theta_W$ from neutrino-nucleon deep inelastic scattering*, proceedings of the XV workshop on Weak Interactions and Neutrinos, Talloires France, G. Bonneaud *et al.* eds., September (1996) vol II, 607.
- [11] A.D.Martin and D.Zeppenfeld, Phys. Lett. **B345** (1994) 558.
S.Eidelmann and F.Jegerlehner, Z. Phys. **C67** (1995) 585.
H.Burkhardt and B.Pietrzyk, Phys. Lett. **B356** (1995) 398.
M.L.Swartz, *Reevaluation of the Hadronic Contribution to $\alpha(M_Z^2)$* , SLAC-PUB-95-7001, September 1995.
- [12] P.Grannis, *Measurement of the Mass of the Top Quark from CDF/D0*, talk presented at ICHEP'96, Warsaw, 25-31 July (1996).
- [13] B.W.Lynn, *High-precision tests of electroweak physics on the Z^0 resonance*, Proceedings of the Workshop on Polarization at LEP, CERN 88-06, September 1988, G.Alexander *et al.* eds., Vol I, 24.
W.Hollik, *Radiative Corrections in the Standard Model and their role for precision tests of the Electroweak theory*, Fortschr. Phys. **38** (1990) 165.
D.Bardin, W.Hollik and T.Riemann, *Bhabha scattering with higher order weak loop corrections*, Z. Phys. **C49** (1991) 485.
- [14] *Reports of the working group on precision calculations for the Z^0 resonance*, eds. D.Bardin, W.Hollik and G.Passarino, CERN 95-03, March (1995).
- [15] F.A.Berends, Proceedings of the Workshop on Z^0 physics at LEP I, CERN 89-08 Vol I, 89.
M.Böhm, W.Hollik, the same proceedings Vol I, 203 and references therein.
- [16] S. Jadach and Z. Was, CERN-TH 7232/94 April (1994).

- [17] DELPHI Coll., P.Abreu *et al.*, *First study of the Interference between Initial and Final State Radiation at the Z resonance*, CERN-PPE/96-44 March (1996), submitted to *Z. Phys.*
- [18] M.Martínez and F.Teubert, *Z. Phys.* **C65** (1995) 267.
- [19] M.Martínez, L.Garrido, R.Miquel, J.L.Harton and R. Tanaka, *Z. Phys.* **C49** (1991) 645.
- [20] R.G. Stuart, *Phys. Lett.* **B272** (1991) 353;
A. Leike, T. Riemann and J. Rose, *Phys. Lett.* **B273** (1991) 513.
T. Riemann, *Phys. Lett.* **B293** (1992) 451.
- [21] G.Burgers, W.Hollik and M.Martínez, FORTRAN code based on Proceedings of the Workshop on Z^0 physics at LEP I, CERN 89-08. It has been upgraded by including the results of [14] and references therein.
- [22] R.Casalbuoni, P.Chiappeta, D.Dominici, F.Feruglio and R. Gatto, *Nucl. Phys.* **B310** (1988) 181.
J.Layssac, F.M.Renard and C.Verzegnassi, *Z. Phys.* **C53** (1992) 97.
- [23] D.London and J.L.Rosner, *Phys. Rev.* **D34** (1986) 1530.
- [24] R.N.Mohapatra and J.C.Pati, *Phys. Rev.* **D11** (1975) 566.
- [25] R.N.Mohapatra and G.Senjanovic, *Phys. Rev. Lett.* **44** (1980) 912, and *Phys. Rev.* **D21** (1981) 165.
- [26] R.M.Barnett *et al.* *Review of Particle Properties*, *Phys. Rev.* **D54** (1996) 1.
- [27] G. Altarelli *et al.*, *Phys. Lett.* **B318** (1993) 139.
- [28] ALEPH Coll., D.Decamp *et al.*, *Nucl. Inst. and Meth.* **A294** (1990) 121.
ALEPH Coll., D.Buskulic *et al.*, *Nucl. Inst. and Meth.* **A360** (1995) 481.
- [29] DELPHI Coll., P.Aarnio *et al.*, *Nucl. Inst. and Meth.* **A303** (1991) 233.
- [30] L3 Coll., B.Adeva *et al.*, *Nucl. Inst. and Meth.* **A289** (1990) 35.
- [31] OPAL Coll., K.Ahmet *et al.*, *Nucl. Inst. and Meth.* **A305** (1991) 275.

- [32] A.A.Sokolov and I.M.Ternov, *Sov. Phys. Dokl.* **8** (1964) 1203.
- [33] V.N.Baier and Y.F.Orlov, *Sov. Phys. Dokl.* **10** (1966) 1145.
A.A.Zholentz *et al.* , *Phys. Lett.* **96B** (1980) 214.
A.S.Artamonov *et al.* , *Phys. Lett.* **118B** (1982) 225.
D.P.Barber *et al.* , *Phys. Lett.* **135B** (1984) 498.
W.W.McKay *et al.* , *Phys. Rev.* **D29** (1984) 2483.
- [34] G.Wilkinson, *Measurement of the LEP Beam Energy*, talk presented at ICHEP'96, Warsaw, 25-31 July (1996).
- [35] E.Lançon and A.Blondel, *Determination of the LEP Energy Spread Using Experimental Constraints*, ALEPH internal report , ALEPH 96-136 (1996).
- [36] S.Jadach, *Status of the Bhabha Scattering*, talk presented at ICHEP'96, Warsaw, 25-31 July (1996).
- [37] P.Mató, *Data Processing for Large e^+e^- Experiments*, Ph.D.thesis, University of Barcelona (1990).
- [38] M.Delfino *et al.* , *Comp. Phys. Comm.* **57** (1989) 401.
- [39] J.Knobloch, *JULIA Users and Programmers guide* ALEPH internal report , ALEPH 90-11 (1990).
- [40] H.Albrecht, E.Blucher and J.Boucrot, *ALPHA Users Guide* ALEPH internal report , ALEPH 95-112 (1995).
- [41] G.Batignani *et al.* , *Nucl. Phys. B (Proc. Suppl.)* **23A** (1991) 291.
- [42] G.J.Barber *et al.* , *Nucl. Inst. and Meth.* **A279** (1989) 212.
- [43] W.B.Atwood *et al.* , *Nucl. Inst. and Meth.* **A306** (1991) 446.
- [44] P.Némethy *et al.* , *Nucl. Inst. and Meth.* **A212** (1983) 273.
- [45] H.Videau, *The ALEPH Pictorial Electromagnetic Calorimeter - A High Granularity Gaseous Calorimeter Operated in a High Magnetic Field*, Invited talk at the 2nd Pisa Meeting on advanced detectors, Castiglione, Italy, June 1983.
- [46] M.G.Catanesi *et al.* , *Nucl. Inst. and Meth.* **A297** (1990) 390.

- [47] R.Frühwirth, HEPHY-PUB 503/87 (1987).
- [48] A.Rougé *et al.* , *A Method for Photon Reconstruction in ALEPH*, ALEPH internal report , ALEPH 93-107 (1993).
J.Knobloch and P.Norton (eds.), *Status of Reconstruction Algorithms for ALEPH*, ALEPH internal report , (1991).
- [49] S.Jadach and Z.Was, *Comput. Phys. Comm.* **36** (1985) 191;
S.Jadach, B.F.L.Ward and Z.Was, *Comput. Phys. Comm.* **66** (1991) 276;
S.Jadach, B.F.L.Ward and Z.Was, *Comput. Phys. Comm.* **79** (1994) 503;
- [50] M.Böhm, A.Denner and W.Hollik, *Nucl. Phys.* **B304** (1988) 687.
F.A.Berends, R.Kleiss and W.Hollik, *Nucl. Phys.* **B304** (1988) 712.
- [51] F.A.Berends *et al.* , *Phys. Lett.* **B148** (1984) 489
F.A.Berends *et al.* , *Phys. Lett.* **B253** (1985) 421.
- [52] B.Bloch *et al.* , *KINGAL User's Guide*, ALEPH internal report , ALEPH 87-53 (1987).
- [53] R.Brun *et al.* , *GEANT3 User's Guide*, CERN-DD/EE/84-1 (1987).
- [54] F.Ranjard *et al.* , *GALEPH Monte Carlo program for ALEPH*, ALEPH internal report , ALEPH 88-119 (1988).
- [55] H.Fesefeldt, *GHEISHA*, Aachen 3rd Inst. Nucl. Phys. **A23** (Proc. Suppl.) (1991) 291.
- [56] W.B.Atwood and J.Thomas, *Observation of the process $e^+e^- \rightarrow l^+l^-\gamma$ in ALEPH.*, ALEPH internal report , ALEPH 90-47 (1990).
- [57] The S-Matrix subgroup of the LEP Electroweak Working Group, *An investigation of the Interference between photon and Z-boson exchange.*, ALEPH internal report , ALEPH 96-108 (1996).
- [58] ALEPH Coll., D.Buskulic *et al.* , *Phys. Lett.* **B378** (1996) 373.
- [59] ALEPH Coll., D.Decamp *et al.* , *Z. Phys.* **C48** (1990) 365.
ALEPH Coll., D.Decamp *et al.* , *Z. Phys.* **C53** (1992) 1.
ALEPH Coll., D.Buskulic *et al.* , *Z. Phys.* **C60** (1993) 71.

- ALEPH Coll., D. Buskalic *et al.*, *Z. Phys.* **C62** (1994) 539.
ALEPH Coll., *Preliminary results on Z Production Cross Section and Lepton Forward-Backward Asymmetries using the 1990-1995 Data.*, contributed paper to ICHEP'96, PA-07-069.
- [60] M. Martínez and F. Teubert, *On the energy dependence of the ALEPH leptonic F-B asymmetries*, ALEPH internal report ALEPH 95-045, April 1995.
- [61] D. Bardin *et al.*, *Z. Phys.* **C44** (1989) 493.; *Comp. Phys. Com.* **59** (1990) 303.; *Nucl. Phys.* **B351** (1991) 1.; *Phys. Lett.* **B255** (1991) 290 and CERN-TH 6443/92 (May 1992).
- [62] HRS Collab., M. Derrick *et al.*, *Phys. Rev.* **D 31** (1985) 2352;
MAC Collab., W. W. Ash *et al.*, *Phys. Rev. Lett.* **55** (1985) 1831;
MARK II Collab., M. E. Levi *et al.*, *Phys. Rev. Lett.* **51** (1983) 1941;
- [63] CELLO Collab., H. J. Behrend *et al.*, *Phys. Lett.* **B 191** (1987) 209;
JADE Collab., W. Bartel *et al.*, *Z. Phys.* **C 26** (1985) 507;
MARK J Collab., B. Adeva *et al.*, *Phys. Rev.* **D 38** (1988) 2665;
PLUTO Collab., Ch. Berger *et al.*, *Z. Phys.* **C 21** (1983) 53;
TASSO Collab., W. Braunschweig *et al.*, *Z. Phys.* **C 40** (1988) 163;
- [64] AMY Collab., A. Bacala *et al.*, *Phys. Lett.* **B 331** (1994) 227;
TOPAZ Collab., B. Howell *et al.*, *Phys. Lett.* **B 291** (1992) 206;
VENUS Collab., K. Abe *et al.*, *Z. Phys.* **C 48** (1990) 13;
- [65] A. Leike, S. Riemann and T. Riemann, Munich University Preprint LMU-91/06, and FORTRAN program ZEFIT;
A. Leike, S. Riemann and T. Riemann, *Phys. Lett.* **B291** (1992) 187.
- [66] CDF Coll., F. Abe *et al.*, *Phys. Rev.* **D51** (1995) 949.